

# Synthesis and Characterization of Pristine and Doped (Ti and Cr) AlN Thin Films

By

**Padmalochan Panda**

(Enrolment No. PHYS 02 2013 04 006 )

**Indira Gandhi Centre for Atomic Research, Kalpakkam, India.**

*A thesis submitted to the  
Board of Studies in Physical Sciences  
in partial fulfillment of requirements  
for the Degree of*

**DOCTOR OF PHILOSOPHY**

of

**HOMI BHABHA NATIONAL INSTITUTE**




**July, 2019**





## Homi Bhabha National Institute

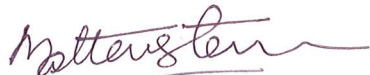
### Recommendations of the Viva Voce Board


As members of the Viva Voce Committee, we certify that we have read the dissertation prepared by **Padmalochan Panda** entitled "**Synthesis and Characterization of Pristine and Doped (Ti and Cr) AlN Thin Films**" and recommend that it may be accepted as fulfilling the thesis requirement for the award of Degree of Doctor of Philosophy.

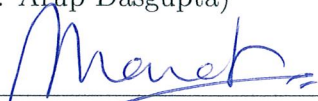
 Date: 05/07/19  
(Chairman- Dr. M. Kamruddin)

 Date: 5/7/18  
(Guide/Convener- Dr. R. Ramaseshan)

 Date: 5/7/18  
(External Examiner - Dr. K. R. Gunasekhar)

 Date: 05/07/19  
(Member 1: Dr. Tom Mathews)

 Date: 05/07/19  
(Member 2: Dr. Arup Dasgupta)

 Date: 05/07/19  
(Member 3: Dr. Sharat Chandra)

Final approval and acceptance of this thesis is contingent upon the candidate's submission of the final copies of the thesis to HBNI.

I hereby certify that, I have read this thesis prepared under my direction and recommend that it may be accepted as fulfilling the thesis requirement

Date: 5/7/19

Place: Kalpakam

  
(Dr. R. Ramaseshan)

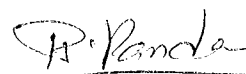
## STATEMENT BY AUTHOR

This dissertation has been submitted in partial fulfillment of requirements for an advanced degree at Homi Bhabha National Institute (HBNI) and is deposited in the Library to be made available to borrowers under rules of the HBNI.

Brief quotations from this dissertation are allowable without special permission, provided that accurate acknowledgment of source is made. Requests for permission for extended quotation from or reproduction of this manuscript in whole or in part may be granted by the Competent Authority of HBNI when in his or her judgment the proposed use of the material is in the interests of scholarship. In all other instances, however, permission must be obtained from the author.

Date: 05/07/2019

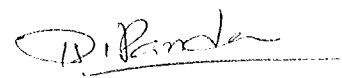
Place: Kalpakkam



**Padmalochan Panda**

## DECLARATION

I, hereby declare that the investigation presented in the thesis has been carried out by me. The work is original and has not been submitted earlier as a whole or in part for a degree / diploma at this or any other Institution / University.

  
Padmalochan Panda

# List of Publications

## (a) Journals:

1. **Padmalochan Panda**, R. Ramaseshan, N. Ravi, G. Mangamma, Feby Jose, S. Dash, K. Suzuki and H. Suematsu, “Reduction of residual stress in AlN films synthesized by magnetron sputtering technique”, *Materials Chemistry and Physics* **200** (2017) 78-84.
2. **Padmalochan Panda**, R. Ramaseshan, S. Tripura Sundari and H. Suematsu, “Anisotropic optical properties of a-axis AlN films : a spectroscopic ellipsometry study”, *OSA Continuum* **1** (2018) 1241-1250.
3. **Padmalochan Panda**, Nanda Gopala Krishna, Parasmani Rajput and R. Ramaseshan, “Local crystal structure and mechanical properties of sputtered Ti-doped AlN thin films”, *Phys. Chem. Chem. Phys.* **20** (2018) 29817-29825.
4. **Padmalochan Panda**, R. Ramaseshan, Madhusmita Sahoo, Nanda Gopal Krishna, A. K. Yadav, S. N. Jha and D. Bhattacharyya, “Local crystal structure in the vicinity of Cr in doped AlN thin films studied by X-ray absorption spectroscopy”, *Phys. Chem. Chem. Phys.* **20** (2018) 13084-13091.
5. **Padmalochan Panda** and R. Ramaseshan, “Effects of Cr doping on the mechanical properties of AlN films grown by the co-sputtering technique”, *Ceramics International* **45** (2019) 1755-1760.

## (b) Conference proceedings:

1. **Padmalochan Panda**, Bulusu Sravani, R. Ramaseshan, N. Ravi, Feby Jose, S. Dash and A.K. Tyagi, “Growth and characterization of highly oriented aluminum nitride films by DC reactive sputtering”, *AIP Conference Proceedings*, **1665** (2015) 080064.
2. **Padmalochan Panda**, R. Ramaseshan, Nanda Gopala Krishna and S. Dash, “Growth and characterization of a-axis oriented Cr-doped AlN films by DC magnetron sputtering”, *AIP Conference Proceedings*, **1731** (2016) 080038.

3. **Padmalochan Panda**, R. Ramaseshan, S. Tripura Sundari, R. Rajaraman, H. Suematsu and S. Dash, “Structural and Optical Properties of Sputtered AlN Thin Films”, *AIP Conference Proceedings*, **1832 (2017) 080061**.

### (c) Oral/Poster presentation:

1. R. Ramaseshan, **Padmalochan Panda**, S. Dash and A.K. Tyagi, “Synthesis and characterization of transition element based nitride thin films”, *Nano 15 - 2015 (K.S.Rangasamy College of Technology, Tiruchengode, Tamil nadu, India)*.
2. **Padmalochan Panda**, Madhusmita Sahoo, R. Ramaseshan, S. Tripura Sundari, H. Suematsu and S. Dash, “Local crystal structure and physical properties of sputtered Cr-doped AlN thin films”, *8th International Conference on Electroceramics - 2017 (Nagoya, Japan)*.
3. **Padmalochan Panda**, R. Ramaseshan, S. Tripura Sundari, N. Ravi and H. Suematsu, “Synthesis and characterization of oriented AlN thin films by transmission electron microscopy”, *International Conference on Microscopy and 39th Annual Meeting of EMSI-2017 (Mahabalipuram, India)*.
4. **Padmalochan Panda**, R. Ramaseshan, “Tuning of indentation hardness of AlN films by the Cr and Ti co-doping”, *Research Scholars Meet on Materials Science and Engineering of Nuclear Materials-HBNI, 2018 (IGCAR, Kalpakkam, India)*.

### (c) Other publications (Not Included in the Thesis)

1. K.G. Raghavendra, A. Dasgupta, P. Bhaskar, K. Jayasankar, C.N. Athreya, **Padmalochan Panda**, S.Saroja, V. SubramanyaSarma, R. Ramaseshan, “Synthesis and characterization of Fe-15 wt.%  $ZrO_2$  nanocomposite powders by mechanical milling”, *Powder Technology* **287 (2016) 190-200**.
2. Ch. Thirimal, **Padmalochan Panda**, R. Ramaseshan and P. Murugavel, “Non-Isothermal Crystallization kinetics and nanomechanical properties of Poly (vinylidene fluoride) - $La_{0.7}Sr_{0.3}MnO_3$  Nanocomposite Films”, *Adv. Sci. Eng. Med.* **8 (2016) 1-7**.

3. P. Arun kumar, **Padmalochan Panda**, M. Sribalaji, R. Ramaseshan, A. K. Keshri and K. Suresh Babu, "Enhancing the oxygen ionic conductivity of (111) oriented  $Ce_{0.80}Sm_{0.20}O_{2-\delta}$  thin film through strain engineering", *Electrochimica Acta*, **240** (2017) 437-446.
4. S. Anandh Jesuraj, P. Kuppusami, T. Dharini, **Padmalochan Panda**, Deepa Devapal, "Effect of substrate temperature on microstructure and nanomechanical properties of  $Gd_2Zr_2O_7$  coatings prepared by EB-PVD technique", *Ceramics International* **44** (2018) 18164-18172.
5. Renjith Ramachandran, Sujay Chakravarty, S. Balaji, **Padmalochan Panda**, C. David, R. Rajaraman, R. Ramaseshan, R. Govindaraj and G. Amarendra, "Study of vacancy defects and their thermal stability in MeV Fe ion irradiated RAFM steel using positron beam Doppler broadening spectroscopy", *Philosophical Magazine* **99** (2019) 38-54.
6. Madhusmita Panda, R. Krishnan, Kishore K. Madapu, **Padmalochan Panda**, Madhusmita Sahoo, R. Ramaseshan, Tripura Sundari, M. Kamruddin, Influence of particulate on surface energy and mechanical property of diamond-like carbon films synthesized by pulsed laser deposition, ", *Applied Surface Science* **484** (2019) 1176-1186



**Padmalochan Panda**



Dedicated  
To  
*Nature and My Family*



“Look deep into nature, and then you will understand  
everything better.” - Albert Einstein

## Acknowledgments

First and foremost, it is a pleasure to express my deepest gratitude to my supervisor, Dr. R. Ramaseshan for his guidance and encouragement throughout the course of present dissertation.

I would like to extend my sincere thanks to the doctoral committee members Dr. M. Kamruddin, Dr. Tom Mathews, Dr. Arup Dasgupta and Dr. Sharat Chandra for their comments and suggestions.

I would like to express my gratitude to Dr. A. K. Bhaduri and Dr. S.A.V. Satya Murty, present and past Director, IGCAR for permitting me to pursue Ph.D. at IGCAR. I am highly thankful to Dr. G. Amarendra, Dr. M. P. Janawadkar and Dr. C. S. Sundar, present and past Group Director, MSG for providing the conducive atmosphere for my smooth research. I would like to thank Dr. R. Rajaraman, Dr. N. V. Chandra Shekar and Dr. B. V. R. Tata, present and past Dean, Physical Sciences for their support. I would also like to thank Dr. Lakshmi Narasimman and Dr. M. Saibaba for the wonderful hospitality during my stay at JRF Enclave. I would like to acknowledge the Department of Atomic Energy for the research fellowship.

It is my pleasure to express my deepest gratitude to Dr. S. Tripura Sundari for fruitful discussions and help in carrying out ellipsometry experiments as well as manuscript and thesis corrections. I would like to extend my sincere thanks to Dr. S. K. Dhara for fruitful suggestions and manuscript corrections. I would also like to thank Dr. G. Rajendra Joshi for valuable suggestions and thesis corrections.

I would like to extend my sincere thanks to Prof. H. Suematsu, Nagaoka University of Technology, Japan, for TEM experiments, Dr. S. Ilango, Mrs. Sunitha and Mr. Magudapathy, for GIXRD experiments, Dr. G. Mangamma, for AFM experiments, Mr.

Nanda Gopal Krishna, for XPS experiments, Dr. Madhusmita Sahoo, Dr. A. K. Yadav, BARC, Dr. Parsmani Rajput, BARC, Dr. S. N. Jha, BARC. and Dr. D. Bhattacharya, BARC, for XAS experiments and analysis.

I would like to thank my seniors, friends and juniors Dr. Subrata Ghosh, Dr. Avinash Patsha, Dr. Bonu Venkatramana, Dr. T. R. Devidas, Dr. K. Srinivasan, Dr. K. G. Raghavendra, Dr. D. Karthickeyan, Ashok Bahuguna, Nilakantha, Lakshmanan, Irshad, Radhikesh, Vairavel, Zaibudeen, Manoj, Madhushmita, Shivang, Nidhin, Vikash, Santhosh, Santanu, Anil, Gopinath, Binaya, Dilip, Alok, Bijaya, Pradosh, Sekhar, Jeevraj for their suggestions, encouragement, friendship and help during these years.

Thanks to all my well wishers, all the members of the Materials Science Group and friends in the JRF enclave.

Finally, special thanks to Namrata (Sonu) for all her adoration and support for me for everything. I am thankful to God, my beloved parents and my whole family for their encouragement, unconditional love and blessings to overcome many barriers to reach the milestone of Doctor of Philosophy.

Thank you all for your love, patience and support to make it possible.

# Abstract

Aluminum nitride (AlN) is a wide band gap ( $\sim 6.2$  eV) semiconducting material with high thermal conductivity (up to 320 W/mK) and low thermal coefficient of expansion with high piezoelectric response. For these characteristics, thin film of AlN finds an important role in semiconductor industry, for example in high-temperature opto-electronic devices, surface acoustic wave devices and short-wavelength light source/detector applications. It is seen that plane orientation of AlN films also plays a vital role in device performance. For example, the extracted light intensity from *a*-plane or *m*-plane oriented AlN LEDs is 25 times higher than the conventional *c*-plane LEDs with shortest emission wavelength of 210 nm. Also, the surface acoustic velocity of *a*-axis oriented AlN film is higher than *c*-axis oriented AlN film. In addition, AlN films doped with transition metals such as Cr and Ti are also potential candidates for the spin-dependent photonic and electronic device applications.

Since, *a*-axis orientation AlN films have higher demand in many practical applications; it is therefore imperative and pertinent to optimize the growth condition to achieve the *a*-axis oriented AlN film and examine the nature of anisotropic optical properties for its better use in the area of optoelectronics. Similarly, several unique parameters such as doping concentration, position (substitution/interstitial) and the local environment of doping element play an essential role in the physical properties of doped-AlN films which is mainly controlled by the growth parameters. Therefore, the effect of dopant in the local crystal structure of AlN film needs close inspection to understand the mechanism of physical properties. Moreover, the physical contact loading during processing or packaging for the device applications generates plastic deformation which significantly deteriorates

the performance of the devices. Due to this AlN films as well as doped-AlN films require a vital comprehension in nano-mechanical properties.

AlN thin films have been grown at various growth temperatures ( $T_s$ , 35 to 600 °C) using reactive magnetron sputtering technique. The crystal structure, orientation, degree of columnar growth and residual stress of these films have been characterized using GIXRD, Rocking curve of XRD, TEM and  $\sin^2\psi$  technique, respectively. A preferential  $a$ -axis oriented AlN film with columnar structure has been grown at  $T_s$  of 400 °C. The residual stress measurement reveals the transition of stress from tensile to compressive between the  $T_s$  of 200 to 400 °C. The mechanical properties of the AlN films have been investigated by the nano-indentation technique. This study reveals that the variation of hardness ( $H$ ) was between 13.0 to 18.5 GPa, with the elastic modulus (238 GPa) relatively high for the  $a$ -axis oriented AlN film. Evolution of uniaxial anisotropic optical properties with  $T_s$  has been investigated by Phase Modulated Spectroscopic Ellipsometry (SE) technique with the photon energy ranging from 0.6 to 6.5 eV. It is observed that  $a$ -axis oriented AlN film exhibits nearly isotropic behavior with the birefringence ( $\Delta n$ ) as -0.01 at 210 nm compared to the  $c$ -axis counterpart with  $\Delta n$  value as -0.05 reported so far in the literature.

Ti and Cr doped AlN films have been grown at different doping concentrations using reactive co-sputtering technique. The doped films are crystallized with hexagonal wurtzite structure without the presence of any secondary phases belongs to doping elements. Surface chemical analysis is carried out using X-ray Photoelectron Spectroscopy. The influence of Ti and Cr atoms on the local crystal environment of the films have been systematically explored by X-ray Absorption Spectroscopy (XAS) measurement in BL-9 of Indus-II, RRCAT, India. It is observed that the insertion of transition metal replaces the Al atom in the AlN lattice and led to the localized distorted tetrahedron nitride

structure without any cluster formation. The bond length of doping element with N and Al in first and second co-ordination sphere have been extracted from the Extended X-ray Absorption Fine Structure (EXAFS) fitting. These bond lengths are found to decrease with doping concentrations. However, the rate of decrease in Cr doped films is relatively higher than Ti doped AlN films due to the strong of  $p$ - $d$  hybridization exist between the Cr - host atoms compared to the Ti - host atoms. The local crystal structure environment consequently governs the hardness of the doped films. It is observed that the hardness of Cr and Ti doped AlN films is increased from 17.5 GPa of pristine AlN to around 23 GPa and 27.6 GPa, respectively.

# Contents

	Page
<b>Abstract</b>	<b>x</b>
<b>1 Introduction</b>	<b>1</b>
1.1 Aluminum nitride (AlN) . . . . .	1
1.1.1 Crystal structure of AlN . . . . .	1
1.1.2 Phase diagram of AlN . . . . .	3
1.1.3 Properties and application of AlN films . . . . .	3
1.1.4 Growth of AlN films . . . . .	7
1.2 Transition metal doped AlN . . . . .	10
1.2.1 Properties and applications of $\text{Al}_{1-x}\text{Ti}_x\text{N}$ films . . . . .	11
1.2.2 Properties and applications of $\text{Al}_{1-x}\text{Cr}_x\text{N}$ films . . . . .	13
1.3 Motivation . . . . .	14
1.4 Objective and overview of the thesis . . . . .	16
<b>2 Experimental techniques</b>	<b>19</b>
2.1 Introduction . . . . .	19
2.2 Magnetron sputtering unit . . . . .	19
2.3 Growth of thin films . . . . .	21
2.3.1 Aluminum nitride (AlN) . . . . .	21
2.3.2 Ti doped AlN ( $\text{Al}_{1-x}\text{Ti}_x\text{N}$ ) . . . . .	22
2.3.3 Cr doped AlN ( $\text{Al}_{1-x}\text{Cr}_x\text{N}$ ) . . . . .	23
2.4 Characterization techniques . . . . .	23
2.4.1 X-ray Diffraction (XRD) . . . . .	23
2.4.2 Transmission Electron Microscopy (TEM) . . . . .	27
2.4.3 Atomic Force Microscopy (AFM) . . . . .	28
2.4.4 X-ray Photoelectron Spectroscopy (XPS) . . . . .	28
2.5 X-Ray Absorption Spectroscopy(XAS) . . . . .	30
2.5.1 Experimental details of XAS . . . . .	31
2.5.2 Theoretical background . . . . .	33
2.6 Nanoindentation . . . . .	35
2.7 Spectroscopic Ellipsometry (SE) . . . . .	38

<b>3</b>	<b>Effect of growth temperature on crystallographic orientation, mechanical and optical properties of AlN films</b>	<b>42</b>
3.1	Introduction . . . . .	42
3.2	Growth and crystallographic studies of AlN films . . . . .	43
3.2.1	GIXRD . . . . .	44
3.2.2	Cross sectional TEM and SAED . . . . .	47
3.2.3	Morphology and surface roughness by AFM . . . . .	49
3.3	Residual stress . . . . .	50
3.4	Mechanical properties . . . . .	54
3.5	Anisotropic optical properties of AlN films . . . . .	56
3.5.1	Modeling and fitting for the analysis of optical constant . . . . .	57
3.5.2	Behavior of anisotropic optical constant with growth temperatures	63
3.6	Conclusion . . . . .	68
<b>4</b>	<b>Significance of Ti on local crystal structure and mechanical properties of <math>\text{Al}_{1-x}\text{Ti}_x\text{N}</math> thin films</b>	<b>71</b>
4.1	Introduction . . . . .	71
4.2	Growth and crystallographic studies of $\text{Al}_{1-x}\text{Ti}_x\text{N}$ thin films . . . . .	72
4.3	Surface chemical analysis . . . . .	75
4.4	Morphology and surface roughness by AFM . . . . .	77
4.5	Local crystal structure at vicinity of Ti in AlN: XAS . . . . .	78
4.5.1	XANES analysis . . . . .	78
4.5.2	EXAFS analysis . . . . .	81
4.6	Mechanical properties . . . . .	84
4.7	Conclusion . . . . .	88
<b>5</b>	<b>Significance of Cr on local crystal structure and mechanical properties of <math>\text{Al}_{1-x}\text{Cr}_x\text{N}</math> thin films</b>	<b>90</b>
5.1	Introduction . . . . .	90
5.2	Growth and crystallographic studies of $\text{Al}_{1-x}\text{Cr}_x\text{N}$ thin films . . . . .	91
5.3	Surface chemical analysis . . . . .	94
5.4	Morphology and surface roughness by AFM . . . . .	96
5.5	Local crystal structure at vicinity of Cr in AlN: XAS . . . . .	97
5.5.1	XANES analysis . . . . .	97
5.5.2	EXAFS analysis . . . . .	100
5.6	Mechanical properties . . . . .	103
5.7	Conclusion . . . . .	108
<b>6</b>	<b>Summary and future directions</b>	<b>110</b>
6.1	Summary . . . . .	110
6.2	Future directions . . . . .	112



# List of Figures

1.1	Crystal structure of wurtzite AlN. . . . .	2
1.2	Phase diagram of AlN with temperature [14]. . . . .	3
1.3	Band structure and labelling of respective transitions for wurzite AlN. . .	6
1.4	Emission properties of GaN and AlN [27]. . . . .	7
1.5	Orientation diagram of AlN films under various sputtering pressures and TSD [12]. . . . .	9
1.6	Band diagram for group III-nitride and AlTiN with respect to the vacuum level [76]. . . . .	12
2.1	Photograph of the sputtering unit (MECA 2000-France) and the arrangement of guns covered by targets. . . . .	20
2.2	The schematic configuration of a common GIXRD. . . . .	25
2.3	Schematic of different angles of conventional rotation w.r.t diffractometer plane. . . . .	26
2.4	A typical normalized X-ray absorption spectrum. . . . .	31
2.5	Schematic of photoelectric effect, in which an x-ray is absorbed and a core level electron is ejected from the atom. . . . .	32
2.6	A schematic layout of XAS measurement unit. . . . .	33
2.7	Schematic illustration of indentation load-displacement curve with important measured parameters ([105]). . . . .	36
2.8	Schematic illustration of the unloading process showing contact geometry parameters ([105]). . . . .	37
2.9	Geometry of an ellipsometric measurement. . . . .	38
2.10	Schematic of the sample analysis procedure. . . . .	39
2.11	Schematic diagram of a phase modulated SE experiment setup. . . . .	40
3.1	GIXRD profiles of AlN thin films with different $T_s$ . . . . .	45
3.2	Rocking curve for (100) plane of AlN grown at 400 °C. . . . .	46
3.3	The variation of crystallite size of AlN thin films with different growth temperature ( $T_s$ ). . . . .	47
3.4	Dark-field cross-sectional TEM micrographs (a-d), corresponding SAED patterns (e-h) of AlN films grown at 35, 200, 400 and 600 °C, respectively and indexed SAED pattern of AlN film grown at 400 °C (i). . . . .	48

3.5	AFM images of AlN films on Si grown at (a) 35 °C, (b) 200 °C, (c) 400 °C and (d) 600 °C. . . . .	50
3.6	Residual stress of AlN thin films as a function of $T_s$ . . . . .	51
3.7	Hardness and modulus of AlN thin films as a function of $T_s$ . . . . .	55
3.8	Behavior of hardness as a function of crystallite size. . . . .	56
3.9	A schematic diagram of the ellipsometry experiment with the different azimuthal angles. . . . .	57
3.10	The extracted (a) $n$ and (b) $k$ at a different azimuthal angles for AlN film grown at 400 °C. . . . .	58
3.11	The measured (a) $I_s$ and (b) $I_c$ at a different incident angle for AlN film grown at 35 °C. . . . .	59
3.12	The measured (a) $I_s$ and (b) $I_c$ at a different incident angle for AlN film grown at 400 °C. . . . .	59
3.13	The measured (a) $\epsilon_r$ and (b) $\epsilon_i$ at a different incident angle for AlN film grown at 35 °C. . . . .	60
3.14	The measured (a) $\epsilon_r$ and (b) $\epsilon_i$ at a different incident angle for AlN film grown at 400 °C. . . . .	60
3.15	Experimental and corresponding fit of (a) $I_s$ , (b) $I_c$ for AlN film grown at 400 °C. . . . .	61
3.16	Film thickness measured by SE and TEM. . . . .	63
3.17	A plot of refractive index (a) $n_{\perp}$ , (b) $n_{\parallel}$ and extinction coefficient (c) $k_{\perp}$ , (d) $k_{\parallel}$ against to photon energy. . . . .	64
3.18	The variation of $n$ and $k$ value at 210 nm of AlN films with $T_s$ . . . . .	66
3.19	Optical band gaps of AlN films with $T_s$ for $k_{\perp}$ and $k_{\parallel}$ . . . . .	67
3.20	The dispersion of (a) birefringence ( $\Delta n$ ) (b) and dichroism ( $\Delta k$ ) with energy at different $T_s$ . . . . .	68
3.21	Dispersion parameters derived from the fitting with $T_s$ . . . . .	69
4.1	GIXRD profiles of $\text{Al}_{1-x}\text{Ti}_x\text{N}$ thin films with $x = 0, 1.5, 3$ and $4 \text{ at\%}$ . . .	73
4.2	W-H plots of $\text{Al}_{1-x}\text{Ti}_x\text{N}$ films with $x = 0$ and $4 \text{ at\%}$ . . . . .	74
4.3	High resolution XPS spectra of (a) Al 2p, (b) N 1s and (c) Ti 2p for $\text{Al}_{1-x}\text{Ti}_x\text{N}$ film with $x = 4 \text{ at\%}$ . . . . .	76
4.4	AFM images of $\text{Al}_{1-x}\text{Ti}_x\text{N}$ films at (a) $x = 0$ , (b) $x = 1.5$ , (c) $x = 3$ , and (d) $x = 4 \text{ at\%}$ . . . . .	78
4.5	Ti K-edge absorption spectra of $\text{Al}_{1-x}\text{Ti}_x\text{N}$ films. . . . .	79
4.6	Extended region fitting using ARTEMIS in R-space of $\text{Al}_{1-x}\text{Ti}_x\text{N}$ thin films. . . . .	81
4.7	(Ti-N) <sub>ax</sub> and (Ti-N) <sub>bs</sub> bond lengths are shown with Ti concentration of $\text{Al}_{1-x}\text{Ti}_x\text{N}$ films. . . . .	84
4.8	Indentation hardness as a function of depth of Si (100) substrate and $\text{Al}_{1-x}\text{Ti}_x\text{N}$ films with $x = 0$ to $4 \text{ at\%}$ . . . . .	85
4.9	Indentation modulus as a function of depth of Si (100) substrate and $\text{Al}_{1-x}\text{Ti}_x\text{N}$ films with $x = 0$ to $4 \text{ at\%}$ . . . . .	86

4.10	Indentation hardness and modulus of $\text{Al}_{1-x}\text{Ti}_x\text{N}$ films as a function of Ti concentrations. . . . .	87
4.11	AFM images of the indentation impressions at 2 mN load of $\text{Al}_{1-x}\text{Ti}_x\text{N}$ films with $x = 0$ and 4 at%. . . . .	88
5.1	GIXRD profiles of $\text{Al}_{1-x}\text{Cr}_x\text{N}$ thin films with $x = 0, 2, 4$ and 6 at% . . .	92
5.2	W-H plots of $\text{Al}_{1-x}\text{Cr}_x\text{N}$ films with $x = 0$ and 6 at%. . . . .	93
5.3	Core level XPS of (a) Al 2 <i>p</i> , (b) N 1 <i>s</i> and (c) Cr 2 <i>p</i> for $\text{Al}_{1-x}\text{Cr}_x\text{N}$ film with $x = 6$ at%. . . . .	95
5.4	AFM images of $\text{Al}_{1-x}\text{Cr}_x\text{N}$ films at Cr concentration of (a) $x = 0$ , (b) $x = 2$ , (c) $x = 4$ , and (d) $x = 6$ at%. . . . .	96
5.5	Cr K-edge absorption spectra of $\text{Al}_{1-x}\text{Cr}_x\text{N}$ films. . . . .	98
5.6	Extended region fitting using ARTEMIS in R-space of $\text{Al}_{1-x}\text{Cr}_x\text{N}$ thin films.	100
5.7	(Cr-N) <sub>ax</sub> and (Cr-N) <sub>bs</sub> bond length are plotted as the function of Cr concentration. . . . .	103
5.8	Indentation hardness as a function of depth of Si (100) substrate and $\text{Al}_{1-x}\text{Cr}_x\text{N}$ films with $x = 0$ to 6 at%. . . . .	104
5.9	Indentation modulus as a function of depth of Si (100) substrate and $\text{Al}_{1-x}\text{Cr}_x\text{N}$ films with $x = 0$ to 6 at%. . . . .	104
5.10	Indentation hardness and modulus of $\text{Al}_{1-x}\text{Cr}_x\text{N}$ films with Cr concentration.	105
5.11	AFM images of the indentation impressions at a peak load of 2 mN of $\text{Al}_{1-x}\text{Cr}_x\text{N}$ films with $x = 0$ and 6 at%. . . . .	107

# List of Tables

1.1	Comparison of physical properties of AlN and other semiconductor materials [1–5, 15, 16]. . . . .	4
1.2	Comparison of piezoelectric properties of AlN and other piezoelectric materials. . . . .	5
2.1	Deposition parameters of AlN thin films by DC sputtering. . . . .	22
2.2	Growth parameters of $\text{Al}_{1-x}\text{Ti}_x\text{N}$ thin films. . . . .	22
2.3	Growth parameters of Cr doped AlN films by reactive magnetron co-sputtering. . . . .	23
3.1	RMS roughness ( $R_{rms}$ ) and average grain size of these AlN films. . . . .	49
3.2	Residual stress of AlN films at different $T_s$ . . . . .	52
3.3	Thermal stress of <i>a-axis</i> and <i>c-axis</i> AlN films at different $T_s$ . . . . .	53
4.1	Crystallite size ( $D$ ) and strain ( $\epsilon$ ) of $\text{Al}_{1-x}\text{Ti}_x\text{N}$ thin films with $x = 0, 1.5, 3$ and $4 \text{ at\%}$ . . . . .	74
4.2	Binding energy of $\text{Al}_{1-x}\text{Ti}_x\text{N}$ thin films with references. . . . .	75
4.3	Pre-edge position of $\text{Al}_{1-x}\text{Ti}_x\text{N}$ films in Ti K-edge absorption spectra. . .	80
4.4	The fitting path parameters of $\text{Al}_{1-x}\text{Ti}_x\text{N}$ thin films . . . . .	83
5.1	Crystallite size ( $D$ ) and strain ( $\epsilon$ ) of $\text{Al}_{1-x}\text{Cr}_x\text{N}$ thin films with $x = 0, 2, 4$ and $6 \text{ at\%}$ . . . . .	93
5.2	Binding energy of different photoelectron peaks extracted from the $\text{Al}_{1-x}\text{Cr}_x\text{N}$ thin films with references. . . . .	94
5.3	$R_{rms}$ and average grain size of $\text{Al}_{1-x}\text{Cr}_x\text{N}$ films with different Cr concentration. . . . .	97
5.4	Pre-edge peak of $\text{Al}_{1-x}\text{Cr}_x\text{N}$ films in Cr K-edge absorption spectra. . . .	99
5.5	Fitted path parameters for the $\text{Al}_{1-x}\text{Cr}_x\text{N}$ thin films . . . . .	102

# Chapter 1

## Introduction

### 1.1 Aluminum nitride (AlN)

In the last two decades, aluminum nitride (AlN) has been attracted in the semiconductor industry due to their unique outstanding physical and optical properties with great technological advantages. AlN is a wide band gap ( $\sim 6.2$  eV) semiconducting material with high thermal conductivity (up to 320 W/mK), high melting temperature ( $\sim 3000$  °C), low thermal coefficient of expansion and high piezoelectric response [1–5]. For these characteristics, it has gained much interest in the semiconductor industry, for example; high-temperature opto-electronic devices, heat sink, surface acoustic wave devices and short-wavelength light source/detector applications.

#### 1.1.1 Crystal structure of AlN

AlN usually crystallizes in the hexagonal wurtzite structure (w-AlN) with  $P6_3mc$  (186) space group in ambient condition [1, 3, 6]. However, AlN has also metastable cubic zinc-blende (c-AlN) and cubic rock-salt crystal structures, which are stable at certain pressure conditions and at very small dimensions (nm) for example, in thin films on a suitable lattice matched substrates having coherent strain. This has been reported theoretically as well as experimentally with lattice parameter,  $a = 4.37$  Å (c-AlN) [6–10].

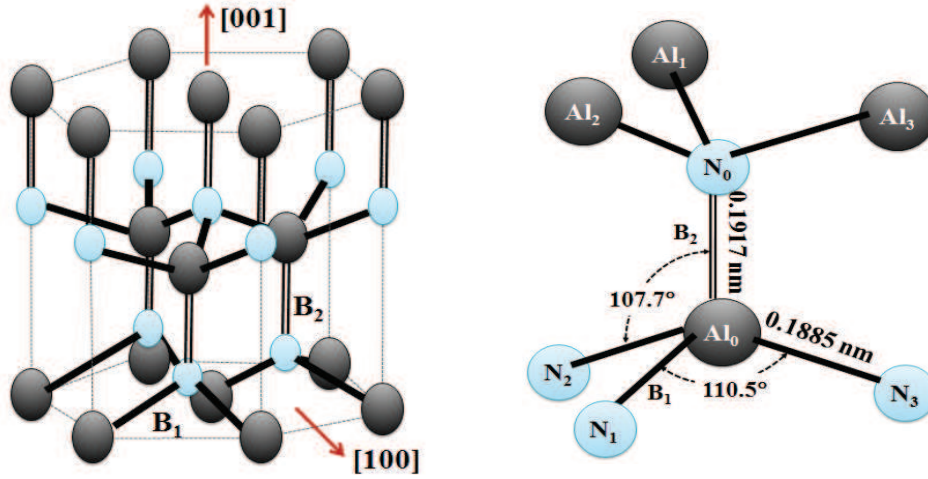
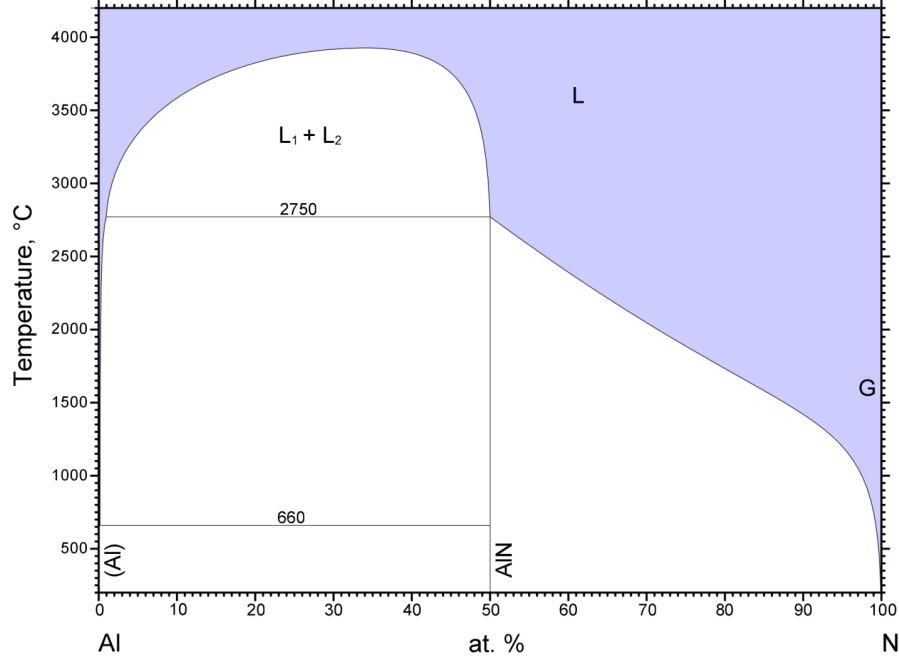


Figure 1.1 – Crystal structure of wurtzite AlN.

Hexagonal w-AlN is a direct band gap semiconductor in the group III-nitrides with close packed (h c p) structure having ABABAB stacking type sequence along  $c$ -axis [001], which is shown in Fig. 1.1. The lattice constants of w-AlN are  $a = 3.110 \text{ \AA}$  and  $c = 4.980 \text{ \AA}$ . In w-AlN, one Al atom is associated with four N atoms and forms a distorted tetrahedron structure. Among them, three Al-N<sub>(i)</sub> ( $i = 1, 2, 3$ ) bonds are named as B<sub>1</sub> at the base (bs-basal) with bond length  $1.885 \text{ \AA}$ , whereas one Al-N<sub>0</sub> bond in the  $c$ -axis direction is named as B<sub>2</sub> at the apex (ax-axial) with bond length  $1.997 \text{ \AA}$ . The bond B<sub>1</sub> is covalent in nature due to  $sp^3$ -hybridization between semi-full orbits of Al and N atoms, whereas bond B<sub>2</sub> is ionic character due to the coupling of Al empty orbit and N full orbit [11–13]. The (100) plane is composed of B<sub>1</sub> bonds which is stronger than (bonding energy) the B<sub>2</sub> bonds. The planes along [100], [010] and [110] direction are made up of B<sub>1</sub> type of bonds, whereas the planes along [001], [011] and [111] direction are made up of both B<sub>1</sub> and B<sub>2</sub> type of bonds. Thus, [001] direction possess more ionic character with lower bond energy than the other directions. The  $c/a$  ratio of w-AlN deviates from the theoretical ratio ( $c/a = 1.633$ ) of hexagonal crystal structure. Therefore, the dipole moments do not cancel each other along the  $c$ -axis due to the lack of centre of inversion symmetry and consequently give rise to the spontaneous polarization. Hence, AlN crystal

has polar face along [001] direction and non-polar along [100] direction [11–13].

### 1.1.2 Phase diagram of AlN



**Figure 1.2** – Phase diagram of AlN with temperature [14].

Hexagonal w-AlN forms at stoichiometric ratio of 50% Al and N atomic concentration which is shown in Fig. 1.2. Pristine AlN is stable at high temperatures in inert atmosphere and melts around 2750 °C, which is higher than the pure Al metal melting temperature (660 °C) [14]. With increase of N concentration, the melting temperature linearly decreases. In a vacuum, AlN decomposes at around 1800 °C, whereas the surface oxidation occurs above 700 °C in air atmosphere. AlN is also stable in hydrogen and carbon dioxide atmospheres up to 1000 °C.

### 1.1.3 Properties and application of AlN films

AlN is a wide band gap semiconducting material in group III nitrides for high temperature optoelectronic and deep ultraviolet (deep-UV) light source/detector applications.

The properties of AlN compared with other semiconductor materials, are shown in Table 1.1 [1–5, 15, 16]. A reasonable thermal match to Si, InP and InAs, make AlN (with high thermal conductivity) an attractive material for electronic packaging and heat-sink applications. Due to the similarity in crystal structure and lattice constant between AlN and GaN, the AlN film is also used as beneficial buffer layer for the growth of GaN films for optoelectronic devices [17]. AlN has good chemical stability, high hardness and high electrical resistivity ( $\geq 10^{10} \Omega\text{cm}$ ), hence it is used as a thermal dissipation, protection against environment and electrical insulation layers in opto-electronic devices.

Semi-conductors	Band gap (eV)	Transition type	Thermal conductivity (W/mK)	Coefficient of expansion ( $10^{-6}/^{\circ}\text{C}$ )
AlN	$\sim 6.2$	Direct	230-320	4.5
GaN	$\sim 3.4$	Direct	130-220	5.6
ZnO	$\sim 3.3$	Direct	43-54	2.9
Si	$\sim 1.1$	Indirect	140-160	4.1
InP	$\sim 1.3$	Direct	68	4.5
InAs	$\sim 0.4$	Direct	30-50	5.2
GaAs	$\sim 1.4$	Direct	45-54	6.5

**Table 1.1** – Comparison of physical properties of AlN and other semiconductor materials [1–5, 15, 16].

Moreover, highly oriented AlN thin film deposited on silicon, has received considerable attention recently as a piezoelectric material (piezo-coefficient,  $d_{33} = 5.6 \text{ pm/V}$ ) for surface acoustic wave (SAW) devices on the account of their high surface acoustic velocity, temperature stability, chemical stability characteristics compared to ZnO, LiNbO<sub>3</sub> and PZT, etc [18–22]. The piezoelectric properties of AlN are compared to other materials, are shown in Table 1.2 [18, 21, 23–25]. In w-AlN films, *a*-axis oriented AlN exhibits a higher acoustic velocity and electro-mechanical coupling coefficient than *c*-axis oriented AlN. Therefore, it is expected that *a*-axis oriented AlN film can perform better for SAW devices [26].



Piezoelectric materials	Acoustic velocity (m/s)	$d_{33}$ (pm/V)	Compatibility with Si technology
AlN	5600	5.6	Good
ZnO	2558	12.4	Fair
LiNbO <sub>3</sub>	3795	31.5	Poor
PZT	3104	200	Poor

**Table 1.2** – Comparison of piezoelectric properties of AlN and other piezoelectric materials.

Generally, the Ultraviolet (UV) light with wavelength shorter than 400 nm is divided into near-UV (300-400 nm), deep-UV (200-300 nm) and vacuum-UV ( $< 200$  nm) light. Since vacuum-UV light is absorbed by air, deep-UV light is the shortest wavelength that is available in the living environment. Deep-UV light has high energy to kill bacteria, viruses and decompose harmful stable substances (such as, dioxin, polychlorinated biphenyls-PCBs, etc). Therefore, these sources are used in water purification, sterilization and environmental protection devices. Also, it is used in high density optical data recording and nano-fabrication technologies, since they have low focal point of light due to lower wavelength [27]. Particularly, the wide direct band gap of AlN, GaN and ZnO semiconductors are favorable for short-wavelength light emitting and high-power devices. Deep-UV LEDs with high efficiency are expected to be a future candidate for the health care and industrial applications where AlN films find an important role with emission wavelength of 210 nm (shortest wavelength ever observed from any semiconductor) [28, 29]. According to DFT calculation (Ceperley-Alder exchange correlation potential) as well as experimental results (CL and deep UV laser PL), the degenerated  $p$ -type valence band maximum creates excitonic states due to the hexagonal crystal-field ( $\Delta_{cr} = -217$  meV) and spin-orbit splitting ( $\Delta_{so} = 20$  meV), as shown in Fig. 1.3 [30, 31]. Therefore, there are two configurations of excitonic transitions *i.e.*  $\sigma$  ( $E \perp c$ ;  $c$  – axis of wurzite structure) and  $\pi$  ( $E \parallel c$ ) configurations. Hexagonal w-AlN crystal has polar face along [001] direction, so the polarization of light strongly affects along the  $c$ -axis of the crystal.

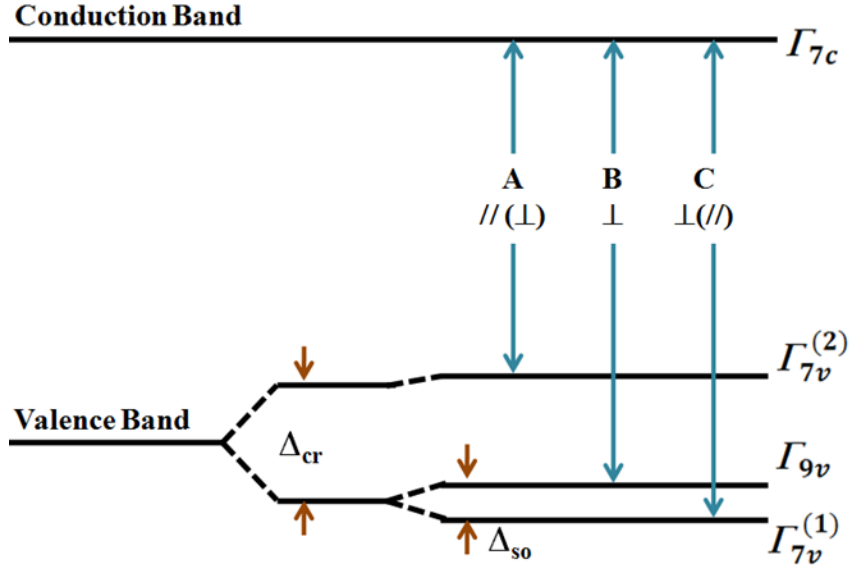


**Figure 1.3** – Band structure and labelling of respective transitions for wurzite AlN.

Gallium nitride (GaN) is used for blue LEDs in near-UV region with emission wavelength of 365 nm, whereas AlN is used for deep-UV source with a wavelength of 210 nm. It can be seen from Fig. 1.4 that like other semiconductors, GaN emits light uniformly from all crystal planes *i.e.* it shows isotropic emission pattern. However, AlN shows a directional light emission (strong optical polarization) properties [27–29]. For AlN, the ratio between the lattice constant ( $c/a$ ) is smaller compared to other nitride semiconductors due to their higher bond strength and ionicity with distorted structure. In general, the physical properties of semiconductors are very sensitive to crystal structural modification. Therefore, in *c-plane* AlN based deep UV-LEDs, the near band-edge emission is intrinsically weak along the normal to this plane due to strong polarization effect ( $E||c$ ). However, the extracted light intensity from *a-plane* or *m-plane* deep UV-LED shows 25 times higher compared to the conventional *c-plane* LED structures (along the surface normal) [28, 29]. The extracted light intensity from the plane of *a-plane* or *m-plane* LEDs, directly depends upon critical angle of light escape cone, which is inversely proportional to the square of refractive index [32]. The plane orientation is thus vital to the radiation properties of UV-LED and optoelectronic devices. From the view point of the growth of

thin films, AlN prefers to grow along  $c$ -plane predominantly rather than  $a$ -plane. Since,  $a$ -plane LED structures are desirable to enhance the light extraction and improve the emission efficiency, it is important to grow high quality  $a$ -plane oriented AlN films.

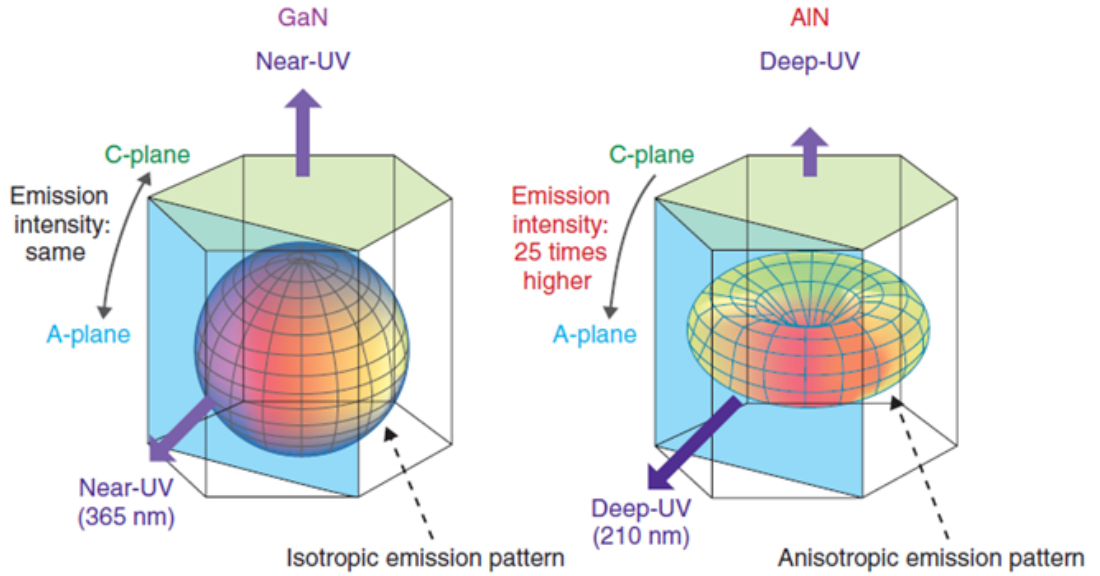


**Figure 1.4** – Emission properties of GaN and AlN [27].

#### 1.1.4 Growth of AlN films

In the past decades, an extensive research work has been carried out on the optimization of deposition by various coating techniques and deposition parameters in order to obtain the required reproducible quality thin films. Epitaxial growth of  $c$ -axis AlN has already been demonstrated such as, chemical vapor deposition on oriented AlN, molecular beam epitaxy on oriented GaN, Si and pulsed laser deposition on oriented molybdenum substrates [33–36]. In most techniques, the deposition temperatures are quite high, hence a smooth surface morphology and stress free epitaxial film could not be obtained due to the degradation of the substrates [37]. For surface acoustic wave (SAW) device applications, highly oriented films and homogeneous composition with low surface roughness is expected, since large surface roughness led to increase in propagation loss especially in

high frequency [38]. Reactive sputtering technique is promising under such circumstances when, low substrate temperature deposition (wide variety of substrate materials, compatible with current semiconductor device processes) and good surface finish as well as adhesion are required [39].

Whenever w-AlN is grown as a thin film using PVD or CVD, [002] oriented or polycrystalline AlN is most favoured. Thermodynamically grown AlN film also follows the same phenomena. The surface energy of (002) plane ( $\sim 5.6 \text{ Jm}^{-2}$ ) is higher than the surface energy of (100) plane ( $\sim 2.4 \text{ Jm}^{-2}$ ) in w-AlN [10]. Therefore, high energetic adatoms are favorable for the formation of (002) oriented plane, whereas low energetic adatoms are favorable for the formation of (100) oriented plane [13, 40]. Feby *et. al.* reported *a*-axis orientated AlN film growth for a target to substrate distance (TSD) of 18 cm and a growth temperature of 300 °C. The rocking curve of (100) plane shows a FWHM of 0.0145°, which confirms a highly oriented *a*-axis AlN film on Si(100) substrates [19]. Ishihara *et. al.* reported that AlN thin films grown with (100) orientation on Al and diamond substrates for a TSD of 12 to 15 cm and sputtering pressure of  $3 \times 10^{-3}$  mbar, whereas the (002) orientation is observed for a TSD of 6 to 10 cm with the same pressure as above [41]. The FWHM of the rocking curve for the AlN (002) peak shows  $\sim 0.2^\circ$ , that suggests that the AlN film highly oriented along the *c*-axis [42]. Xu *et. al.* have grown *a*-axis oriented AlN film on Si(111) substrate with increasing the pressure from 3 to  $12 \times 10^{-3}$  mbar at TSD of 4 cm. Also, they have grown *a*-axis oriented AlN film by increasing TSD from 3 to 12 cm at pressure of  $3 \times 10^{-3}$  mbar [12]. Similarly, Chen *et. al.* have also grown *a*-axis oriented AlN films on Si(100) substrates at a pressure of  $10^{-2}$  mbar with TSD as 6 cm [43]. In general, it is observed from literature that AlN films deposited at low TSD and low sputtering pressure exhibited (002) preferred orientation whereas those synthesized at high TSD and high pressure exhibited (100) orientation. The growth of

AlN film in different orientation by sputtering technique is shown in Fig. 1.5.

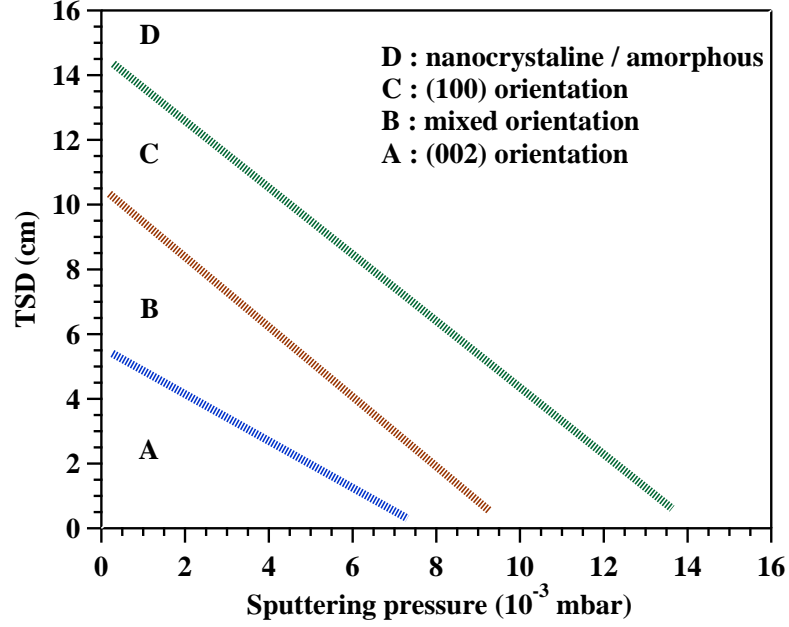


**Figure 1.5** – Orientation diagram of AlN films under various sputtering pressures and TSD [12].

The growth mechanism of AlN thin films can be understood based on the periodic bond-chain (PBC) approach. According to PBC, the mean free path ( $\lambda$ ) of sputtered atom (adatom) plays the crucial role in the growth of different orientation. When the  $\lambda$  is longer than the TSD, Al and N atoms deposited on the substrate directly without any collision. Therefore, at low sputtering pressure and TSD, the energy of the adatom has high kinetic energy that develops a higher nucleation density and grows along (002) plane orientation with faster rate. However, when the  $\lambda$  is smaller than the TSD, Al and N atoms form Al-N dimer in the plasma and reaches at substrate with many collisions. Therefore, at high sputtering pressure and TSD, the energy of the adatom has low kinetic energy that creates a lower nucleation density and grows along (100) plane orientation with faster rate compared to (002) plane. If the sputtering pressure and TSD are increased further, the Al and N atoms suffers too many collisions to reach the substrate

and have not enough energy to arrange in a crystalline hexagonal w-AlN structure. Thus, AlN films are found to be amorphous. This mechanism is called as ‘dimmer model’ or ‘nucleation density model’ [12, 41, 43].

Generally, the AlN film can be grown epitaxially on Si(111) substrates along  $c$ -axis. However, the growth of (100) AlN is favoured by the Si (100) substrates due to the following reasons. The lattice arrangements of Si(100) surface are known to be square and the atomic arrangement of (100) surface of AlN are rectangular. Therefore,  $a$ -axis oriented is relatively favorable compared to the  $c$ -axis oriented AlN films on Si(100) substrates [44, 45]. It is also reported that Al interlayer (few nm) is required to increase the adhesion strength between the film and Si substrate, which also favours the growth of AlN film along  $a$ -axis due to the reduction in lattice mismatch [46]. Similarly, high quality  $a$ -plane AlN epitaxial films are successfully deposited on  $r$ -plane sapphire using a thin ZnO buffer layer for surface acoustic wave (SAW) applications by magnetron sputtering [26, 47].

## 1.2 Transition metal doped AlN

In semiconductors, the charge of electrons play a crucial role in the information processing and communications, opto-electronic and high-frequency devices; whereas magnetic materials are used for the information recording using the spin of electron. To make use of both charge and spin of electrons in semiconductors for the device applications, transition metals (TM) are normally doped in nonmagnetic semiconductors to make dilute magnetic semiconductor (DMS) and they are attracted potentially in spintronic applications [48, 49]. The mechanism of the ferromagnetism is induced due to the indirect and double exchange interaction between the magnetic moments of partially filled  $d$  orbital

of TM with the host orbital which is caused by the virtual magnetic acceptor level and valence band transitions [49–53].

However, only few DMS materials are available with Curie temperature above the room temperature, which are essential from the view point of both fundamental research and practical applications. Following theoretical predictions and experimental results, TM doped wide band gap semiconductors (ZnO, SnO<sub>2</sub>, TiO<sub>2</sub>, GaN and AlN) were attracted considerable attention in spin-dependent photonic and electronic devices due to their intrinsic ferromagnetism above room temperature [49, 54–56]. Among them, AlN is a wide band gap semiconductor with a high thermal conductivity and melting temperature which are compatible with the modern day microelectronics. AlN is chemically stable at high temperatures and demonstrates a high solubility for transition metals. First row transition metals (Sc, Ti, V, Cr, Mn, Fe, Co and Ni) are used to dope AlN lattice to change its physical properties for the application in lasers, deep UV to UV LEDs, sensor, UV polarizer, high-temperature optoelectronic displays and spin-tunneling devices in the wavelength span of 200 to 375 nm by band-gap-engineering [28, 51–54, 57–65].

### 1.2.1 Properties and applications of Al<sub>1-x</sub>Ti<sub>x</sub>N films

Ti doped AlN films have revealed as n-type ferromagnetic material for dilute magnetic semiconductor applications at room temperature, reported by first principle calculation as well as experimental methods [66–69]. Addition of transition elements to AlN such as Ti, Cr and Zr have yielded ternary nitrides with higher hardness, superior oxidation resistance, good wear and corrosion resistance [70–73]. This improvement in performance manifested as a decrease in flank wear and corresponding increase in life time of the tool during drilling, cutting tests of aerospace components and long-life surface modified

membranes.  $\text{Al}_{1-x}\text{Ti}_x\text{N}$  can be grown using sputtering technique at low temperature on various substrates including metals.  $\text{Al}_{0.9}\text{Ti}_{0.1}\text{N}$  film deposited on optical fiber is used as infrared whispering gallery modes microlaser in the range of 775 to 800 nm for the biomedical applications [74, 75].

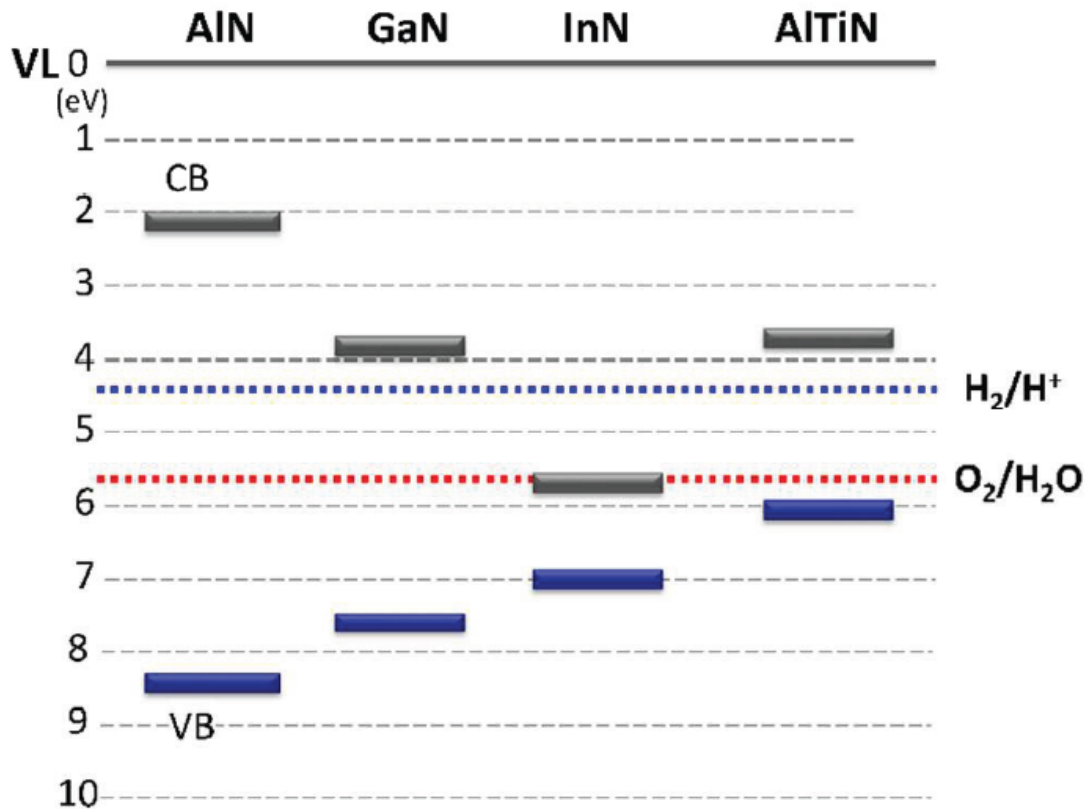


**Figure 1.6** – Band diagram for group III-nitride and AlTiN with respect to the vacuum level [76].

An extensive research is going on for highly efficient hydrogen gas production by tuning the band gap energy of wide band gap semiconductors via photo-electrochemical water splitting. For example,  $\text{TiO}_2$  is used potentially for the hydrogen generation via photo-electrochemical water splitting [76, 77]. However, the band gap of  $\text{TiO}_2$  is too wide to absorb a significant portion of the solar spectrum and the valence band potential is too low for effective oxidation of water. While exploring the possibility of heavy transition metal doping to group III nitride materials for photoelectric conversion under visible light,



Tatemizo *et. al.* observed that heavily Ti doped AlN absorbs blue-green light with production of photo-current [76]. Band diagram of group III-nitrides and AlTiN with respect to vacuum level are shown in Fig. 1.6 compared to the water oxidation and hydrogen reduction potentials. It implies that the potential at the top of the VB for AlTiN films meet the precondition of the water oxidation. Thus, It is expected that Ti doped AlN films might be desirable for efficient photoelectric conversion applications[76]. Addition of Ti to AlN lattice reveals the improvement of larger piezoelectric response with better thermal stability of frequency resistance [78].

### 1.2.2 Properties and applications of $\text{Al}_{1-x}\text{Cr}_x\text{N}$ films

According to density functional theory (DFT) calculation, Cr doped AlN exhibits a huge magnetic moment of  $3 \mu_B/\text{Cr}$  originating from the significantly high  $p-d$  exchange interaction between the  $p$ -orbital of host semiconductor (solvent) and the  $3d$  shells of magnetic dopant ions (solute) owing to indirect exchange interaction [49, 64, 79].  $\text{Al}_{1-x}\text{Cr}_x\text{N}$  is reported to exhibit DMS properties with high Curie temperature ( $T_c \geq 800 \text{ K}$ ) by experimental as well as first principle calculation [64, 65, 79]. Ferromagnetic Cr doped AlN is used as a potential material in the spin light emitting diode (polarized), barrier layers for spin-tunnelling devices, lasers and high-temperature devices with a wide range of possibility of band-gap-engineered structures [53, 61, 63, 80]. Additionally, the piezoelectric response of Cr doped AlN films is 73% higher than that of the pristine AlN [81].

High resistance to wear, corrosion and oxidation properties of materials with high thermal stability are important in many different industrial applications. In the past decades, nitride-based compounds ( $\text{Ti}_{1-x}\text{Al}_x\text{N}$ ,  $\text{Al}_{1-x}\text{Cr}_x\text{N}$ , and  $\text{Ti}_{1-x}\text{C}_x\text{N}$ ) have been extensively investigated due to their excellent tribological and mechanical performances [19, 72, 82–

87]. It is reported that  $\text{Al}_{1-x}\text{Cr}_x\text{N}$  compound synthesized by various physical vapor deposition techniques with  $x = 17$  to  $79 \text{ at}\%$  having hardness between 20 to 41 GPa [72, 84–87].

### 1.3 Motivation

AlN has high technological demand in deep-UV LED, since it has the shortest emission wavelength 210 nm. It is seen that the plane orientation of AlN films also play a vital role in device performance. For example, the extracted light intensity from *a*-plane or *m*-plane oriented AlN LEDs is 25 times higher than the conventional *c*-plane LEDs. Also, the surface acoustic velocity of *a*-axis oriented AlN film is higher than *c*-axis oriented, that is expected to show a better performance in SAW devices. Thus, it is important to optimize the growth conditions and to develop high quality *a*-axis oriented AlN films. It is also important to examine the nature of anisotropic optical properties of these films for its better use in the area of opto-electronics. Although there are few reports available on the anisotropic optical properties of AlN thin films, which are confined to *c-axis* oriented films only [88–92]. Therefore, it is imperative and pertinent to examine the nature of refractive index of *a-axis* oriented AlN thin films over a broad range of wavelengths starting from deep UV to NIR.

Transition metal doped AlN films are the potential source of magnetic semiconductors for spin-dependent photonic and electronic device applications. For example, Cr doped AlN films are the well known dilute magnetic semiconductor (DMS) with high Curie temperature,  $T_c \geq 800 \text{ K}$ . According to density functional theory (DFT) calculation, Cr doped AlN exhibits a huge magnetic moment ( $3 \mu_B/\text{Cr}$ ) compared to other transition metal dopants. However, the experimentally observed magnetic moment was less

than  $1 \mu_B/\text{Cr}$ , due to possible role of Cr clusters, nitrogen vacancies, defects and impurities for the different Cr concentration in AlN lattice [52, 54, 64]. Though Cr ionic radii is larger than the Al atom, still it can settle in the interstitial sites of AlN lattice. Formation of Cr clusters at interstitial sites reduce the total magnetic moment, which increases the antiferromagnetic states [79, 80]. Cui *et. al.* have reported using DFT calculation that the Cr clusters larger than 2 atoms exhibit antiferromagnetic coupling [79]. Hence, the growth of cluster less doped AlN thin films is the first step to achieve the DMS property in these systems. Also, piezoelectric response of Cr doped AlN films is 73% higher than that of the pristine AlN. Similarly, Ti doped AlN films also exhibit room temperature DMS property and are desirable for the efficient photoelectric conversion devices as well. However, several unique parameters such as doping concentration, position (substitution/interstitial) and the local environment of doping element play an essential role in the physical properties of doped AlN films which is mainly controlled by the growth parameters. Therefore, the effect of dopant in the local crystal structure of AlN film needs a fundamental investigation using X-Ray Absorption Spectroscopy (XAS).

Addition of transition metals to AlN such as Ti, Cr and Zr have yielded ternary nitride compounds with higher hardness, superior oxidation resistance, good wear resistance and corrosion resistance. On the other hand, AlN shows a high solubility for transition metals with high chemical stability upto high temperatures. Doping of transition metals ( $< 15 \text{ at\%}$ ) in wurtzite hexagonal AlN (at the Al site) has considerable demands in the areas of opto-electronics and more specifically in dilute magnetic semiconductor (DMS) device applications. Moreover, the physical contact loading during processing or packaging for the opto-electronic device applications generates plastic deformation which significantly deteriorates the performance of the devices. In this regard, a systematic study of mechanical properties of transition metals (Ti and Cr) doped AlN thin films has not been

explored. Due to this, AlN films as well as doped AlN films require a vital comprehension in nano-mechanical properties.

## 1.4 Objective and overview of the thesis

The prime aim of the present thesis is to grow *a*-axis oriented AlN film and understand the effects of growth temperature on residual stress and mechanical properties. Additionally, It emphasizes the anisotropic optical properties of *a-axis* oriented AlN films over a broad range of wavelengths starting from deep UV to NIR. This thesis also highlights the growth of Ti and Cr-doped AlN films, the local crystal structure and the mechanical properties with respect to doping concentration. The thesis is organized in to six chapters and the contents of each chapter are summarized as follows.

**Chapter 1** briefly introduces the crystal structure, general properties and applications of pristine AlN as well as doped AlN films. A progress and present status of growth of *a*-axis oriented AlN thin films and their applications are briefly introduced.

**Chapter 2** provides a description of the magnetron sputtering system used for the growth of pristine and doped (Ti and Cr) AlN thin films. The growth parameters used for the synthesis of these films are described in detail. These films are characterized by X-Ray Diffraction (XRD), Transmission Electron Microscopy (TEM), Atomic Force Microscopy (AFM), and X-Ray Photoelectron Spectroscopy (XPS) to investigate the crystallographic, structural, morphological and chemical properties. Local crystal structure at the vicinity of doping elements are characterized by X-Ray Absorption Spectroscopy (XAS) and the working principle is briefly presented in this section. Also a brief introduction to

the characterization techniques used for the mechanical and optical properties of these thin films (using nano-indentation technique and Spectroscopic Ellipsometry (SE), respectively) and their basic principle are also presented.

**Chapter 3** presents the growth of AlN thin films with different growth temperatures ( $T_s$ , 35 to 600 °C), deposited by reactive sputtering technique. This chapter primarily concerned with the growth of *a*-axis oriented AlN thin films and it is obtained at a growth temperature of 400 °C. Also, this chapter reports the residual stress in AlN films for different growth temperatures which is measured by the  $\sin^2\psi$  technique and exhibits a transition from tensile to compressive between 200 to 400 °C. Nano-indentation hardness ( $H$ ) of these films with respect to the growth temperature showed a variation between 12.8 to 19.0 GPa. However, *a*-axis oriented AlN film exhibits relatively a high elastic modulus, such as  $E = 237.6$  GPa. Optical characterization of these thin films are discussed with the help of SE technique in the broad range of energy, which is a non-invasive non-contact technique with a high degree of accuracy. This chapter also presents an elaborate study on the anisotropic optical properties of AlN films with respect to growth temperatures, in the photon energy range of 0.6 to 6.5 eV. It is observed that the birefringence ( $\Delta n = -0.01$ ) of *a*-axis oriented AlN film is relatively lower compared to the *c*-axis oriented AlN film ( $\Delta n = -0.05$  at 210 nm) reported in the literature so far.

**Chapter 4** presents the growth of Ti doped AlN ( $\text{Al}_{1-x}\text{Ti}_x\text{N}$ ) films by reactive co-sputtering technique with different Ti concentrations ( $x = 0, 1.5, 3$  and  $4$  at%). The surface chemical analysis and morphology of these films are studied by XPS and AFM technique. This chapter fundamentally explores the local crystal structure around the Ti dopant in AlN lattice, which is investigated by X-ray absorption spectroscopy. It is observed that Ti forms localized TiN species with distorted tetrahedron structure by

replacing Al atom in AlN lattice leading to increase in tensile strain. The coordination number of Ti with N atom in first coordination sphere shows a stoichiometry nature *i.e* around four, similar to pristine AlN. The bond lengths  $(\text{Ti-N})_{ax}$ ,  $(\text{Ti-N})_{bs}$  are found to be moderately decreased with Ti concentration, whereas Ti-Al bond length in second coordination sphere is independent of Ti. Finally, this chapter describes the effect of Ti doping on the mechanical properties of AlN thin films, where the hardness of  $\text{Al}_{1-x}\text{Ti}_x\text{N}$  films are increased from 17.5 to 27.6 GPa with increase in doping concentration.

**Chapter 5** presents the growth of Cr doped AlN ( $\text{Al}_{1-x}\text{Cr}_x\text{N}$ ) films by reactive co-sputtering technique with different Cr concentrations ( $x = 0, 2, 4$  and  $6 \text{ at\%}$ ). The surface chemical analysis and morphology of these films are also studied by XPS and AFM techniques. From X-ray absorption spectroscopy study, it is observed that Cr also replaces the Al atom in AlN lattice and forms localized distorted tetrahedron CrN species as similar to Ti doped AlN films. These films have both N and Al vacancies in the first and second coordination sphere, respectively. The bond lengths  $(\text{Cr-N})_{ax}$  and  $(\text{Cr-N})_{bs}$  are found to be decreasing rapidly with Cr concentration and shows a strong  $p - d$  hybridization compared to Ti doped AlN films. Therefore, the modulus enhanced from 231 to 313 GPa with the increase in Cr concentration. The hardness of  $\text{Al}_{1-x}\text{Cr}_x\text{N}$  films is varying between 17.5 to 23.0 GPa and show a lower hardness compared to Ti doped AlN due to more Al and N vacancies and large crystallite size.

**Chapter 6** summarizes the research contribution and the major findings of this thesis. In addition, few issues that will be tackled in the near future are also indicated.

# Chapter 2

## Experimental techniques

### 2.1 Introduction

This chapter provides a brief description of the magnetron sputtering system used for the growth of thin films and the characterization techniques such as X-ray Diffraction (XRD), Transmission Electron Microscopy (TEM), Atomic Force Microscopy (AFM), and X-ray Photoelectron Spectroscopy (XPS) to investigate the crystallographic, structural, morphological, chemical and elemental analysis. The growth parameters used for the synthesis of thin films (AlN, Cr doped AlN and Ti doped AlN) in this research work are explained in detail. Local crystal structure at the vicinity of doping elements (Cr and Ti) in AlN thin films are characterized by X-ray Absorption Spectroscopy (XAS), which is briefly presented in this section. A brief introduction of the characterization techniques used for the mechanical and optical properties of these thin films using nano-indentation technique and Spectroscopic Ellipsometry (SE), respectively are given.

### 2.2 Magnetron sputtering unit

In this research work, thin films are grown using reactive magnetron sputtering technique (M/s. MECA 2000, France). The main parts of the system are the high vacuum chamber

(diameter: 630 mm and height: 500 mm) housing three magnetron guns (two RF and one DC source), six substrate holders of 4 inch diameter and thickness monitor. This system is pumped by a turbo molecular pump (Leybold-Germany, pumping speed 1100 lit/min) backed by a rotary pump (Leybold-Germany). This system is also equipped with mass flow controllers for gas and suitable vacuum measuring gauges. During sputter deposition, a thousand position gate valve (VAT, Switzerland) with a stepper motor controlled by a VAT PM-5 (Switzerland) controller is maintained the working pressure in the chamber according to the feed back signal obtained from the capacitance manometer (Baratron, MKS). This VAT PM-5 controller is capable of operating in two modes namely (i) constant pressure mode and (ii) constant position mode. Fig.2.1 depicts the photograph of this sputtering unit.



**Figure 2.1** – Photograph of the sputtering unit (MECA 2000-France) and the arrangement of guns covered by targets.

This sputtering unit has three magnetron guns with 50 mm diameter and 5 mm thickness targets with pneumatic shutters. Among these, two are RF powered with LCR match boxes and third one is with DC powered, baked by water cooled system to reduce the heat during the deposition. Two RF sources are powered by Hutttinger 600 RF and the DC source is powered by Hutttinger 1500 DC. These three guns are placed by focusing towards the substrate at an angle  $30^\circ$  from the normal for co-sputtering of three targets simultaneously. A non-magnetic shield is used to separate the targets for avoiding



cross contamination at the time of co-sputtering (Fig. 2.1). A quartz crystal monitor MAXTEK, INC (USA) is used to monitor the thickness of the coating on the fly. It also contains a stationary substrate heater to grow thin films at different temperatures upto 800 °C. The important deposition parameters to grow thin films with desired properties are sputtering power, sputtering pressure, gas flow, target to substrate distance (TSD) and substrate temperature.

## 2.3 Growth of thin films

### 2.3.1 Aluminum nitride (AlN)

AlN thin films were grown on silicon (100) substrates by DC reactive magnetron sputtering technique from pure aluminum target (4N) of 50 mm diameter in a high purity argon (5N) and nitrogen (5N) gas mixture. Si (100) substrates were cleaned by a standard two-step RCA process *i.e.* at first soaked in a solution of  $\text{H}_2\text{O} : \text{NH}_4\text{OH} : \text{H}_2\text{O}_2$  (5:1:1) at 70 °C and then etched in a 2% HF- $\text{H}_2\text{O}$  solution for 2 minutes to remove the native oxide layers on the surface. Before deposition, the sputtering chamber was evacuated to  $1 \times 10^{-6}$  mbar. At first, a mono layer of Al in Ar atmosphere was deposited on the substrate for few seconds to improve the adhesion between the substrate and deposited AlN thin films. These films were grown at different growth temperatures (substrate temperature,  $T_s$ ) by keeping constant Ar/ $\text{N}_2$  gas ratio, target to substrate distance (TSD) and deposition pressure. The deposition parameters in this study are listed in Table 2.1. Surface profilometer Dektak 6M (M/s.Veeco, USA) was used to measure the thickness of these films, and it was found to be around 1  $\mu\text{m}$ .

Sputtering parameters	Values
Target	Al (4N pure)
Substrate	Si (100)
Deposition pressure (mbar)	$5 \times 10^{-3}$
TSD (cm)	14
Ar : N <sub>2</sub> (sccm)	4 : 1
DC power (W)	200
Growth temperature ( $T_s$ ) (°C)	35 to 600

**Table 2.1** – Deposition parameters of AlN thin films by DC sputtering.

### 2.3.2 Ti doped AlN ( $\text{Al}_{1-x}\text{Ti}_x\text{N}$ )

$\text{Al}_{1-x}\text{Ti}_x\text{N}$  thin films were grown on Si(100) substrate by reactive magnetron co-sputtering technique from 50 mm diameter Al and Ti targets (4N pure) in pure argon and nitrogen gas (5N pure) atmosphere. These Si (100) substrates were also cleaned by the standard two-step RCA process as described earlier. Before deposition, the base pressure of sputtering chamber was maintained below the pressure of  $6 \times 10^{-6}$  mbar by turbo-molecular pump.  $\text{Al}_{1-x}\text{Ti}_x\text{N}$  films were grown at constant flow of argon to nitrogen ratio, TSD and growth temperature with changing the Ti sputtering power, which are listed in Table 2.2. Surface profiler was used to determine the thickness of  $\text{Al}_{1-x}\text{Ti}_x\text{N}$  films and it was found to be around 400 nm.

Sputtering parameters	Values			
Target (4N)	Al and Ti			
TSD (cm)	7			
Ar : N <sub>2</sub> (sccm)	4 : 1			
Growth temperature (°C)	400			
Power (Al:Ti)(W)	200:0	200:30	200:50	200:70
Sputtering pressure ( $10^{-3}$ mbar)	5	7	7.6	8
Ti at%	0	1.5	3	4

**Table 2.2** – Growth parameters of  $\text{Al}_{1-x}\text{Ti}_x\text{N}$  thin films.

### 2.3.3 Cr doped AlN ( $\text{Al}_{1-x}\text{Cr}_x\text{N}$ )

$\text{Al}_{1-x}\text{Cr}_x\text{N}$  thin films were grown on Si (100) substrate by reactive magnetron co-sputtering technique from a 50 mm diameter Al and Cr targets (4N pure) in high purity argon and nitrogen gas (5N pure) mixture as described for growth of  $\text{Al}_{1-x}\text{Ti}_x\text{N}$  thin films. The deposition parameters in this study are listed in Table 2.3. The thickness of these films were measured by surface profilometer and it was found to be around 450 nm.

Sputtering parameters	Values			
Target (4N)	Al and Cr			
TSD (cm)	7			
Ar : N <sub>2</sub> (sccm)	4 : 1			
Growth temperature (°C)	400			
Power (Al:Cr)(W)	200:0	200:30	200:40	200:50
Sputtering pressure ( $10^{-3}$ mbar)	5	7	7.3	7.6
Cr at%	0	2	4	6

**Table 2.3** – Growth parameters of Cr doped AlN films by reactive magnetron co-sputtering.

## 2.4 Characterization techniques

### 2.4.1 X-ray Diffraction (XRD)

XRD is a powerful and easy technique to investigate the phase formation and the crystal structure of the materials. The basic components of an XRD instrument are the X-ray source, the detector and its control unit. Since X-ray wavelength is comparable to the lattice spacing of materials, it diffracts from parallel plane of atoms. This diffraction occurs, when the path difference of the scattered X-rays from successive atomic planes is an integral multiple of the wave length ( $\lambda$ ) of the X-ray [93]. The condition is known as Bragg's law of diffraction and is expressed as equation 2.1.

$$n\lambda = 2d\sin\theta \quad (2.1)$$

where  $\lambda$  is the wavelength of X-ray used (normally Cu  $K_\alpha$ ,  $\lambda = 1.54056 \text{ \AA}$ ),  $\theta$  is the diffraction angle and  $d$  is the inter planar spacing. In a diffraction pattern, the recorded intensity is plotted against the diffraction angle  $2\theta$ . Each diffracted peak correlates to a plane in the crystal structure.

The penetration depth of X-ray beams in Bragg-Brentano mode XRD, ranges from a few micrometers to a few hundred micrometers, depending on the density of the material. As a result of this, the Bragg Brentano configuration generally produces intense signal from the substrate and weak signals from the film itself. By using a very small grazing angle for the incident rays, the penetration depth of X-rays can be limited to a few nanometers *i.e.* X-rays interaction volume confine to a few tens to hundreds of nanometers from the surface of thin film [94]. Thus, grazing incidence X-ray diffraction (GIXRD) is commonly used to investigate the significant surface and interface structure of thin films to avoid the substrate information. Fig. 2.2 depicts the schematic diagram of the GIXRD arrangement. In the present study, the identification of crystalline phases of thin films were carried out by Bragg-Brantano (Cu -  $K_\alpha$ ) geometry and Grazing Incidence X-ray Diffraction (GIXRD) technique (M/s. Bruker D8, Germany) with a grazing angle of  $0.5^\circ$ .

However, in thin films, the peak width of XRD profile consists of both crystallite size and strain component. Hence, to delineate the effect of microstrain and crystallite size on the peak broadening, Williamson-Hall (W-H) method is used. Mean crystallite size and strain of the film are calculated from XRD profiles using the following equation.

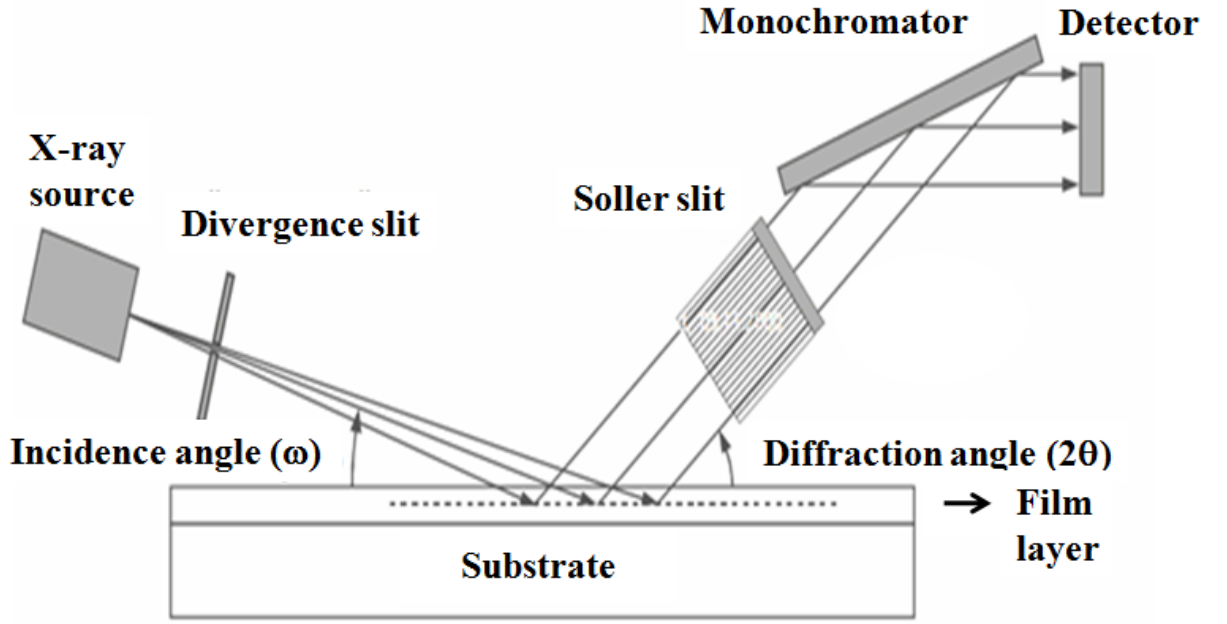


**Figure 2.2** – The schematic configuration of a common GIXRD.

$$\beta \cos \theta = \frac{K\lambda}{D} + 4\epsilon \sin \theta \quad (2.2)$$

where  $K$  is the Scherrer constant (0.9),  $D$  is the crystallite size,  $\beta$  is the Full Width at Half Maximum (FWHM) and  $\epsilon$  is the induced strain in the film [95].

#### 2.4.1.1 Rocking curve ( $\omega$ -Scan)

In XRD, there are three conventional angle of rotation ( $\omega$ ,  $\phi$  and  $\psi$ ) in different direction with respect to diffractometer plane, which is shown in Fig. 2.3. Whereas,  $\omega$  is the angle between incident X-rays and film surface,  $\phi$  is the in-plane rotation of the film and  $\psi$  is the azimuthal tilt.

The degree of preferred orientation of a crystallographic plane of film and its crystal quality can be determined by rocking curve measurement of XRD. In this measurement, the X-ray source and the detector angle ( $2\theta$ ) are fixed for a particular Bragg peak. The

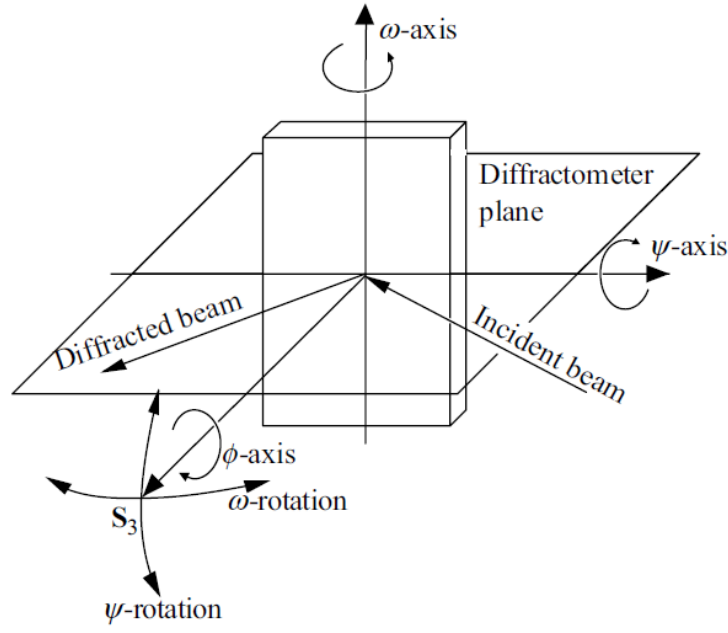


**Figure 2.3** – Schematic of different angles of conventional rotation w.r.t diffractometer plane.

diffraction intensity is measured by the rocking ( $\omega$ -rotation) of film surface around the Bragg peak [93, 94]. The degree (or distribution) of preferred orientation is estimated from the FWHM of the rocking curve profile which is discussed in section 3.2.1.

#### 2.4.1.2 Residual stress

A well-documented  $\sin^2\psi$  technique is used to measure the residual stress of thin films, where the crystallographic planes tilted from the surface normal at different  $\psi$  angles. Usually, the lattice spacing varies with the strain of elastically strained crystalline material. There is a correlation exists between the stress components in the film and variation in the inter-planer spacings ( $d$ ) for the tilt angles ( $\psi$ ) along the diffraction vector is shown below

$$\sigma_\phi = \frac{E}{(1 + \nu) \sin^2\psi} \left( \frac{d_i - d_0}{d_0} \right) \quad (2.3)$$

where  $E$  - Young's modulus,  $\nu$  - Poisson's ratio,  $\left( \frac{d_i - d_0}{d_0} \right)$  - micro-strain,  $\sigma_\phi$  is the stress

in the film.[93, 96]. In this  $\sin^2\psi$  technique, various tilt angles ( $\psi$ ) are used to measure the residual stress of these films. Also, in-plane rotation  $\phi = 0, 45$  and  $90^\circ$  of the samples are used to obtain a three dimensional stress distribution in the system.

### 2.4.2 Transmission Electron Microscopy (TEM)

TEM is an unique material characterization technique that enables investigation of high resolution microstructural features with magnified images of the order of  $10^3$  to  $10^6$  as well as acquisition of crystallographic information. In principle, TEM uses near relativistic electron beam normally accelerated by hundreds of kV supply voltage. Normally, e-beam interacts with target specimen in three ways *i.e.* unscattered electrons (transmitted/direct beam), elastically scattered electrons (diffracted beam) and inelastically scattered electrons [97]. The transmission of e-beam without any interaction with the specimen is inversely proportional to the specimen thickness. Depending on the mode of operation, a sophisticated system of electromagnetic lenses focuses the scattered electrons into an image or a diffraction pattern. The directions of coherent elastic scattered electrons are determined by the crystallographic orientation between the atomic planes of the specimen and the incident beam. By selecting the diffracted beam from a selected area on the specimen, selected area electron diffraction (SAED) pattern can be obtained. The SAED pattern is equivalent to an X-ray diffraction pattern. A single crystal leads to a well arranged spot pattern on the screen; a poly-crystal constitutes a ring pattern. Whereas, an amorphous material produces a series of diffuse halos. General analysis of the samples can be carried out by different modes of the TEM, such as the bright field and dark field images, SEAD patterns, high resolution TEM (HRTEM) and fast Fourier transform (FFT) images. Images formed from the transmitted electrons are known as bright field images and images formed using specific diffracted ( $hkl$ ) beams are known

as dark field images. They yield information about both atomic structure and defects present in the material. Thus TEM is definitely a useful and effective tool to characterize the thin films to investigate the crystal structure, phase and orientation.

In this study, the cross section samples for transmission electron microscopy have been prepared using a focused ion beam system (JIB-4500, JEOL, Japan). Cross sectional microstructural studies were performed using a transmission electron microscopy (M/s JEM-2100F, JEOL, Japan ) operating at 200 kV.

### 2.4.3 Atomic Force Microscopy (AFM)

The AFM is widely used for the study of surface morphology with an order of atomic scale spatial resolution. The AFM probes consists of sharp tip of the order of 10 nm, which is used for probing interactions between the tip and surface of the sample. The common force associated with AFM interaction is the inter atomic force called as van der Waals force and it depends on the separation between the tip and the sample. The small forces between the tip and specimen during the scan will cause a deflection on the cantilever. A laser beam is focused on the back of a cantilever and this will be detected by a position sensitive photo diode. By raster-scanning of the tip across the surface and recording the change in force as a function of position to map the morphology of the surface. In this study, the surface morphology of these films was characterized by an AFM (M/s. Anton Paar, Switzerland) with a contact cantilever single-crystal silicon tip of size 10 nm.

### 2.4.4 X-ray Photoelectron Spectroscopy (XPS)

The XPS, also known as electron spectroscopy for chemical analysis (ESCA) is a widely used surface sensitive technique to investigate the compositional elements and its chem-



ical state. In this technique, a surface of specimen is irradiated with X-rays of known energy (commonly Al  $K\alpha$  or Mg  $K\alpha$ ) in ultra high vacuum. In this technique, the irradiated photons interact with the core-level electrons of the atom. When the incident energy ( $h\nu$ ) is greater than the binding energy ( $E_b$ ) of the electron in a particular shell, a photo-electron is ejected with a kinetic energy ( $E_k$ ), which is represented in the following equation.

$$E_k = h\nu - E_b - \phi \quad (2.4)$$

where  $\phi$  is the work function of the material. These ejected photo-electrons are collected by an electron analyzer that measures their kinetic energy. An electron energy analyzer produces an energy spectrum *i.e.* intensity against binding energy (number of photo-electrons with time) [98].

For the present study, a monochromatic Al  $K\alpha$  radiation with 1486.71 eV, at an operating power 300 W was used. The emitted photoelectrons were analyzed by a hemispherical analyzer with 150 mm mean radius. The spectrometer was calibrated using a standard silver sample. The data obtained were processed by the Specslab2 software. The binding energy of C-1s spectrum from contaminated carbon at 284.7 eV was used as a reference to account for any charging of the sample. The peak positions were compared with standard values for identification of different elements. The pass energy, incident and detection angles in XPS with respect to the sample surface normal are 50 eV, 55° and 0°, respectively. Ar<sup>+</sup> ion beam with 1 keV and current 0.5 mA were employed to sputter few nm layers of the film surface to clean the specimen.

## 2.5 X-Ray Absorption Spectroscopy(XAS)

X-ray absorption spectroscopy (XAS) generally deals with measurement of absorption coefficient as a function of x-ray photon energy around an absorption edge of an element in a material. X-ray absorption spectrum is broadly classified into two important parts i.e. X-ray absorption near-edge structure (XANES) and extended x-ray absorption fine structure (EXAFS) after the edge, which is shown in Fig. 2.4. XANES is sensitive to three-dimensional geometrical arrangements (symmetry e.g. octahedral, tetrahedral co-ordination) of atoms around x-ray absorbing atom in the host material [99]. It is also helpful in determining the chemical oxidation state of the absorbing atom. On the other hand, EXAFS is generally characterized by the presence of fine structure oscillations and gives precise information about local structure around the particular atomic species in the short range order. This determination is confined to a distance given by the mean free path of the photo-electron within 5-7 Å radius from the element. On the basis of above characteristic, the EXAFS is a powerful structural local probe to determine the bond length, coordination number, disorderness in the co-ordination sphere of the absorbing atom.

Normally, the energy of x-rays are ranging from  $\sim 500$  eV to 500 keV (wavelengths from  $\sim 25$  to  $0.25$  Å). At this energy range, an electron absorbs photon in a tightly bound quantum core level of an atom. The incident x-ray energy must be greater than the binding energy of a particular core level of an absorbing atom, so that the electron will be removed from its quantum level. In this case, excess energy is given to a photo-electron that is ejected from the atom as seen in Fig. 2.5.

With the advent of modern synchrotron radiation sources, XAS technique has emerged

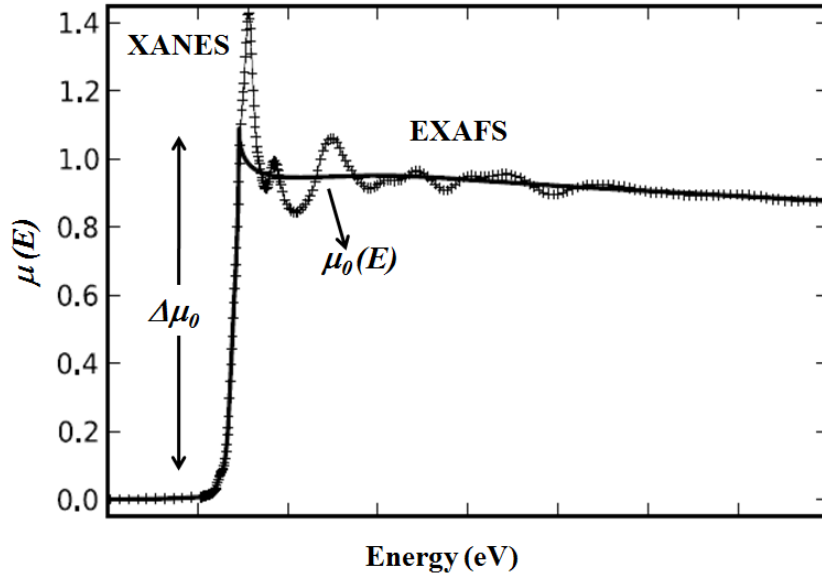


**Figure 2.4** – A typical normalized X-ray absorption spectrum.

to be the most powerful local structure determination technique, which can be applied to any type of material *i.e.* amorphous, polycrystalline, polymers, surfaces and liquids in ambient condition. XAS can be measured either in transmission or fluorescence geometries. In transmission mode, the absorption coefficient ( $\mu$ ) is measured as a function of  $\log(I_0/I)$ , where  $I_0$  is the intensity of incident x-rays and  $I$  is the intensity of transmitted beam through specimen. Usually, fluorescence geometry is preferable in thin films deposited on thick substrate. In this mode,  $\mu$  is measured as a function of  $(I_f/I_0)$ , where  $I_f$  is the intensity of fluorescence x-rays.

### 2.5.1 Experimental details of XAS

XAS measurement with synchrotron radiation is generally carried out in two different modes viz., scanning and dispersive. In this study, doped (Cr and Ti) AlN films were studied by the standard  $45^\circ$  geometry fluorescence mode at BL-09, which is a scanning XAS beamline, of the Indus-2 Synchrotron source (2.5 GeV, 200 mA) at Raja Ramanna Centre for Advanced Technology (RRCAT), Indore, India. The beam-line consisted of

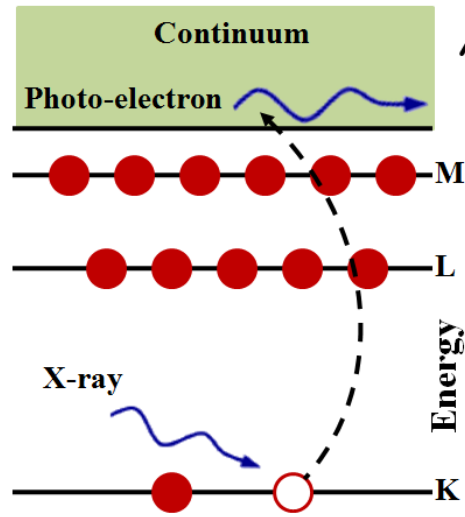


**Figure 2.5** – Schematic of photoelectric effect, in which an x-ray is absorbed and a core level electron is ejected from the atom.

an Rh/Pt coated collimating meridional cylindrical mirror followed by a Si (111) ( $2d = 6.2709 \text{ \AA}$ ) based double crystal monochromator (DCM). The energy resolution ( $E/\Delta E$ ) of this beam line is  $10^4$ . For the fluorescence measurements, one ionization chamber of length 300 mm was used to measure the incident photon flux intensity, and a solid state detector was used to measure the fluorescent photon intensity. Schematic of a typical XAS measurement is shown in Fig. 2.6. Before measurement, the photon energy scale was calibrated by measuring XAS spectrum of a standard Ti and Cr metal foil. The absorption spectra were carried into ATHENA software package and normalized to unit edge step. Generally, the self-absorption influences the EXAFS amplitude data due to high penetration depth of incident beams in thick and high concentrated samples. Therefore, these experimental spectra were checked for self-absorption influences by Booth algorithm in ATHENA, giving the input as angle of beams with the film thickness [100]. The self-absorption effect for the XANES spectrum also cross-checked with Fluo algorithm by using the chemical formula of Ti and Cr doped AlN film, incident and outgoing angles of beam as input parameters [101, 102]. It confirms that these films have no self-absorption effects, since there is no contrast between experimental and corrected

self-absorption spectrum.

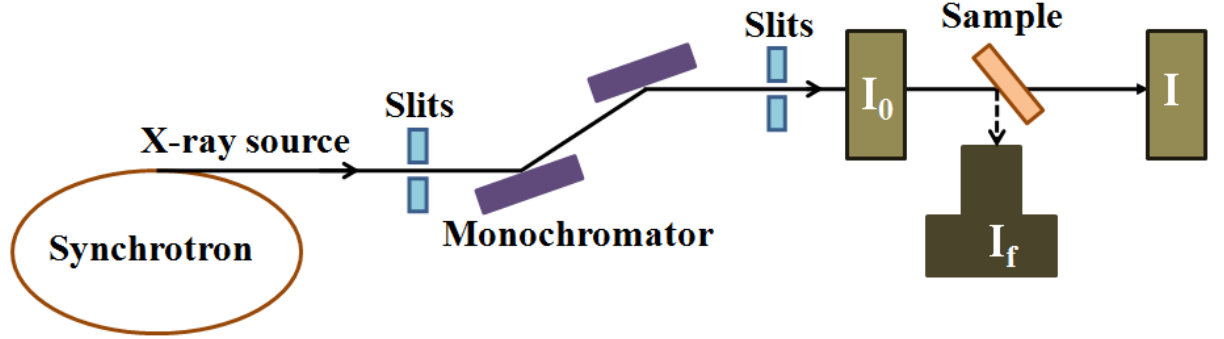


**Figure 2.6** – A schematic layout of XAS measurement unit.

### 2.5.2 Theoretical background

Core-electron absorbs the incident x-ray ( $E$ ) and jumps to continuum state with a kinetic energy of  $E - E_0$ , where  $E_0$  is the binding energy of core-electron. The core state is eventually filled by ejecting a fluorescent x-ray or an Auger electron. The photo-electron propagates in continuum state and get backscattered from the surrounded several neighboring atoms. Photo-electrons and the final state of the photo-electron can be described, by the superposition of the original and scattered waves. This leads to an interference phenomenon that modifies the interaction probability between core electrons and incident photons. Constructive interference increases while destructive interference decreases the absorption coefficient of the atom. This interference phenomenon depends on the distance between emitting and scattering atoms, their atomic mass and coordination numbers. Since the oscillations in the absorption spectra are important in EXAFS, the oscillation part of the measured absorption co-efficient ( $\mu(E)$ ) was converted to the fine structure function  $\chi(E)$  using the following equation.

$$\chi(E) = \frac{\mu(E) - \mu_0(E)}{\Delta\mu_0(E_0)} \quad (2.5)$$

where  $E_0$  is the threshold energy,  $\mu_0(E)$  is the the smooth background function as the absorption of an isolated atom and  $\Delta\mu_0(E)$  is the edge step in the absorption. Analysis of EXAFS is done in  $k$ -space by converting the absorption co-efficient  $\chi(E)$  to  $k$ -space ( $\chi(k)$ ) using the following relation.

$$k = \sqrt{\frac{2m(E - E_0)}{\hbar^2}} \quad (2.6)$$

where  $m$  belongs to mass of the electron,  $\chi(k)$  is weighted by  $k^3$  for amplification of oscillations to compensate the damping of the amplitude of XAFS oscillation at high  $k$ . Under the dipole approximation, an analytical expression of the EXAFS signal can be derived as the relationship shown below [103].

$$\chi(k) = \sum \frac{N_j f_j(k) e^{-2k^2 \sigma_j^2} e^{-\frac{2R_j}{\lambda}}}{k R_j^2} \text{Sin}[2kR_j + \delta_j(k)] \quad (2.7)$$

where,  $N_j$  is the number of  $j^{th}$  neighbors of the absorbing atom at a distance of  $R_j$ , having a scattering amplitude of  $f_j$  and phase of  $\delta_j$ . The term  $\sigma_j$  represents the fluctuation at the atomic positions (having both structural as well as thermal effect) and  $\lambda$  is the mean free path of the scattering photo-electron.

Crystal structure parameters from the EXAFS signal are determined by fitting the experimental EXAFS spectra with the above theoretical expression.  $\chi(R)$  versus radial distances ( $R$ ) plots are used to extract the co-ordination number, radial distances and neighbouring atoms of the dopant in different co-ordination spheres. Different codes for EXAFS data analysis programme are available among which, IFEFFIT package is mostly used [104]. The goodness of the fit has been measured by minimizing a statistical parameter; known as R-factor, which is defined by the equation shown below.

$$R = \frac{\sum_{i=\min}^{\max} [Re(\chi_d(r_i) - \chi_t(r_i))^2 + Im(\chi_d(r_i) - \chi_t(r_i))^2]}{\sum_{i=\min}^{\max} [Re(\chi_d(r_i))^2 + Im(\chi_d(r_i))^2]} \quad (2.8)$$

The theoretical scattering path of a absorbing element in specimen is generated with FEFF modelling using ARTEMIS for the fitting the experimental data, which has IFEFFIT integrated with it [104].

## 2.6 Nanoindentation

Nano-indentation is a novel and versatile technique developed over the past three decades to investigate the local mechanical properties of extremely small volume of bulk materials and thin films. In a traditional indentation experiment, an indenter is pressed into a specimen with a known load and is subsequently removed. Generally, It measures the hardness, modulus, and stiffens of a material and also allows the depth resolved indentation from a surface to sub-surface. The hardness of the material is defined as the load divided by residual indentation area and the indentation impression is only a few nanometers in depth. Its attractiveness stems largely from the fact that mechanical properties can be determined directly from indentation load and displacement measurements without the need to image the hardness impression.

The nano-indentation system consists of a precision loading arrangement and accurate measurement of displacement having high thermal stability. The precision loading could be accomplished by electromagnetic deflection of a spring and the displacement could be measured by a capacitance gauge or Linear Variable Differential Transformer (LVDT). In nano-indentation, the most commonly used tip is the Berkovich tetrahedral diamond with sharp three sided point like tip. The hardness ( $H$ ) and elastic modulus ( $E$ ) are calculated

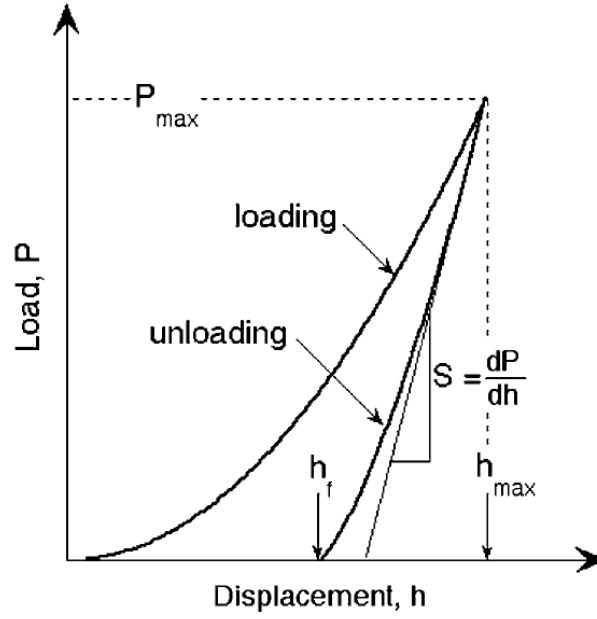


**Figure 2.7** – Schematic illustration of indentation load-displacement curve with important measured parameters ([105]).

from the load displacement profile of indentation test using Oliver and Pharr formalism [105]. A schematic representation of a typical load displacement curve obtained with a Berkovich indenter is presented in Fig. 2.7, where the  $P$  and  $h$  belongs to the load and displacement of the indenter. Deformation during loading is assumed to be both elastic and plastic in nature as the permanent hardness impression forms. During unloading, it is assumed that only the elastic displacements are recovered. From the  $P - h$  curve, the maximum load ( $P_{max}$ ) and the maximum displacement ( $h_{max}$ ) must be measured. The slope of the upper portion of the unloading curve during the initial stages of elastic unloading is called stiffness, which is defined by  $S = dP/dh$ . The parameter  $h_f$  is the final depth of penetration after the indenter is fully unloaded.

The indentation contact area is measured on the unloading process to find the  $H$  and  $E$  of a material, which is shown schematically in Fig. 2.8. During the indentation, the specimen surface displaces at the contact perimeter from the initial surface is defined by  $h_s = \epsilon \frac{P_{max}}{S}$ , where  $\epsilon$  is a constant that depends on the geometry of the indenter. The



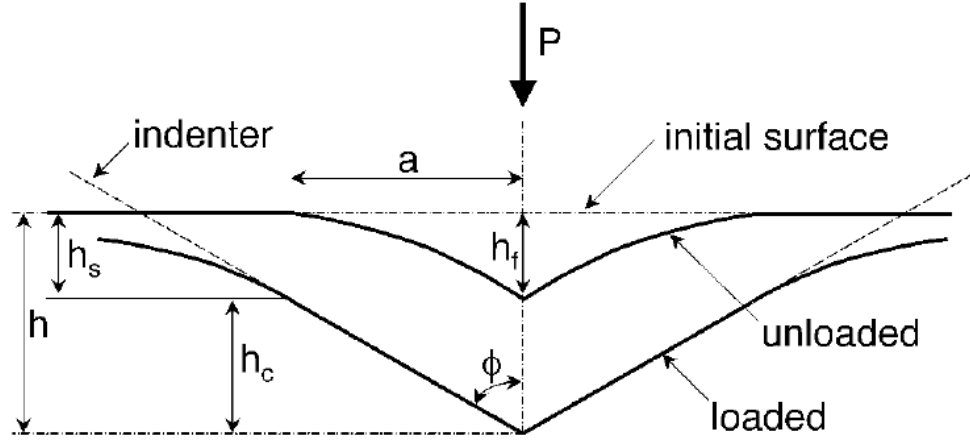


**Figure 2.8** – Schematic illustration of the unloading process showing contact geometry parameters ([105]).

vertical displacement of the contact periphery *i.e.* the depth along which contact is made between the indenter and the specimen is denoted by  $h_c$  ( $h_c = h_{max} - h_s$ ) and it is;

$$h_c = h_{max} - \epsilon \frac{P_{max}}{S} \quad (2.9)$$

Assuming  $F(d)$  be an area-function that describes the cross sectional area of the indenter at a distance  $d$  back from its top of the tip, the contact area ( $A$ ) is defined as  $A = F(h_c)$ . From the contact area, the hardness is estimated from the relationship shown below,

$$H = \frac{P_{max}}{A} \quad (2.10)$$

The measured stiffness is related to the contact area as  $S = \sqrt{\frac{4\pi}{A}} E_{eff}$ , where  $E_{eff}$  is the effective elastic modulus defined by the below equation.

$$\frac{1}{E_{eff}} = \frac{1 - \nu^2}{E} + \frac{1 - \nu_i^2}{E_i} \quad (2.11)$$

The indentation modulus  $E$  can be extracted by giving the elastic constants of indenter ( $E_i$ ), Poisson's ratio of the specimen ( $\nu$ ) and indenter ( $\nu_i$ ) as input in above relation.

In this study, the nano-mechanical properties of pristine and doped AlN thin films were carried out by a compact platform Ultra Nano-indentation Tester (M/s. Anton Paar, Switzerland) equipped with a three sided pyramidal diamond (Berkovich) tip with an end radius of 30 nm. Indentation was performed as a function of depth (10 nm to 650 nm) at different linear load with the standard process *i.e.* the loading and unloading rates are maintained at twice of the peak load.

## 2.7 Spectroscopic Ellipsometry (SE)

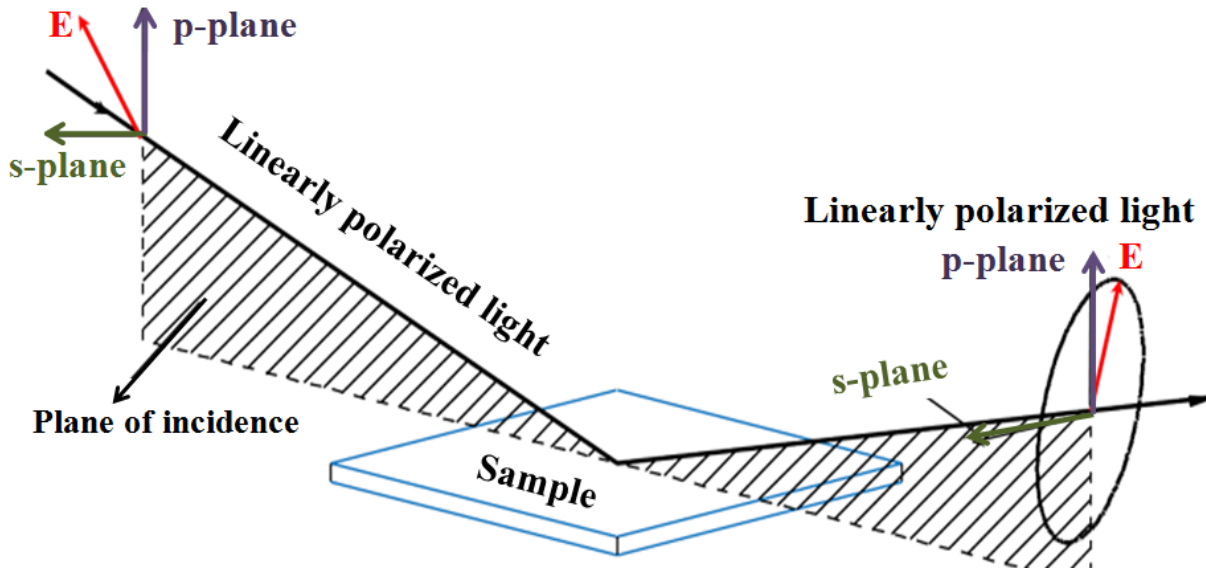


**Figure 2.9** – Geometry of an ellipsometric measurement.

Spectroscopic Ellipsometry (SE) measurement is a powerful unique optical characterization technique to determine the optical properties of materials in the broad energy range, which is a non invasive, non-contact and sensitive technique with a high degree of accuracy [106]. SE is commonly used to measure optical properties of solids such as refractive index, extinction co-efficient, and dielectric constant. SE measures the change in polarization state of a linear polarization light as it reflects from the sample of the interest.

The polarization change between the parallel ( $p$ ) and perpendicular ( $s$ ) components of the reflected light with respect to the plane of incidence is represented as the change in amplitude ( $\Psi$ ) and the phase difference ( $\Delta$ ), which are considered as ellipsometric parameters, are shown in Fig. 2.9. The ellipsometric parameters  $\Psi$  and  $\Delta$  are related to the ratio of reflection coefficients is shown below

$$\rho = \frac{r_p}{r_s} = e^{i\Delta} \tan \Psi \quad (2.12)$$

where  $r_p$  and  $r_s$  are the parallel and perpendicular reflection coefficients, respectively.

In this experiment,  $I_s$  and  $I_c$  are the experimentally measured parameters from which the pseudo dielectric constants are computed. These are related to  $\Psi$  and  $\Delta$  in the following equation below.

$$I_s = \sin(2\Psi)\sin(\Delta) \quad \text{and} \quad I_c = \sin(2\Psi)\cos(\Delta) \quad (2.13)$$

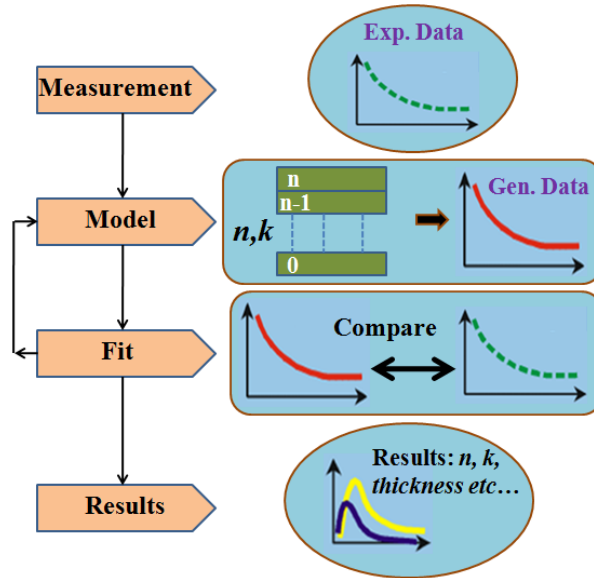


**Figure 2.10** – Schematic of the sample analysis procedure.

The optical characteristics of materials are extracted through suitable optical modeling to experimental measured  $I_s$  and  $I_c$  values, which is shown in Fig. 2.10. In the first

step, it is necessary to create a theoretical model of the material of interest for data analysis. This model needs to include the order of the layers, their optical constants and thickness (unknown physical parameters). These values are not known, hence an initial guess should be provided with the basic knowledge in SE. The model should also contain some known parameters, such as wavelength, polarization state, and the angle of incident light. The next step in data analysis is to vary the unknown physical parameters and generated data from the model by successive iterations until one finds the set of variable parameters which yield a calculated data that closely match the measured optical data. This has to evaluate the best-fit model in order to decide whether the predicted model is physically reasonable and whether all the parameters are unique and not correlated. It is then understood that these set of parameters represents the true physical description of the sample under study.

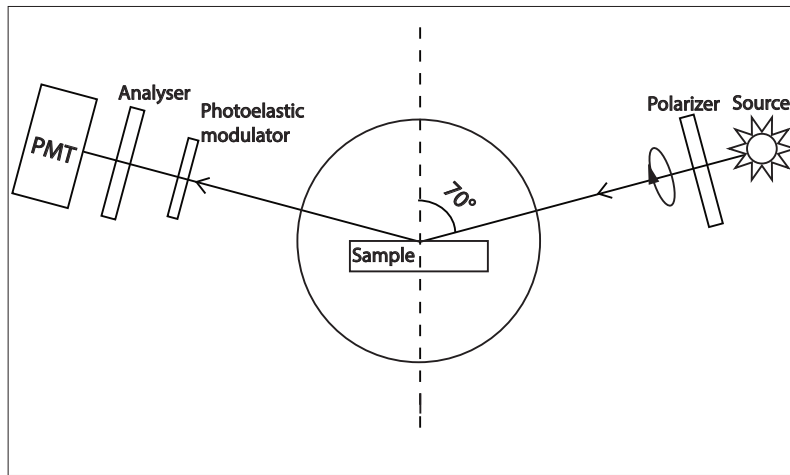


**Figure 2.11** – Schematic diagram of a phase modulated SE experiment setup.

A classical non-linear minimization regression analysis was performed by the Levenberg Marquardt algorithm to carry out the fitting of experimental data using the model to describe the sample. A high resolution goodness of fitting by the root-mean-square error ( $\chi^2$ ) is defined as;

$$\chi^2 = \frac{1}{2N - P - 1} \sum_{i=1}^N \left[ \left( \frac{I_{s,m_i} - I_{s,c_i}}{10^{-2}} \right)^2 + \left( \frac{I_{c,m_i} - I_{c,c_i}}{10^{-2}} \right)^2 \right] \quad (2.14)$$

where  $N$  is the number of data points,  $P$  is the number of parameters to be fitted and indices  $m_i$  and  $c_i$  are the measured and computed quantity of the  $i_{th}$  energy of ellipsometry parameters [107].

In this study, the SE parameters are measured in ambient conditions by a phase modulated Spectroscopic Ellipsometer (M/s. Horiba Jobin-Yvon, UVISSEL2, France) at an incident angle of  $65^\circ$ ,  $70^\circ$  and  $75^\circ$  in the photon energy range of 0.6 to 6.5 eV with 0.01 eV increment as shown in Fig. 2.11. The data analysis and fittings are performed using DeltaPsi2 software.

# Chapter 3

## Effect of growth temperature on crystallographic orientation, mechanical and optical properties of AlN films

### 3.1 Introduction

Aluminum nitride (AlN) films have been attracted in the semiconductor industry due to their unique outstanding physical and optical properties with great technological advantages. Deep ultra-violet light-emitting diode (UV-LED) with high efficiency is an expected future candidate for health care and industrial applications where AlN thin films find an important role with emission wavelength of 210 nm (shortest wavelength ever observed from any semiconductor) using a *p-i-n* homojunction of AlN. The extracted light intensity along the surface normal from *a-plane* or *m-plane* deep UV-LED is 25 times higher compared to the conventional *c-plane* structure [28, 29]. So, plane orientation heavily affects the radiation properties of UV-LED, polarizer, electro-luminescent diodes like optoelectronic devices. Generally, properties of these films depend on the crystal structure, crystal orientation and micro-structure that in turn depend on the deposition conditions. Thus, it is important to optimize the growth conditions and to develop high quality *a*-axis oriented AlN films. Due to simplicity and reproducibility, reactive magnetron sputter-

ing technique is one of the common methods to grow AlN films under low temperature with desired crystal structure and orientation [13, 19, 33, 36, 108]. Growth temperature of thin films has a crucial role on the micro-structure and orientation, that affects the physical properties including optical and mechanical. It is also important to examine the nature of anisotropic optical properties of these films for its better use in the area of optoelectronics. Although there are few reports available on the anisotropic optical properties of AlN thin films, which are confined to *c-axis* oriented films only [88–92]. Therefore, it is imperative and pertinent to examine the nature of refractive index of *a-axis* oriented AlN films.

The present chapter describes the growth of poly-crystalline and *a-axis* oriented AlN thin films by DC reactive magnetron sputtering at different growth temperatures ( $T_s$ ). The crystallographic structure and surface morphology of these films are investigated by GIXRD, rocking curve, TEM and AFM techniques. The evolution of residual stress in AlN films with growth temperature is also studied by  $\sin^2\psi$  technique. The nano-indentation technique is used to investigate the mechanical properties of these films. The optical anisotropic behavior of these AlN films are carried out using SE technique in the photon energy range of 0.6 to 6.5 eV.

## 3.2 Growth and crystallographic studies of AlN films

AlN thin films are grown on silicon substrates by DC reactive magnetron sputtering technique from pure aluminum target (4N) of 50 mm diameter in a high purity argon and nitrogen gas mixture. These Si substrates are cleaned by a standard two-step RCA process. Few layer of Al in Ar atmosphere is deposited on the substrate for few seconds

to improve the adhesion between the substrate and the deposited film. Thereafter, AlN films are deposited in  $5 \times 10^{-3}$  mbar sputtering pressure at different growth temperatures ( $T_s$  : 35, 200, 400 and 600 °C) by keeping all other sputtering parameters constant. The details of the growth parameters are given at section 2.3.1.

### 3.2.1 GIXRD

The GIXRD profiles of AlN thin films deposited over Si (100) with different  $T_s$  varying from 35 to 600 °C by DC magnetron sputtering are shown in Fig. 3.1. The GIXRD patterns of these films show poly-crystalline hexagonal wurtzite structure and agree with the JCPDS data 25-1133. At 35 °C, a poly-crystalline nature is observed, however with the increase in temperature up to 400 °C, the crystallinity has increased along with orientation either (101) or (100). At 400 °C, the film exhibits a strong texture towards (100) plane *i.e.* a preferential orientation towards *a-axis*. Thereafter, the crystallinity is decreased at 600 °C and shows a profile similar to AlN film grown at 35 °C.

When x-ray beam is irradiated in asymmetrical diffraction configuration (GIXRD) with a particular angle (Bragg angle) on the planes of oriented crystals, a high intensity peak is seen corresponding to that plane and it is called texture. Generally, the texture is used when maximum number of crystals inside the film are orientated in a single direction [109]. However, epitaxial growth is used when all the crystals belonging to the film grown in a single direction perpendicular to the substrate. Hence, it is concluded that there is a preferential orientation along *a-axis* of AlN film grown at 400 °C. To verify the crystal quality and preferential orientation along *a-axis* of this AlN film, a rocking curve of (100) plane has carried out and is shown in Fig. 3.2. It exhibits a FWHM of  $0.0391 \pm 0.0005$  at the angle  $33.2^\circ$  ( $2\theta$ ). This signifies that the (100) planes are oriented parallel to the



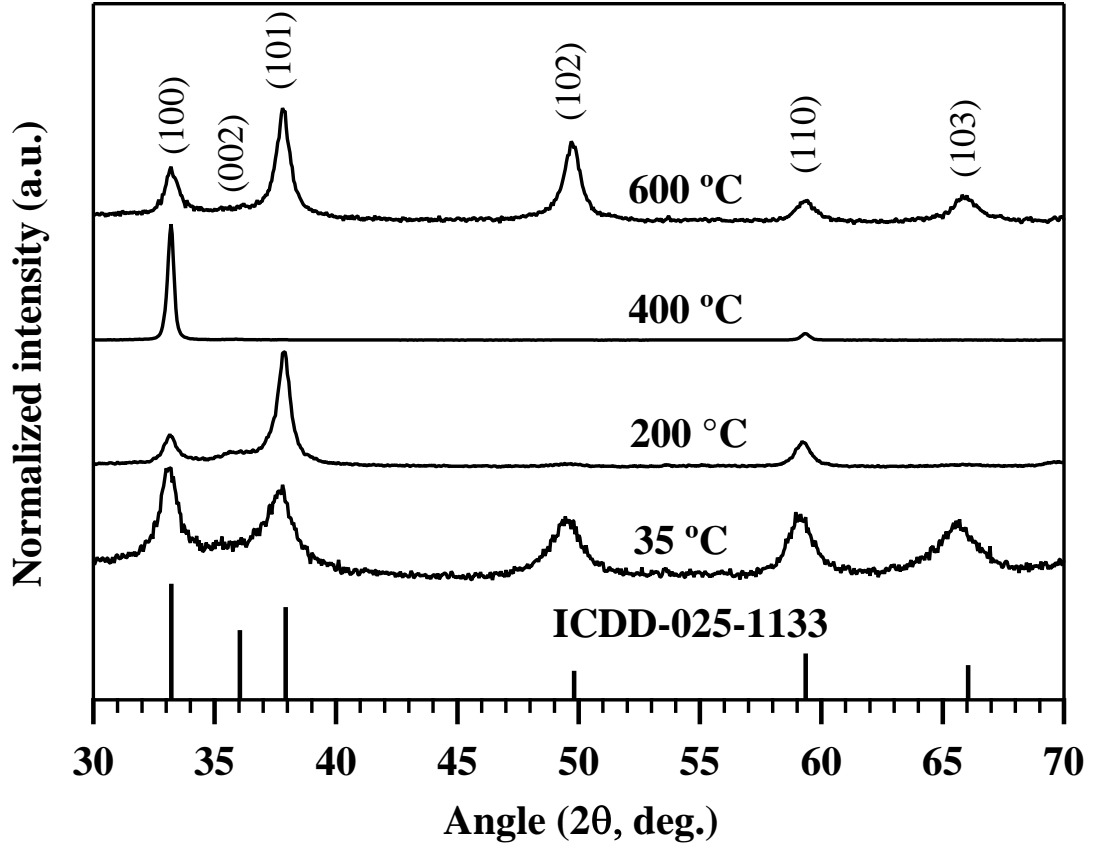


**Figure 3.1** – GIXRD profiles of AlN thin films with different  $T_s$ .

substrate. However this is slightly larger than the reported *a-axis* oriented AlN where the target to substrate distance is varied by maintaining substrate temperature constant[19].

To understand the growth of AlN thin films with temperature, it is important to know the bonding nature and strength with its orientation. The crystal structure of wurtzite AlN is discussed and shown in Fig. 1.1 of section 1.1.1. One Al atom is associated with four N atoms and forms a distorted tetrahedron structure. Among them, three Al-N<sub>(i)</sub> (*i* = 1, 2, 3) bonds are named as B<sub>1</sub>, whereas one Al - N<sub>0</sub> bond in the *c-axis* direction is named as B<sub>2</sub>. The bond B<sub>1</sub> is more covalent in nature, whereas B<sub>2</sub> is more ionic in nature [12, 13]. The (100) plane is composed of the B<sub>1</sub> bonds which is much stronger compared to B<sub>2</sub> bonds. So at low pressures and increasing temperatures, B<sub>2</sub> bond can be

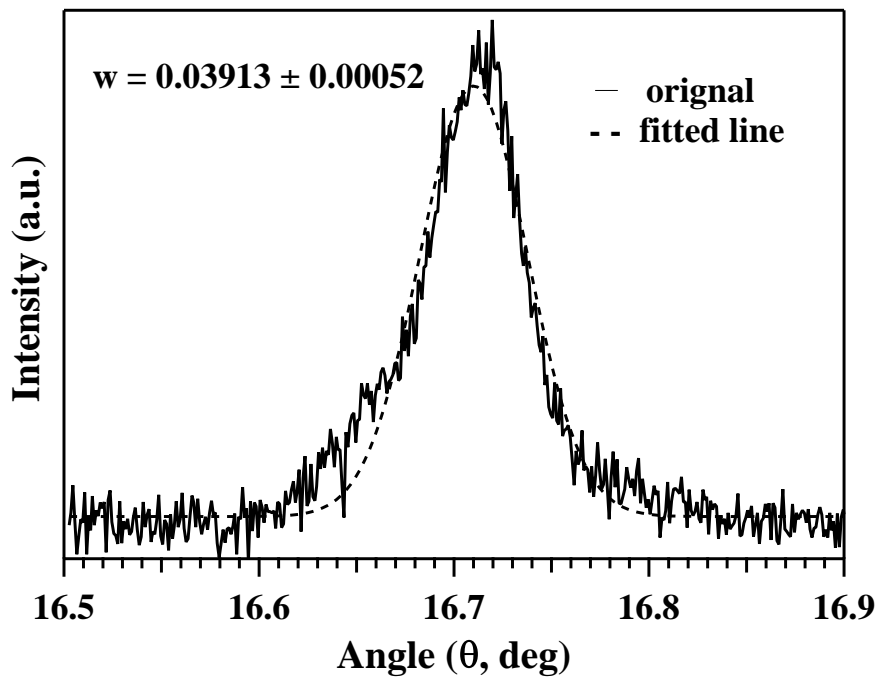


**Figure 3.2** – Rocking curve for (100) plane of AlN grown at 400 °C.

easily dissociated that led to the increase in the vertical growth rate of (100) planes. At 400 °C growth temperature, the film is highly oriented along *a*-axis due to (100) crystallite overgrowth compared to other orientations. But above 400 °C, other orientations are also present, since higher temperature is favorable for the dissociation and regrowth of both the bonds. Therefore, it can be understood that the optimum growth temperature for depositing highly *a*-axis oriented AlN films is 400 °C.

Crystallite size was calculated from GIXRD profile using Williamson-Hall method and plotted against growth temperature ( $T_s$ ) as shown in Fig. 3.3. The crystallite size increases with the increase of  $T_s$  until 400 °C and thereafter, it decreases. This is due to the enhanced atom mobility at high temperatures, this increases the ad-atoms surface diffusion length leading to a higher probability of ad-atoms migration from the landing site to nucleation site. So that a better crystallinity and higher degree of orientation is seen up to 400 °C. However, further increase in the growth temperature the crystallite

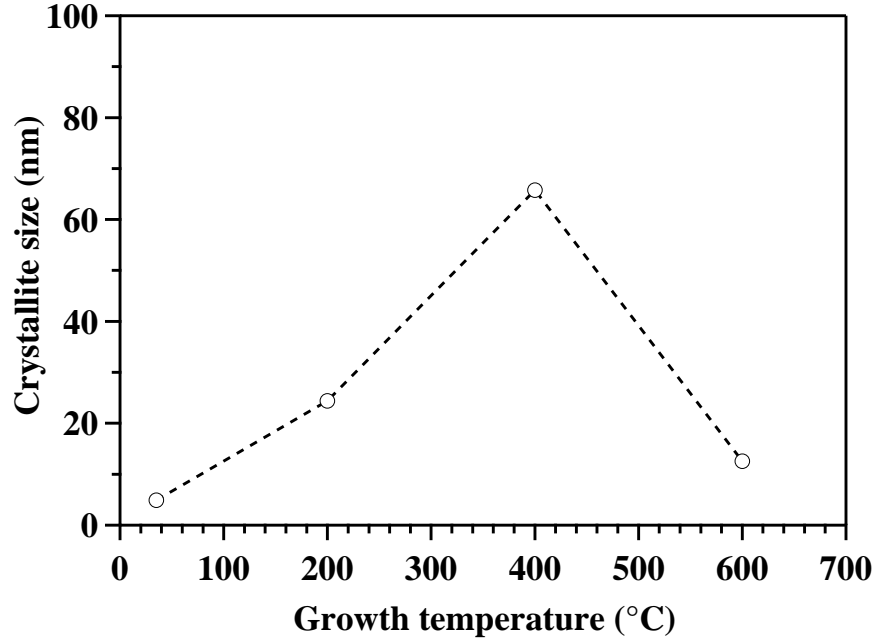


**Figure 3.3** – The variation of crystallite size of AlN thin films with different growth temperature ( $T_s$ ).

size decreases drastically. At higher temperatures over 400 °C, excessive surface mobility of ad-atoms make thin film texture difficult due to stronger re-evaporation effect which results in reducing the crystallite size and intensity of the peaks [108, 110].

### 3.2.2 Cross sectional TEM and SAED

Figs. 3.4(a-d) show dark-field TEM cross sectional micrographs of AlN films grown at different  $T_s$ . The structure comprises of parallelly spaced columnar structure with an angle tilted by a few degrees to the substrate normal. In sputtering system there are three guns placed focusing towards the substrate at an angle. So the sputtered atom flux arrives obliquely at an angle  $\alpha$  and causes inclination to the crystallite columns by  $\beta$ , where  $\alpha$  and  $\beta$  are related by the empirical tangent-rule :  $\tan \beta = 1/2 \tan \alpha$  [111]. A thin interface layer of Al deposited to improve the bonding between AlN and Si substrate is visible at the bottom of the columnar films.

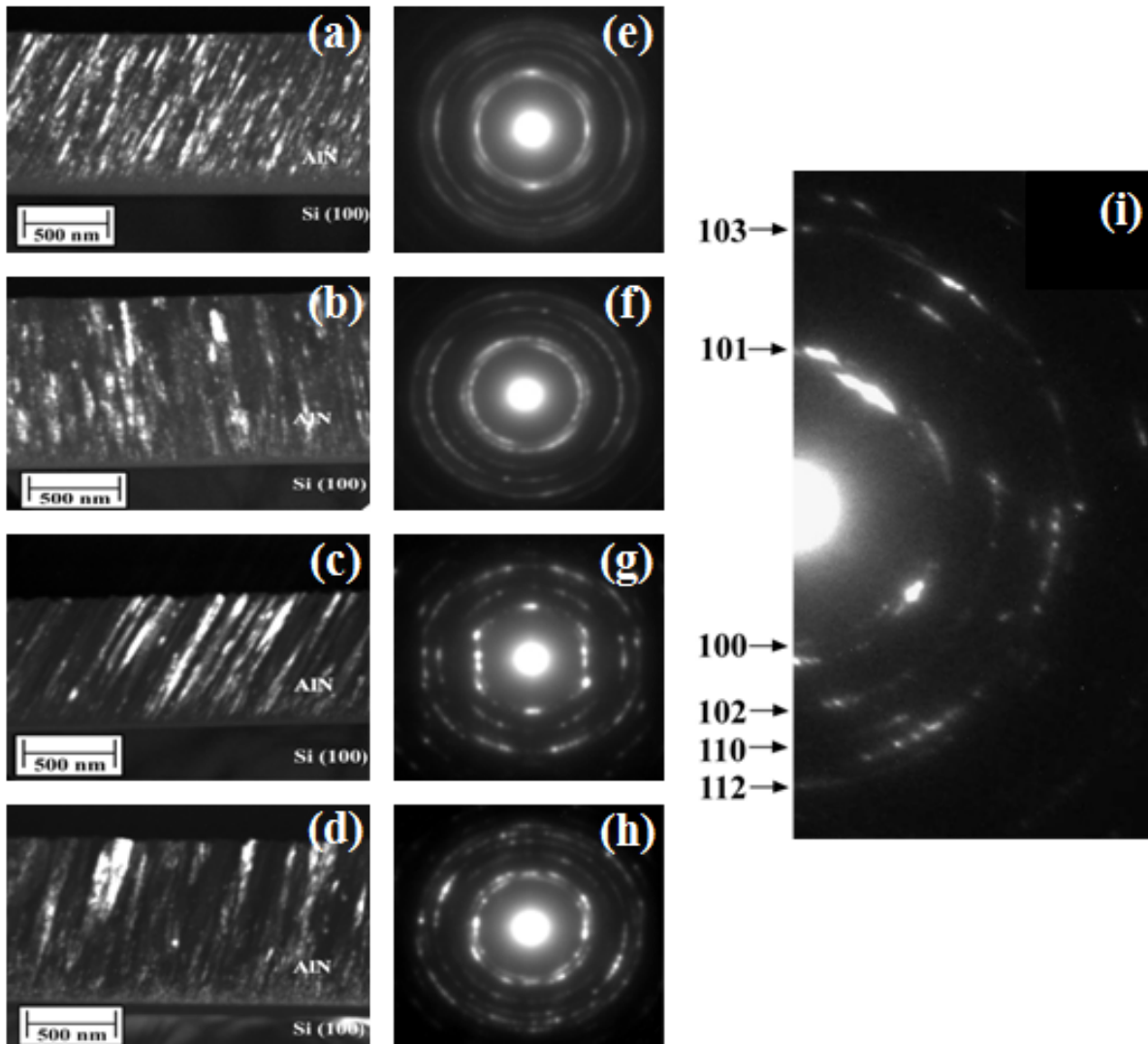


**Figure 3.4** – Dark-field cross-sectional TEM micrographs (a-d), corresponding SAED patterns (e-h) of AlN films grown at 35, 200, 400 and 600 °C, respectively and indexed SAED pattern of AlN film grown at 400 °C (i).

Figs. 3.4(e-i) shows the corresponding SAED patterns of those films deposited at different  $T_s$ . The diffraction rings are indexed using the space group  $P6_3mc$ , lattice constants  $a = 0.311$  nm and  $c = 0.497$  nm (JCPDS file 25-1133). The one deposited at 35 °C exhibited a polycrystalline micro-structure with mixed planes of (100), (101), (102), (110), (103) and (112). A representative SAED pattern of AlN film grown at 400 °C is indexed and is shown in Fig. 3.4(i). Generally, SAED patterns of single crystal, polycrystalline and amorphous material exhibit spot, sharp ring and diffused like ring patterns, respectively

[97]. Since, all these films are polycrystalline in nature, the SAED shows a perfect circular ring patterns. However, the one deposited at 400 °C exhibits a systematic dot pattern of (100) plane. This pattern represents a well crystallized film with a preferential orientation towards *a-axis* compared to other films and analogous to the GIXRD profile shown in Fig. 3.1.

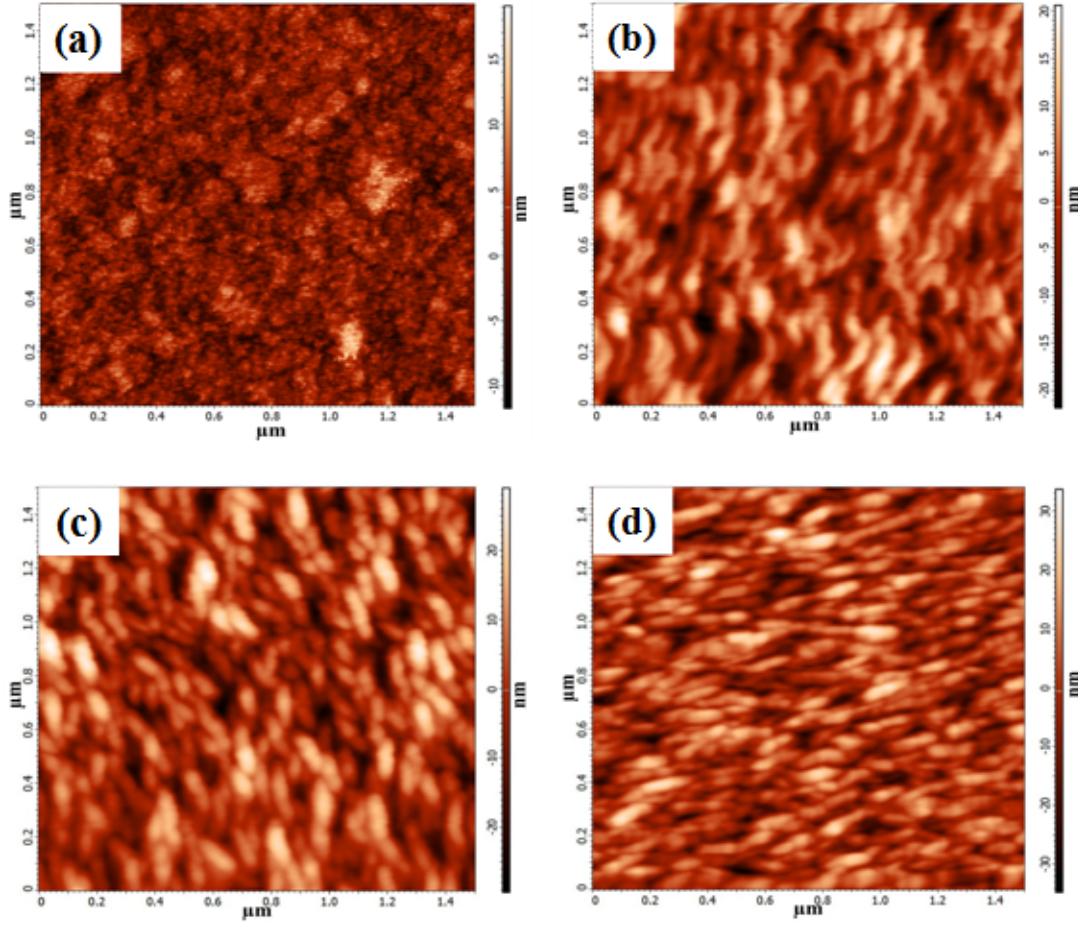
### 3.2.3 Morphology and surface roughness by AFM

Fig. 3.5 consists of AFM images taken over  $1.5 \times 1.5 \mu m^2$  area showing the morphology of AlN films deposited on Si at various  $T_s$ . In Fig. 3.5 (a), AlN films deposited at 35 °C exhibit irregular grains with less surface density. However, the increase in growth temperature from 200 °C to 600 °C resulted a similar morphology with a pebble-like grain structure and dense surface.

$T_s$ (°C)	$R_{rms}$ (nm)	Grain size (nm)
35	3.0	10.5
200	5.2	48.0
400	9.0	64.0
600	7.8	37.0

**Table 3.1** – RMS roughness ( $R_{rms}$ ) and average grain size of these AlN films.

Table 3.1, displays the root mean square roughness ( $R_{rms}$ ) and the mean diameter of the grains against the growth temperatures ( $T_s$ ).  $R_{rms}$  and average grain size are significantly affected by the increase in growth temperatures. Since the thermal energy is delivered to the surface, the energy and mobility of surface ad-atoms are enhanced the atomic diffusion. This resulted in the formation of fewer large grains by agglomeration of adjoining atoms or crystals and make surface coarser with the growth temperatures. This can be seen in the cross-sectional TEM image (Fig. 3.4), the waviness is pronounced more in 400 °C. However, at 600 °C roughness decreases due to the decrease in grain size and crystallite size which is similar to Fig. 3.3.



**Figure 3.5** – AFM images of AlN films on Si grown at (a) 35 °C, (b) 200 °C, (c) 400 °C and (d) 600 °C.

### 3.3 Residual stress

Residual stress plays an important role on thin films since it alters the physical properties like energy-band structure, external quantum efficiency of LED, piezoelectric constant and mechanical properties. This may cause micro-cracks or peeling from the substrate, which reduces the coated component lifetime and performance [112]. Therefore, it is important to control the residual stress by controlling the deposition parameters to synthesize a mechanically stable films. A well-documented  $\sin^2\psi$  technique has been used to measure the residual stress of these AlN films, which is discussed in section 2.4.1. The observed

residual stress of all these films are shown in Fig. 3.6 as a function of  $T_s$ . A tendency from tensile to compression is observed with the increase in  $T_s$ . The mean value of the residual stress has decreased from 0.42 GPa to 0.28 GPa, when the  $T_s$  increased from 35 °C to 200 °C. However, after this temperature a transition has occurred in the residual stress *i.e* tensile to compressive mode. At 600 °C, the residual stress has increased in the compression mode up to 0.15 GPa.

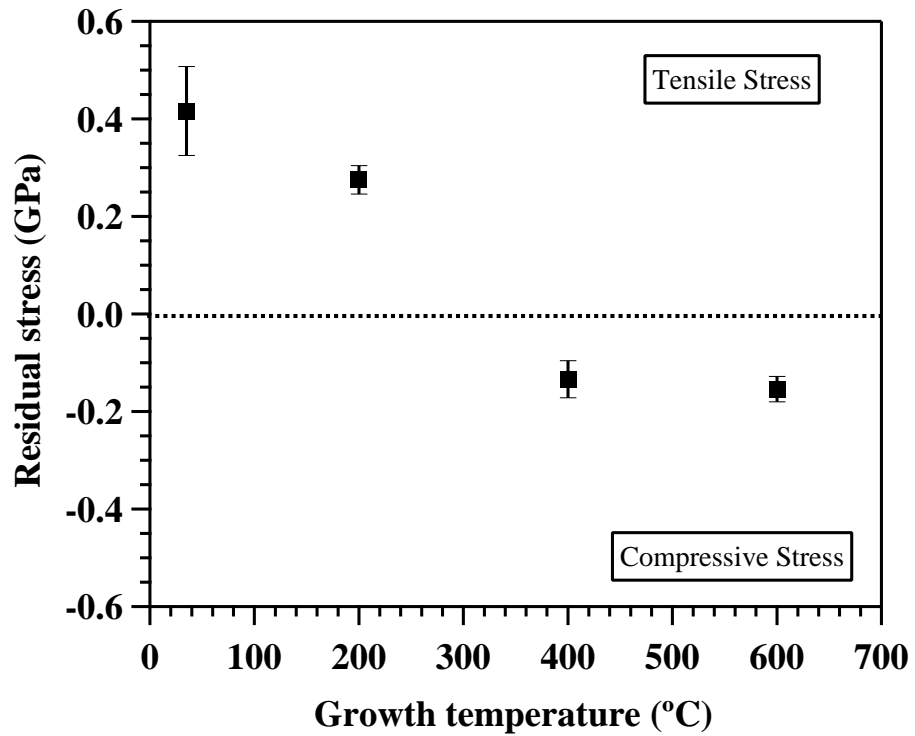


**Figure 3.6** – Residual stress of AlN thin films as a function of  $T_s$ .

To understand the nature of residual stress with the  $T_s$ , the literature results are summarized in Table 3.2. Especially, only the transition from tensile to compressive stress regions and vice versa are picked up for the discussion. Among all, only Wang *et al.* reported a similar transition (the bias voltage was kept at -40 V), whereas in this study the bias voltage was 0 V [113].

RT to high temperature residual stress variation	Range of shift ( $T_s$ )	Deposition technique	Ref.
Tensile to compressive	150 to 300 °C	DC reactive sputtering	[113]
Compressive to tensile	RT to 400 °C	RF reactive sputtering	[13]
Tensile to compressive	200 to 400 °C	DC reactive sputtering	this work

**Table 3.2** – Residual stress of AlN films at different  $T_s$ .

At low  $T_s/T_m$  ( $T_s$  = growth temperature and  $T_m$  = melting temperature of coating material), the intrinsic stress dominate over the thermal stress. It is important to know whether the thermal stress also plays a role in the residual stress of the system. In general, the origin of residual stress can be attributed to the epitaxial stress (lattice mismatch between substrate and the film), thermal stress (difference in co-efficient of thermal expansion between substrate and the film), microstructure and the mode of growth (intrinsic stress). The thermal expansion coefficient of AlN film is larger than that of the Si substrate. Due to this, AlN films possess a thermal stress as the film is cooled down to room temperature from high temperature after deposition. This thermal stress can be calculated using the relation[114]

$$\sigma_T = \frac{E_f}{(1 - \nu_f)}(\alpha_s - \alpha_f)(T_s - T_r) \quad (3.1)$$

where  $\sigma_T$  is thermal stress,  $\alpha_s$  and  $\alpha_f$  are thermal coefficient of expansion of substrate (Si,  $3.6 \times 10^{-6} \text{ }^\circ\text{C}^{-1}$ ) and the AlN film ( $5.3, 4.2 \times 10^{-6} \text{ }^\circ\text{C}^{-1}$  along *a-axis* and *c-axis*, respectively)  $T_r$  and  $T_s$  are room and growth temperature,  $E_f$  and  $\nu_f$  are Young's modulus (AlN, 350 GPa) and Poisson's ratio (AlN, 0.21) [115]. The calculated thermal stress is shown in Table 3.3. It is seen that AlN exhibits a strong compressive thermal stress along *a-axis* compared to *c-axis* with increase in  $T_s$ .

Intrinsic or growth stress is a structure and micro-structure sensitive property which is



$T_s(^{\circ}\text{C})$	$\sigma_T(a\text{-axis})$ (GPa)	$\sigma_T(c\text{-axis})$ (GPa)
35	-0.007	-0.002
200	-0.131	-0.046
400	-0.282	-0.099
600	-0.433	-0.152

**Table 3.3** – Thermal stress of *a-axis* and *c-axis* AlN films at different  $T_s$ .

observed in films during deposition and growth under non-equilibrium conditions. In the early stages of the film growth, the film consists of smaller crystallites/grains, separated by an atomic-scale distance. When these crystallites/grains coalesce, a tensile stress is generated at the point where neighboring islands impinge on each other [116]. As well as, the parameter  $T_s/T_m$  is very important in stress-related behavior for different materials. At low growth temperature *i.e* low  $T_s/T_m$ , the intrinsic stress can dominate over thermal stress [117, 118]. Because, when these AlN films deposited at room temperature, there is a little surface diffusion and one would expect the Al or N vacancy concentration to be much larger than at equilibrium. When these excess vacancies are subsequently annihilated at vertical boundary, the associated volume change results in an in-plane change of film dimensions [119]. So at lower growth temperatures, stress relaxation by diffusion does not occur where intrinsic stress dominates over the thermal stress and a tensile stress develops. Also, according to atomic peening model, at high deposition pressure and high TSD (14 cm), the mean free path of the sputtered particle reduces, and there is a particle energy loss due to increase in collision probability between plasma particles which increases the oblique angle particle bombardment. So, atomic self-shadowing effect causes a tensile stress in the film[117, 118].

However, the increase in  $T_s$ , the diffusion of defects and vacancies in AlN lattice microstructure causes the decrease in residual stress due to film densification by decreasing

the void regions through enhanced atomic rearrangement. At 400 °C, the film shows preferential orientation along *a-axis* that possess high thermal stress compared to *c-axis*. So the residual stress changes from tensile to compressive stress due to dominant of thermal stress over intrinsic stress. There after, thermal stress dominates over the intrinsic stress at high  $T_s$  (600 °C) and the compressive residual stress increases. It can be reasoned in Fig. 3.6 that  $T_s$  plays a major role on residual stress of sputtered AlN films.

### 3.4 Mechanical properties

The indentation test have been performed to the know the penetration resistance of materials *i.e* mechanical properties of materials by a known geometry indenter under a fixed load. Recently, It has been seen that there is a significant improvement in indentation equipment for the measurement of mechanical properties on small scales (few nm) of materials. It is now feasible to monitor a very precise and accurate load and depth of an indenter during experiment.

Thin film of AlN is a potential wide band gap semiconducting material for optoelectronic device applications. Moreover, the physical contact loading during processing or packaging of devices, generates plastic deformation which significantly deteriorates the performance of the devices. In this regard, it is vital to study of mechanical properties of AlN films with different growth temperatures. Nanoindentation studies are performed on these films at a peak load of 4 mN. The absence of creep and thermal drift was verified by holding the indenter at maximum load for 2 sec (no change in penetration depth). The indentation hardness ( $H$ ) and modulus ( $E$ ) are extracted from the loading and unloading of the indentation curve as described in section 2.6, are shown in Fig. 3.7. At 35 °C, AlN film shows a hardness increases to 18.5 GPa for AlN film grown at 200 °C. There after,

further increase in  $T_s$ , hardness shows a gradual drop *i.e.* down to 13.0 GPa for 600 °C.

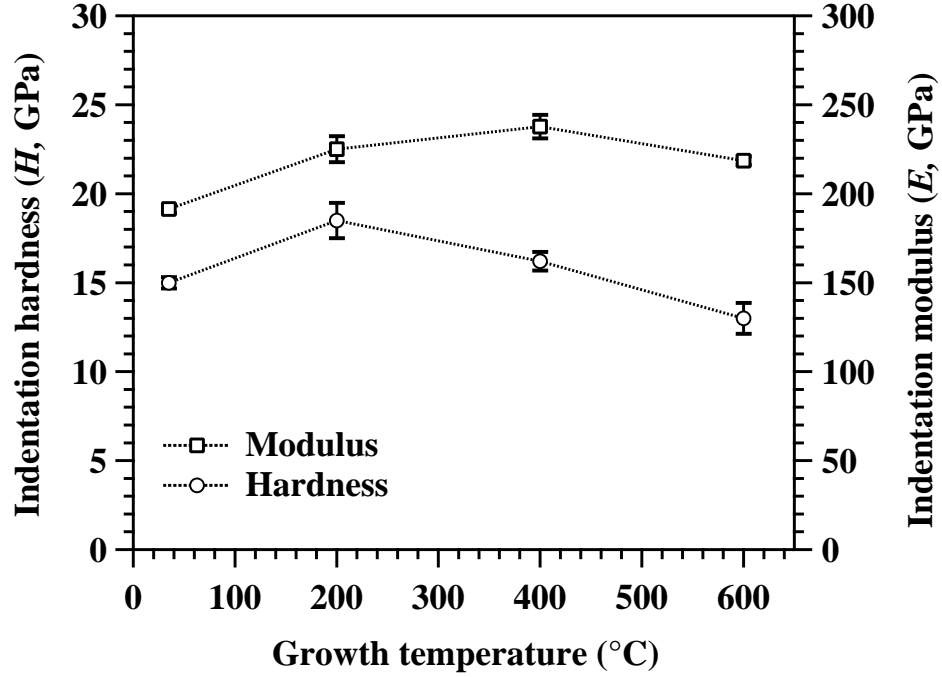


**Figure 3.7** – Hardness and modulus of AlN thin films as a function of  $T_s$ .

Normally, crystallite size of material, plane orientation, planar density, bond strength and residual stress collectively contributes to the change in mechanical properties of the thin film. In this study, AlN film grown at 35 °C shows a  $H$  as 15.0 GPa due to the presence of defect and porosity at low growth temperature, however AlN film grown at 200 °C shows high  $H$  value compared to other films. It can be seen from GIXRD profile of AlN films in Fig. 3.1 that AlN grown at 200 °C exhibits a strong texture along (101) planes, which belongs to *c-plane* family having higher planar density. Therefore, it shows a relatively high hardness compared to other films. It is understood from GIXRD and AFM, the average crystallite size and grain size increases with  $T_s$ . Additionally, the stress relaxation occurred in these films can be seen from residual stress measurement in Fig. 3.6. According to Hall-Petch relation, the hardness decreases with increase in crystallite size. Hence, the  $H$  is decreased with growth temperatures. Also, a transition

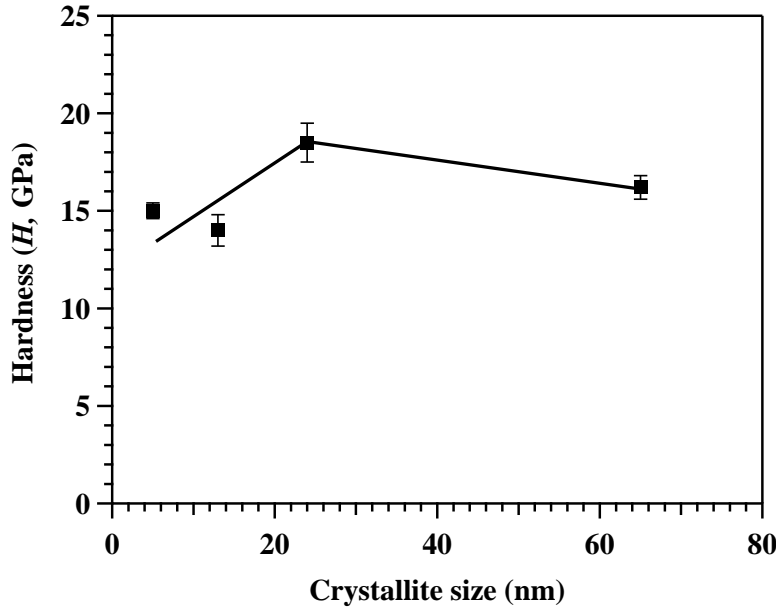


**Figure 3.8** – Behavior of hardness as a function of crystallite size.

from Hall-Petch to inverse Hall-Petch occurs when crystallite size is around 15-18 nm [120, 121]. Fig. 3.8 shows the behavior of hardness as a function of crystallite size. In this study, it also shows a critical transition of crystallite size around 15-20 nm *i.e.* lower the critical size, the hardness decreased and above the critical size the hardness also decreased with increase in crystallite size, which is satisfying the Hall-Petch relation. Moreover, indentation modulus ( $E$ ) of these AlN films is also varied from 192 to 238 GPa with different  $T_s$ . Generally, modulus depends on the nature of the inter-atomic bonds in the crystal. At 400 °C, AlN film is highly *a-axis* oriented which contains  $B_1$  type of bonds (covalent). So this film has exhibited high elastic nature with higher modulus of 238 GPa.

### 3.5 Anisotropic optical properties of AlN films

SE is used to measure anisotropic optical properties of AlN films as a function of  $T_s$  to investigate the refractive index ( $n$ ), extinction co-efficient ( $k$ ) and band gap. The SE parameters are measured in ambient conditions by a phase modulated ellipsometer at

different incident angle of  $65^\circ$ ,  $70^\circ$  and  $75^\circ$  in the photon energy range of 0.6 to 6.5 eV with 0.01 eV increment. In this experiment,  $I_s$  and  $I_c$  are the experimentally measured parameters using the fundamental parameters ( $\Psi$  and  $\Delta$ ) from which the pseudo dielectric constants are computed as described in section 2.7.

### 3.5.1 Modeling and fitting for the analysis of optical constant

In this study, AlN film grown at  $400^\circ\text{C}$  shows a strong texture along (100) plane with hexagonal wurtzite structure, which is shown in Fig. 3.1. A rocking curve of (100) exhibits FWHM of  $0.0391 \pm 0.0005$  at an angle of  $33.2^\circ$ , which confirms that the film is preferentially oriented along [100] direction to the normal of the surface. From the rocking curve, it is inferred that the optic axis (*c-axis*) in the present experiment is in the plane of the film. In literature, it is reported that the single crystal AlN and epitaxial AlN along *c-axis* (optic axis) exhibit uniaxial anisotropic properties [88–92].

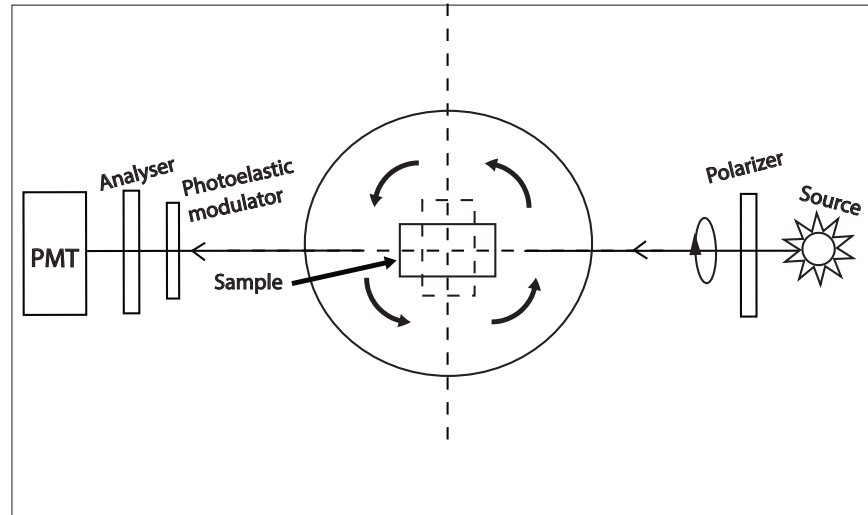


**Figure 3.9** – A schematic diagram of the ellipsometry experiment with the different azimuthal angles.

Owing to the columnar structure in these films (Fig. 3.4), SE measurement has performed at different azimuthal angles ( $0^\circ$ ,  $90^\circ$ ,  $180^\circ$  and  $270^\circ$ ) for AlN film grown at  $400^\circ\text{C}$  for angle of incidence of  $70^\circ$ . The schematic diagram of measurement methodology is shown

in Fig. 3.9. The extracted  $n$  and  $k$  values with azimuthal angles are shown in Fig. 3.10, which show a difference near to band edge of this film.

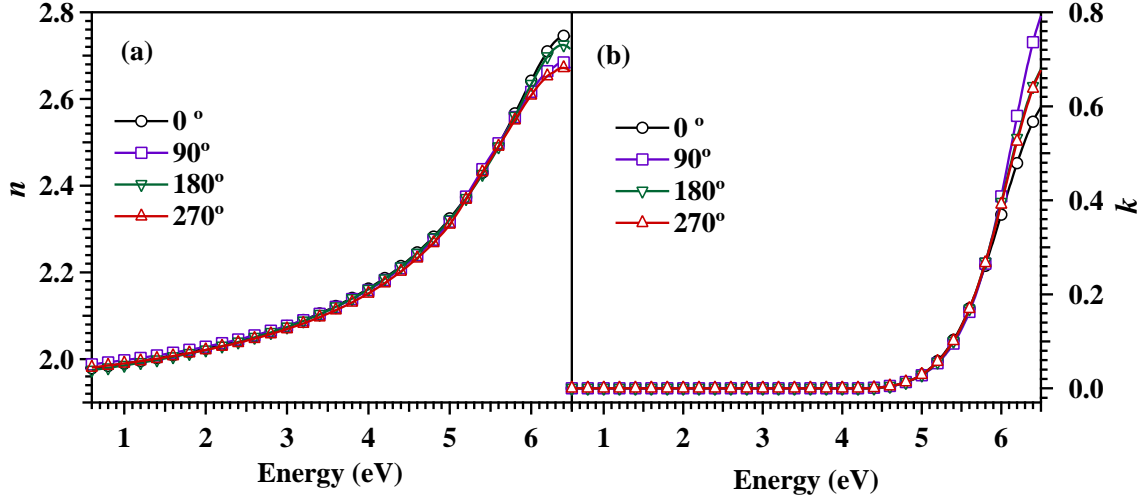


**Figure 3.10** – The extracted (a)  $n$  and (b)  $k$  at a different azimuthal angles for AlN film grown at 400 °C.

In this study, the SE data of these films are collected for three different angles of incidence, viz 65°, 70° and 75°. A representative experimentally measured ellipsometric parameters ( $I_s$  and  $I_c$ ) for 65°, 70° and 75° angles of incidence for the film grown at 35 and 400 °C are shown in Fig. 3.11 and 3.12, respectively. The corresponding pseudo dielectric functions ( $\epsilon_r$  and  $\epsilon_i$ ) are also shown in Fig. 3.13 and 3.14, respectively. It is found that the pseudo-dielectric function deduced from  $I_s$  and  $I_c$  for the three angles showed a difference for 400 °C film as compared to the 35 °C film. The small difference for 400 °C film could be due to the orientation of the film along  $a$ -axis *i.e.* it exhibits an anisotropic behavior.

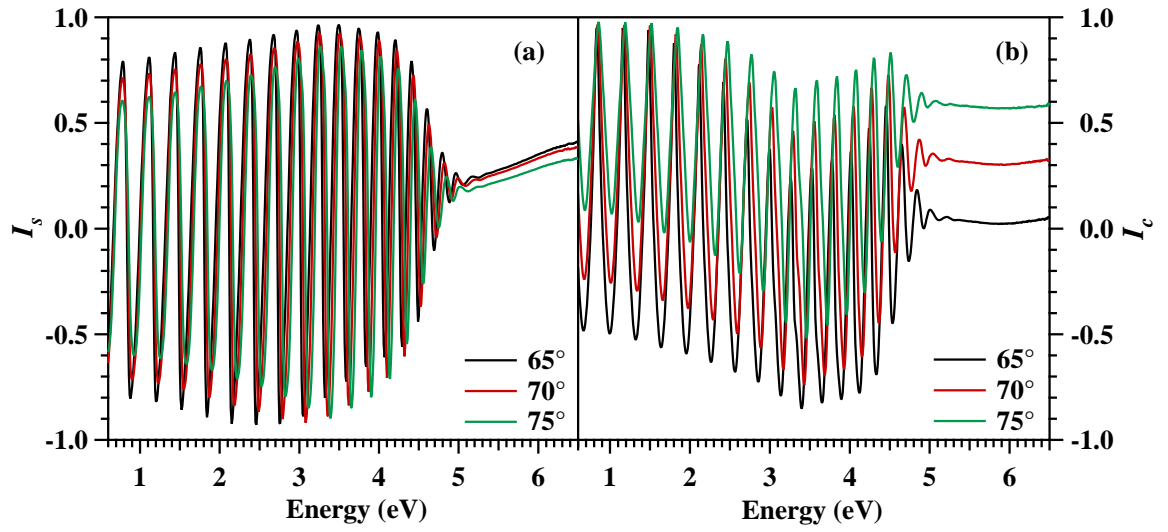


**Figure 3.11** – The measured (a)  $I_s$  and (b)  $I_c$  at a different incident angle for AlN film grown at 35 °C.

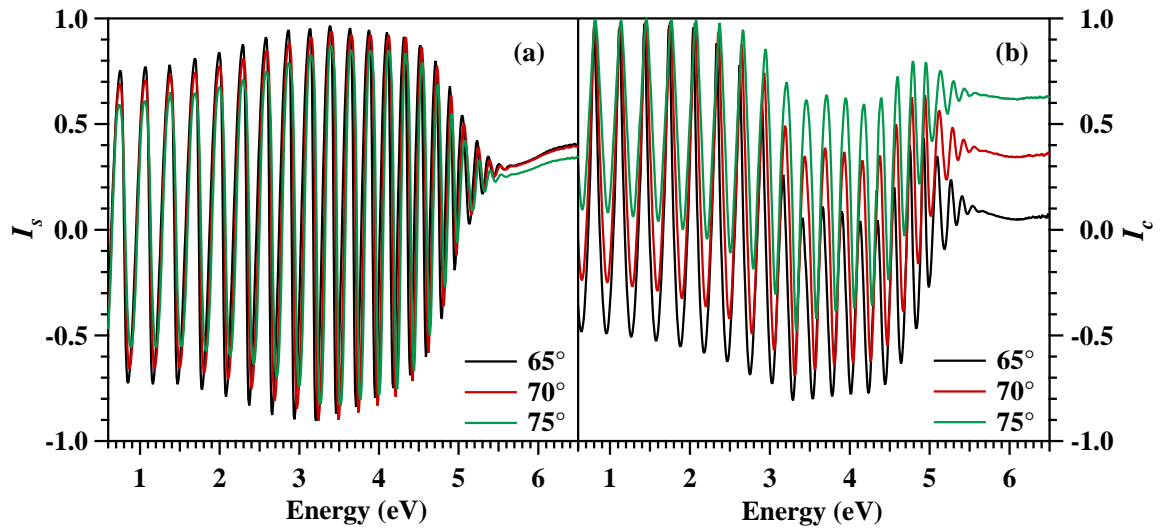


**Figure 3.12** – The measured (a)  $I_s$  and (b)  $I_c$  at a different incident angle for AlN film grown at 400 °C.

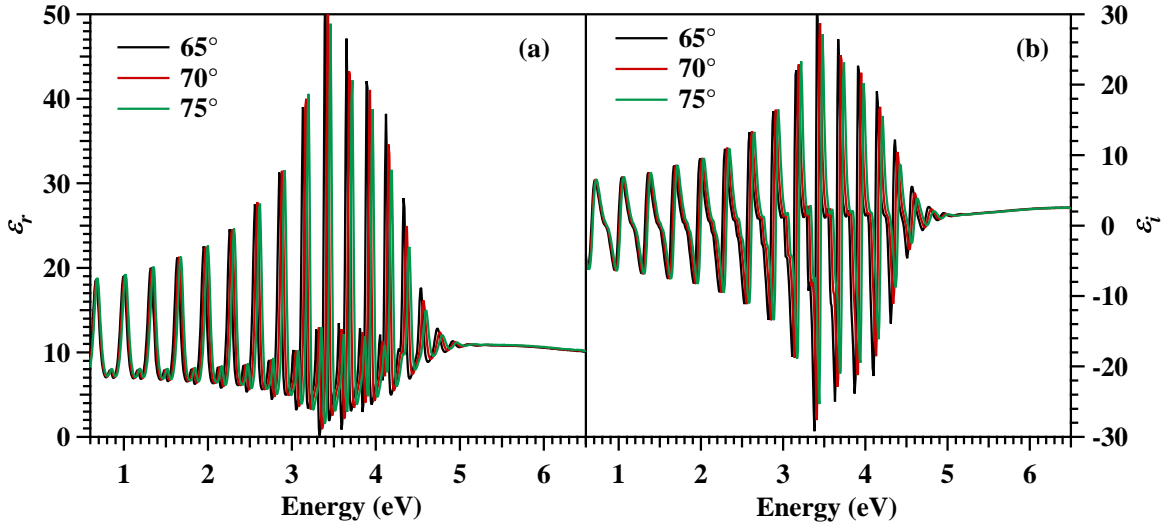


**Figure 3.13** – The measured (a)  $\epsilon_r$  and (b)  $\epsilon_i$  at a different incident angle for AlN film grown at 35 °C.

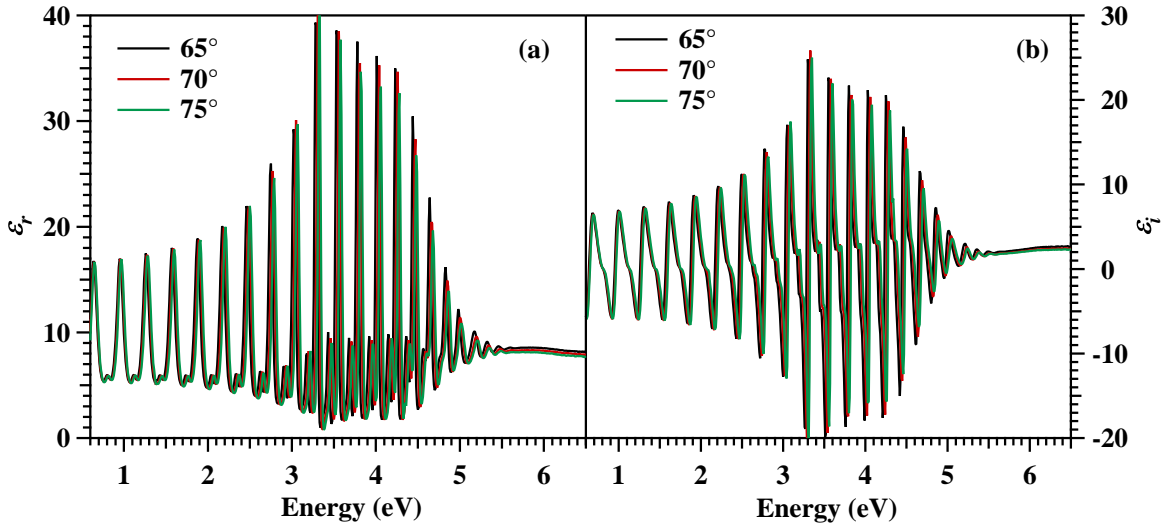


**Figure 3.14** – The measured (a)  $\epsilon_r$  and (b)  $\epsilon_i$  at a different incident angle for AlN film grown at 400 °C.

The refractive index ( $n$ ) and extinction coefficient ( $k$ ) of these films are computed by fitting  $I_s$  and  $I_c$  with the modified Forouhi-Bloomer dispersion relation. This relation fits smoothly for broader wavelength range *i.e.* from normal to anomalous dispersion region [122]. This is also consistent with Kramers-Kronig relation with five independent parameters as described below.



$$n = n_\infty + \sum_{j=1}^N \frac{B_j(\omega - \omega_j) + C_j}{(\omega - \omega_j)^2 + \Gamma_j^2} \quad (3.2)$$

$$k = \begin{cases} \sum_{j=1}^N \frac{f_j(\omega - \omega_g)^2}{(\omega - \omega_j)^2 + \Gamma_j^2} & : \omega > \omega_g \\ 0 & : \omega \leq \omega_g \end{cases} \quad (3.3)$$

where

$$\begin{cases} B_j = \frac{f_j}{\Gamma_j} [\Gamma_j^2 - (\omega_j - \omega_g)^2] \\ C_j = 2f_j\Gamma_j(\omega_j - \omega_g) \end{cases}$$

where, the term  $f_j$  (in eV) is the oscillator strength,  $\Gamma_j$  (in eV) is the broadening factor of absorption peak,  $\omega_j$  (in eV) is the energy at which the extinction coefficient is maximum and  $\omega_g$  (in eV) is the minimum energy from which absorption starts.

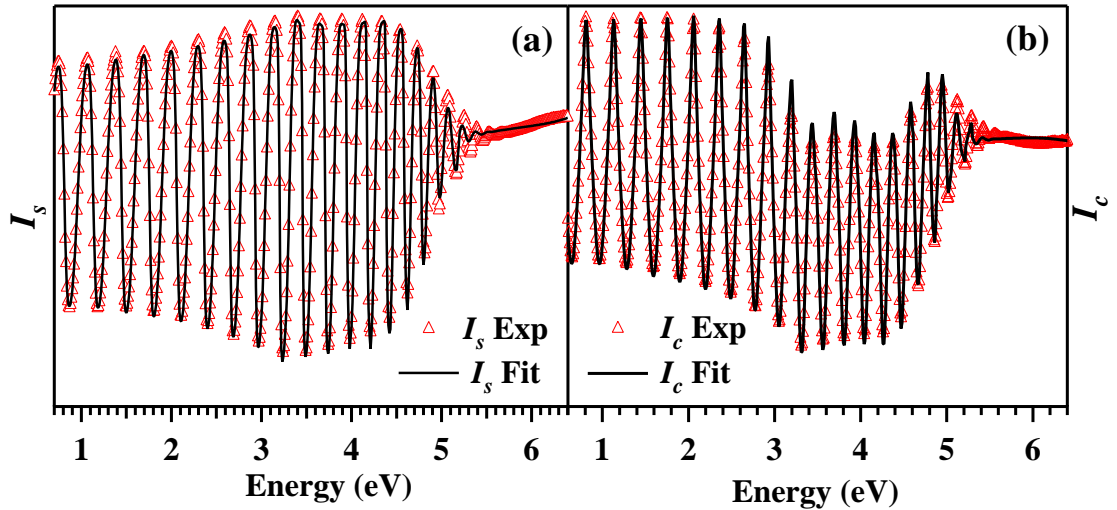


**Figure 3.15** – Experimental and corresponding fit of (a)  $I_s$ , (b)  $I_c$  for AlN film grown at 400 °C.

The anisotropic optical properties of single crystals or epitaxial thin films are conven-

tionally studied by generalized ellipsometry [123, 124]. However, in the present case, the AlN thin films are predominantly polycrystalline and the film grown at 400 °C is textured and highly oriented along *a-axis*. The anisotropic optical properties are extracted by suitable models using DeltaPsi2 software based on the approaches mentioned in literature [90–92, 125, 126]. A systematic approach of inclusion and omission of layers has been followed in which, a five layer model (Air/roughness (AlN + void)/ AlN/ interface (Al+AlN)/ Si) with uniaxial anisotropic conditions is employed for the analysis of optical properties of AlN films. The treatment of roughness and interface layer is based on Bruggeman Effective Medium Approximation (BEMA). The fitting is performed by classical non-linear minimization Levenberg-Marquardt algorithm, which is expressed in terms of  $\chi^2$  value that defines the goodness of fit and is described in section 2.7. The  $\chi^2$  value for all the fittings are 20 to 30 in the energy range of 0.6 to 6.5 eV. Measured experimental parameters ( $I_s$  and  $I_c$ ) for AlN film grown at a typical  $T_s$  of 400 °C over a spectral range 0.6 to 6.5 eV and corresponding fit are shown in Fig. 3.15 (a,b). It is seen that the fitting of  $I_s$  and  $I_c$  across the whole spectral range is in good agreement with the experimental  $I_s$  and  $I_c$ .

The roughness as deduced from SE of these films is found to lie between 7 and 20 nm. These values are higher than the root mean square roughness values (3 to 9 nm) as obtained from atomic force microscopy (AFM). The surface roughness obtained by AFM technique is acquired over an area of  $1.5 \times 1.5 \mu m^2$  and thus basically represents the local roughness values of these films. In SE technique, the data are acquired over a large elliptical area of  $2 \times 0.7 mm^2$ . Thus, the difference in the magnitude of roughness is due to the fact that the data for ellipsometry is obtained from a larger area with mixture of materials and voids compared to AFM [127–129]. Nevertheless, the roughness computed from SE and AFM, both follows a similar trend with  $T_s$ . The thickness of the interface

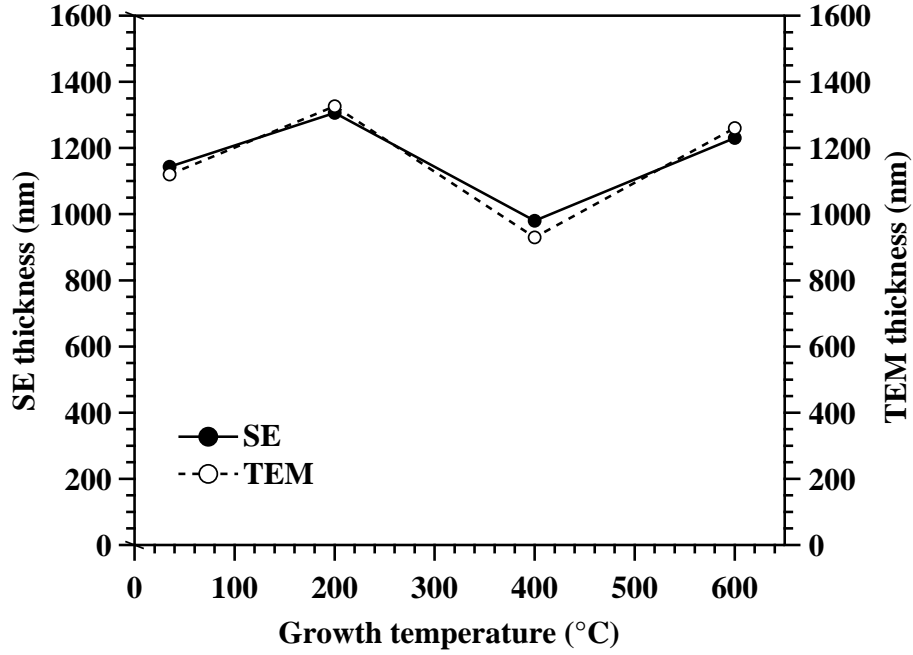


Figure 3.16 – Film thickness measured by SE and TEM.

layer (Al+AlN) between AlN film and Si substrate is extracted from the fitting that decreases from 16 to 5 nm as a function of  $T_s$ .

### 3.5.2 Behavior of anisotropic optical constant with growth temperatures

The real ( $n$ ) and imaginary ( $k$ ) parts of the refractive index of AlN films for different  $T_s$  obtained from the five layer model are shown in Fig. 3.17 (a, b, c, d). The  $n$  and  $k$  exhibit strong uniaxial anisotropic dispersion and increase monotonically with increasing photon energy in normal dispersion region, while it decreases in anomalous region. All these films show transparent nature up to a photon energy 3.5 eV (354 nm) from NIR.

Since, AlN is predominantly used in deep-UV region (210 nm), it is worthwhile to explore the behavior of both  $n$  and  $k$  of these films as a function of  $T_s$  in Fig. 3.18. With the increase in  $T_s$ , both  $n_{\perp}$  and  $n_{\parallel}$  increase up to 400 °C and then thereafter it falls, while

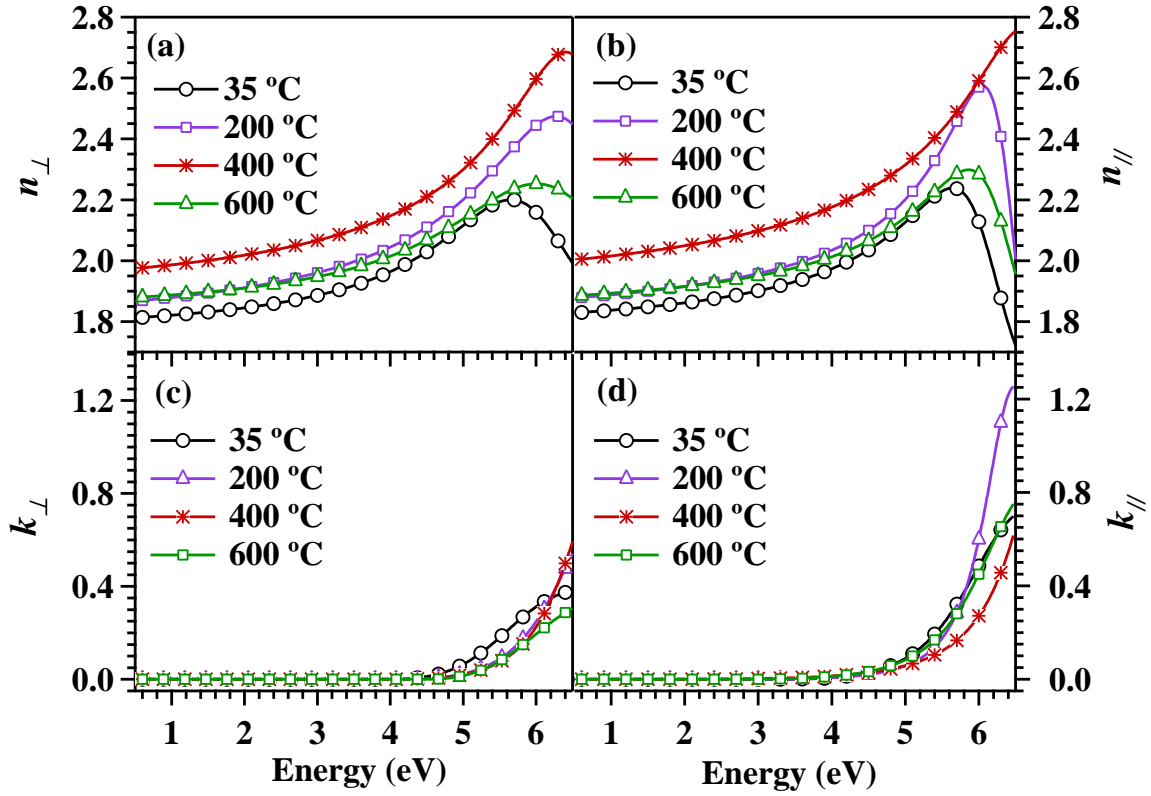


**Figure 3.17** – A plot of refractive index (a)  $n_{\perp}$ , (b)  $n_{\parallel}$  and extinction coefficient (c)  $k_{\perp}$ , (d)  $k_{\parallel}$  against to photon energy.

both  $k_{\perp}$  and  $k_{\parallel}$  decreased with respect to  $T_s$ . As it is well known that the optical parameter  $n$  and  $k$  are basically dependent on the crystal structure, disorders like voids, lattice defects and chemical composition of the film [130]. In the present study, the crystallite size of these films is shown in Fig. 3.3 and it follows the behavior of refractive index. The parameter  $T_s/T_m$  ( $T_m$  = melting temperature of growing material) is important for the columnar high dense growth of film that defines the film orientation and structure [131]. Since, the  $T_m$  of AlN is very high, the parameter  $T_s/T_m$  is very low at room temperature. Thus, there is a little surface diffusion of adatoms to grow high dense columnar structure and one would expect voids, nitrogen vacancies and defect concentration to be much higher. But, with increase in  $T_s$ , the adatom mobility increases and causes the increase in crystallite size and columnar structure. The higher mobility of adatoms causes the forma-

tion of dense AlN films and reduces the residual stress, porosity and defects. Increase in growth or annealing temperature reduces the concentration of defect states like nitrogen, impurity and coordination defects, where refractive index of the film is improved and is proportional to packing density [130, 132]. Hence,  $n$  value is increasing linearly with  $T_s$  upto 400 °C, then a fall at 600 °C due to decrease in crystallite size. So, highly *a-axis* oriented AlN film grown at 400 °C, exhibits high  $n$  ( $n_{\perp} = 2.56$ ,  $n_{\parallel} = 2.55$ ), which is lower than the reported *c-axis* oriented AlN ( $\sim 2.7$ ) [91, 92, 133]. Jiang *et al* and Shokhovets *et al* have described the optical anisotropic properties of *c-axis* oriented AlN films using the variable angle spectroscopic ellipsometry (VASE) technique [91, 92]. The refractive index values are around 2.30 ( $n_{\parallel}$ ) and 2.20 ( $n_{\perp}$ ) at 4 eV of photon energy. In the present study, the refractive index values are 2.17 ( $n_{\parallel}$ ) and 2.14 ( $n_{\perp}$ ) at 4 eV for the *a-axis* oriented AlN films [134]. At 35 °C, the value  $k$  is higher due to more vacancies in the film and Al concentration in the interface layer, that additionally contribute to the absorption by creating localized states. But, with increase in  $T_s$ , ad-atoms have high surface mobility that reduces the defects and Al concentration in the interface layer. That resulted in the reduction of  $k$  value. Thus, the optical parameters  $n$  and  $k$  strongly depend on  $T_s$  and correlates to crystallite size of these films.

To obtain the optical bandgap of these AlN films, the absorption coefficient ( $\alpha$ ) (defined as  $\alpha = 4\pi k/\lambda$ , where  $\lambda$  is the wavelength of the incident light) is calculated over extended energy range (0.6 to 6.5 eV) using the formalism followed by Looper *et al* [122]. The optical band gaps for the  $k_{\perp}$  and  $k_{\parallel}$  are obtained using a linear extrapolation of tangential line to the energy axis of  $(E\alpha)^2$ , which is shown in Fig. 3.19. These results agree well with Kar *et al*, where they have reported the bandgap energy of AlN films annealed as a function of temperature [135]. The band gap increases with  $T_s$  up to 400 °C then it decreases at 600 °C. So, optical band gap also strongly depends on the crystallite size.

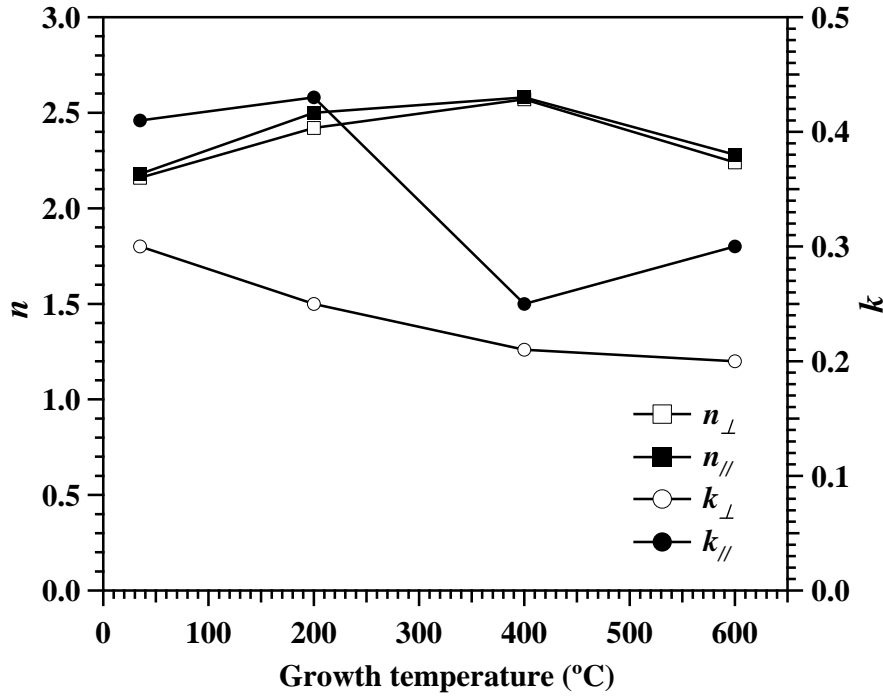


**Figure 3.18** – The variation of  $n$  and  $k$  value at 210 nm of AlN films with  $T_s$ .

At low temperatures, the band gap is small compared to bulk AlN that is due to the generation of shallow states caused by the formation of lattice distortion by voids, Al and N vacancy concentrations [130, 135]. Whereas, highly *a-axis* oriented AlN film grown at 400 °C with large crystallite size ( $\sim 66$  nm) shows direct band gap as 6.05 ( $k_{\parallel}$ ) and 6.1 eV ( $k_{\perp}$ ), which is near to the bulk AlN.

To understand the behavior of anisotropy, the difference in  $n$  (birefringence,  $\Delta n = n_{\parallel} - n_{\perp}$ ) and  $k$  (dichroism,  $\Delta k = k_{\parallel} - k_{\perp}$ ) is shown in Fig. 3.20. The  $\Delta n$  exhibits a positive value except at higher energy region. Additionally, the value of  $\Delta n$  is larger near band energy region for all these films, whereas AlN film grown at 400 °C shows a maximum birefringence at lower energy range and a minimum birefringence at near band gap. Also, all these films exhibit a strong dichroism near the band edge, whereas 400 °C AlN film shows a negative dichroism after the band edge. Generally, near the band gap, the fundamental absorption occurs due to the contribution of excitonic and band-to-band transitions. For

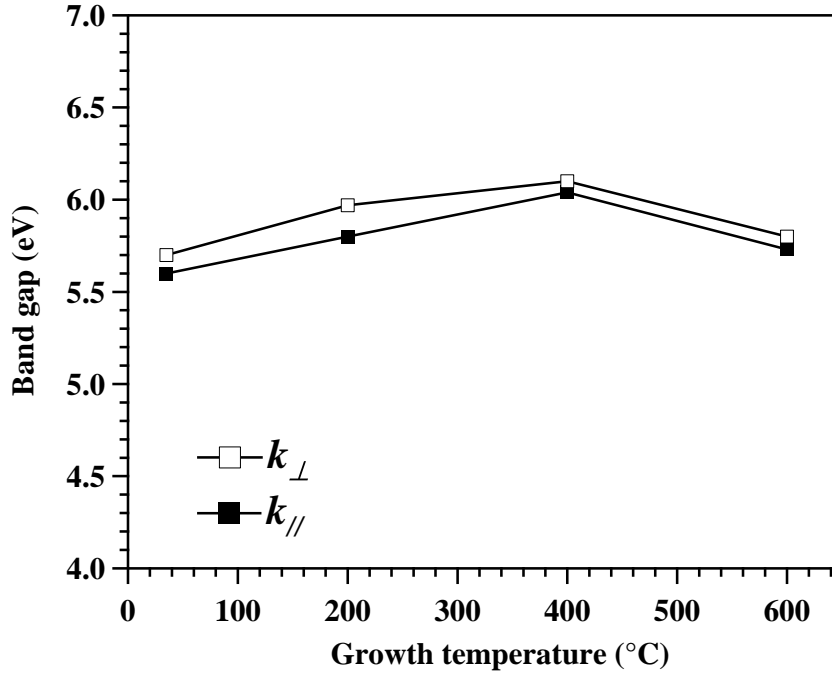


**Figure 3.19** – Optical band gaps of AlN films with  $T_s$  for  $k_{\perp}$  and  $k_{\parallel}$ .

wurzite structure AlN, the excitonic transition strongly depends upon polarization state of light due to the non-cubic crystal-field splittings [30, 31]. Therefore, the anisotropy properties strongly affected near the band gap, which results a strong  $\Delta n$ . In this study, AlN grown at 400 °C is a highly *a-axis* oriented normal to the substrate compared to other films. Therefore, it shows a strong birefringence ( $\sim 0.03$ ) at lower energy range. However, birefringence disappears at energies 5.55 and 6.11 eV and reappear with a negative value ( $-0.01$ ) at 5.9 eV. The birefringence of *a-axis* oriented AlN film exhibited a lower value compared to the reported *c-axis* oriented AlN film ( $\Delta n = -0.05$  at 5.9 eV) [91]. Also, it is seen that *a-plane* (*m-plane*) LED exhibited an isotropic emission pattern along the surface normal compared to the *c-plane* structure at wavelength of 210 nm [28]. So, this film (*a-axis*) contains a mixed  $\sigma$  and  $\pi$  exciton feature that decreases the value of both  $\Delta n$  and  $\Delta k$  near the band gap.

The parameters of the modified Forouhi-Bloomer dispersion model were extracted from

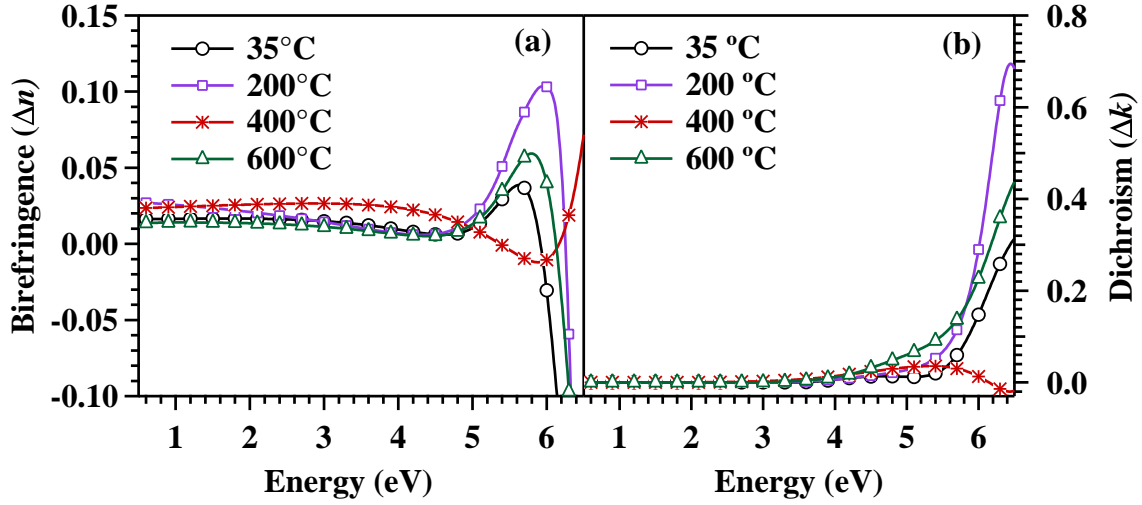


**Figure 3.20** – The dispersion of (a) birefringence ( $\Delta n$ ) (b) and dichroism ( $\Delta k$ ) with energy at different  $T_s$ .

the fitting and shown in Fig. 3.21. The  $\Gamma_j$  and  $f_j$ , both decrease with  $T_s$  upto 400 °C. The broadening parameter  $\Gamma_j$  ( $= \hbar/\tau_j$ , where  $\tau_j$  is the phonon relaxation time), is the inverse of relaxation time, depends on the phonon contribution and microstructural parameters, such as static impurities, defect density, strain, grain boundary, grain sizes, etc [106]. A decrease in  $\Gamma_j$  is observed with the increase in  $T_s$  and implies an increase in phonon relaxation time due to the increase in crystallite size as well as decrease in residual stress.  $\omega_j$  defines the energy at which the extinction coefficient is maximum for a material and it increases with  $T_s$  due to increase in band gap, whereas energy from which the absorption starts ( $\omega_g$ ) is almost constant. So, at 400 °C, AlN film shows high  $n$  as well as low  $k$  with higher value of  $\omega_j$  among all due to higher purity, larger crystallite size and also highly oriented.

### 3.6 Conclusion

AlN thin films have grown using reactive magnetron sputtering at different growth temperatures ( $T_s$ , 35 to 600 °C). All these films are crystallized with wurtzite structure and



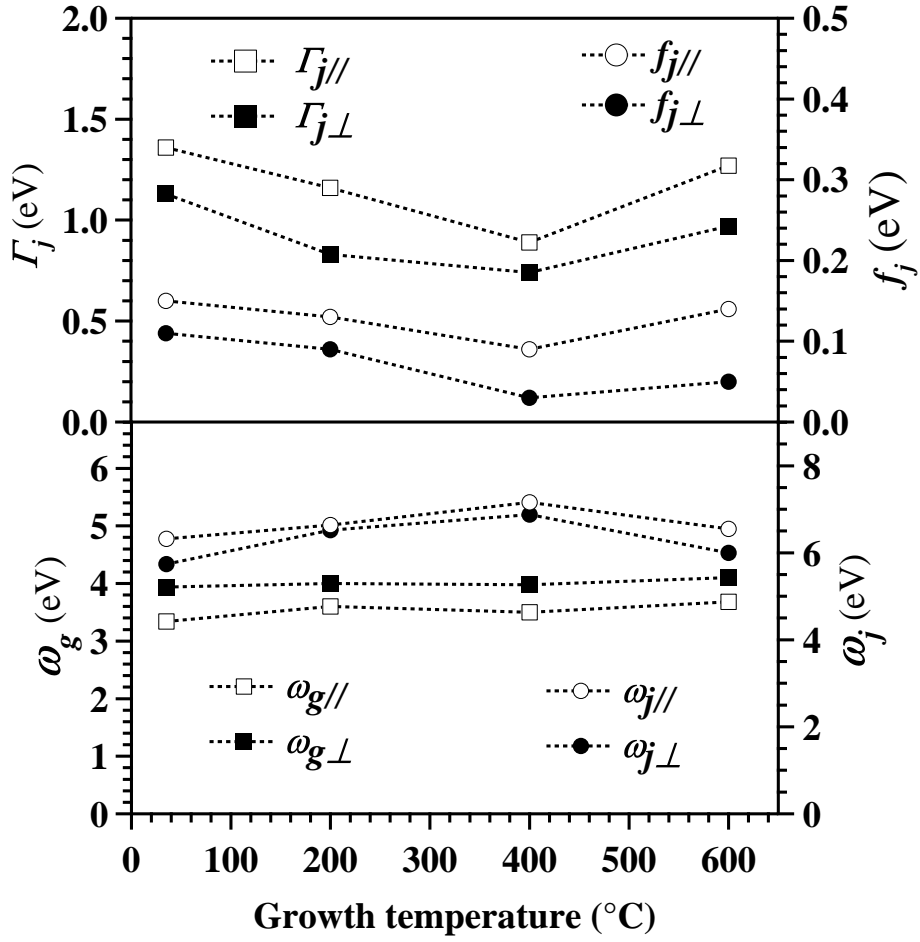


**Figure 3.21** – Dispersion parameters derived from the fitting with  $T_s$ .

the  $T_s$  influences the orientation of these films. The crystallinity is increased with  $T_s$  and a preferential *a-axis* orientation is observed at 400 °C. The cross section and SAED pattern of AlN films showed a high degree of alignment (columnar structure) as well as the orientation. The surface morphology, RMS roughness and average grain size are also strongly influenced by the  $T_s$ . However, the residual stress measurement by  $\sin^2\psi$  technique exhibits a transition from tensile to compressive between 200 to 400 °C growth temperature. Nano-indentation hardness studies on these films revealed that the indentation hardness ( $H$ ) varied between 13.0 to 18.5 GPa, where as at 400 °C AlN film exhibited a relatively high elastic modulus ( $E = 238$  GPa) due to the  $B_1$  type of bonding which is more covalent in nature. Uniaxial anisotropic optical properties of these films with different  $T_s$  are

investigated by SE technique, which are strongly depend on  $T_s$ . Highly *a-axis* oriented AlN film grown at 400 °C, exhibited high  $n$  ( $n_{\perp} = 2.55$ ,  $n_{\parallel} = 2.57$ ) and low  $k$  ( $k_{\perp} = 0.21$ ,  $k_{\parallel} = 0.25$ ) at 210 nm (deep-UV region) with low value of  $\Delta n$  (-0.01) and  $\Delta k$  (0.03). With increase in  $T_s$ , the band gap also increased upto 400 °C, which is close to the bulk AlN. So, the anisotropy optical properties of *a-axis* AlN can be effectively used in UV-LED and electro-luminescent diode based polarization-sensitive optoelectronic applications.

# Chapter 4

## Significance of Ti on local crystal structure and mechanical properties of $\text{Al}_{1-x}\text{Ti}_x\text{N}$ thin films

### 4.1 Introduction

Addition of transition elements to AlN such as Ti, Cr and Zr have yielded ternary nitrides with higher hardness, superior oxidation resistance, good wear and corrosion resistance [70–73]. Amongst, Ti doped AlN films have revealed as a n-type ferromagnetic material for dilute magnetic semiconductor (DMS) applications at room temperature, reported both by first principle calculation as well as experimental methods [66, 67, 69, 136].  $\text{Al}_{99}\text{Ti}_1\text{N}$  film deposited on optical fiber is used in infrared whispering gallery modes microlaser in the range of 775 to 800 nm for biomedical applications [74, 75]. Exploring the possibility of heavy transition metal doping to group III nitride materials for photoelectric conversion under visible light, this Ti doped AlN is expected as a potential candidate for efficient solar energy conversion [76]. In addition, doping of Ti to AlN lattice reveals the improvement of piezoelectric response as compared to pristine AlN [78].

The present chapter describes about the growth of  $\text{Al}_{1-x}\text{Ti}_x\text{N}$  thin films by reactive magnetron co-sputtering at different Ti concentrations and the crystallographic structure,

surface chemical analysis and morphology of these films are investigated by GIXRD, XPS and AFM. Doping concentration, position of dopant and their local crystal structure are very important factors that affect the physical and mechanical properties of these films. Therefore, the local crystal structure around Ti dopant in these thin films are analyzed by X-ray absorption spectroscopy (XAS) technique *i.e.* both X-ray absorption near-edge structure (XANES) and extended X-ray absorption fine structure (EXAFS). Since, Ti doped AlN films are used predominantly in optoelectronic devices, so it is crucial to investigate the mechanical properties, because of contact loading/unloading during processing and fabrication that degrade the efficiency of the devices. Hence, the nano-indentation technique is used to investigate the mechanical properties of these films.

## 4.2 Growth and crystallographic studies of $\text{Al}_{1-x}\text{Ti}_x\text{N}$ thin films

$\text{Al}_{1-x}\text{Ti}_x\text{N}$  films ( $x = 0, 1.5, 3$  and  $4$  at%) were grown on Si(100) substrate by reactive magnetron co-sputtering technique from a  $4\text{N}$  pure,  $50$  mm diameter Al and Ti targets in Ar and  $\text{N}_2$  gas environment. Before deposition, the Si wafers are cleaned by the standard RCA procedure.  $\text{Al}_{1-x}\text{Ti}_x\text{N}$  films were grown at constant flow of argon to nitrogen ratio, target to substrate distance (TSD) and growth temperature by changing the Ti sputtering power, that are listed in section 2.3.2.

GIXRD profiles of  $\text{Al}_{1-x}\text{Ti}_x\text{N}$  thin films with different Ti concentrations ( $x = 0, 1.5, 3$  and  $4$  at%) are shown in Fig. 4.1. All these films exhibit poly-crystalline wurtzite hexagonal structure of AlN and concur with the ICDD data 25-1133. It is ascertained that these Ti atoms are dissolved well in the host AlN lattice, in the absence of any other secondary peaks corresponding to Ti metal/compound.

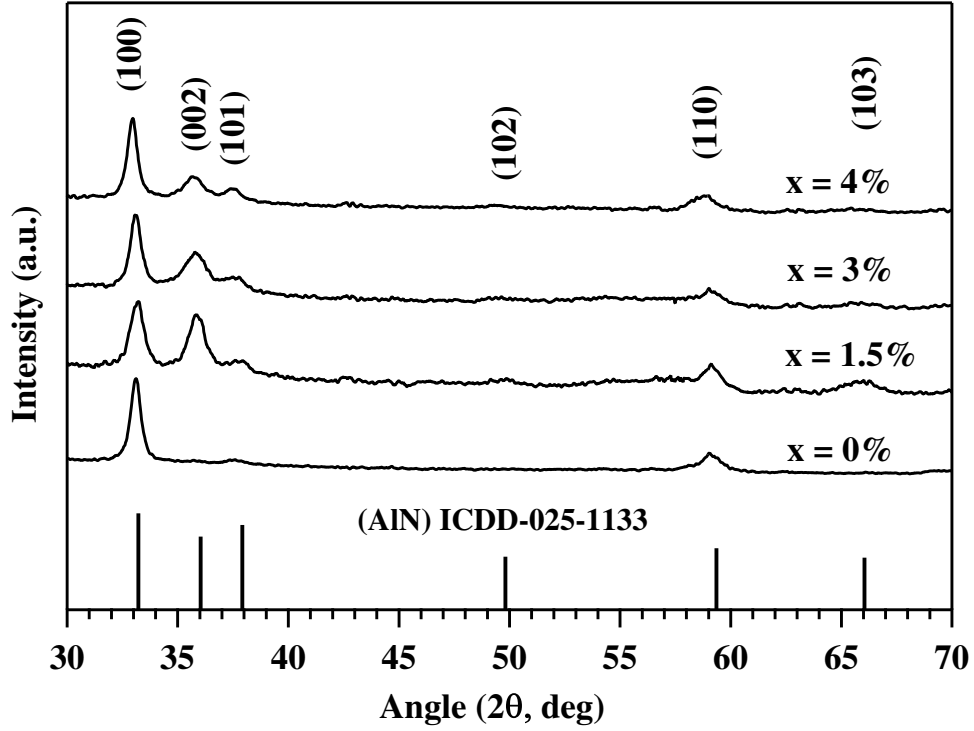


**Figure 4.1** – GIXRD profiles of  $\text{Al}_{1-x}\text{Ti}_x\text{N}$  thin films with  $x = 0, 1.5, 3$  and  $4 \text{ at}\%$ .

From the Fig. 4.1, it can be seen that a consistent shift in the peak position of AlN crystal planes towards lower  $2\theta$  values with the increase in Ti concentration compared to ICDD standard data. Since, the atomic radius of Ti is larger than Al, it can induce a tensile stress in these films and a corresponding peak shift towards lower  $2\theta$ . Hence, Williamson-Hall (W-H) method is used to extract the average strain and crystallite size of these thin films. The induced strain ( $\epsilon$ ) and mean crystallite size ( $D$ ) in these  $\text{Al}_{1-x}\text{Ti}_x\text{N}$  films are estimated using the below equation

$$\beta \cos \theta = \frac{K\lambda}{D} + 4\epsilon \sin \theta \quad (4.1)$$

where  $\beta$  is the FWHM of diffraction peaks and  $K$  is the Scherrer constant (0.9) [95]. W-H plot *i.e.*  $\beta \cos \theta$  as a function of  $4 \sin \theta$  is shown in Fig. 4.2 for  $\text{Al}_{1-x}\text{Ti}_x\text{N}$  films with

$x = 0$  and 4 at%, only. The strain and crystallite size are calculated from the slope and y-intercept of the linear fit to the data, respectively.

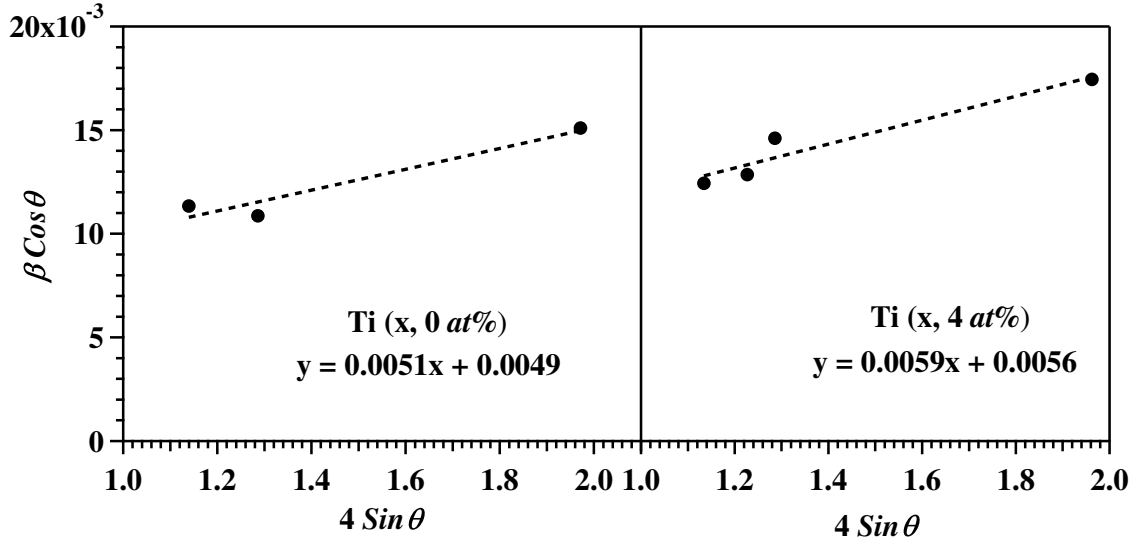


**Figure 4.2** – W-H plots of  $Al_{1-x}Ti_xN$  films with  $x = 0$  and 4 at%.

$x$ (at%)	$D$ (nm)	$\epsilon$ ( $10^{-3}$ )
0	29	5.1
1.5	27	5.2
3	26	5.5
4	24	5.9

**Table 4.1** – Crystallite size ( $D$ ) and strain ( $\epsilon$ ) of  $Al_{1-x}Ti_xN$  thin films with  $x = 0, 1.5, 3$  and 4 at%.

The average crystallite size and strain of  $Al_{1-x}Ti_xN$  films with different concentration are shown in Table 4.1. The crystallite size shows a consistent decline with respect to Ti concentration. Pristine AlN ( $x = 0$  at%) grown at a sputtering pressure of  $5 \times 10^{-3}$  mbar, has a crystallite size of around 29 nm. Ti atoms are doped in AlN by the reactive co-sputtering technique that increases the sputtering pressure due to increase in Ti sputtering power as listed in Table 4.1. Thus, sputtered atoms from the target encounter many collisions before it reaches the substrate due to decrease in mean free path and hence reduces the ad-atom energy. So, the crystallite size gradually decreases

along with Ti concentration. Also, the atomic radius of Ti atom (1.46 Å) is larger than that of Al (1.43 Å), the substitute doping of Ti atom in AlN lattice expands the lattice parameter compared to pristine AlN [66, 67, 76]. Therefore,  $\text{Al}_{1-x}\text{Ti}_x\text{N}$  films exhibit tensile strain that increase with the Ti concentration, which is shown in Table 4.1.

### 4.3 Surface chemical analysis

For surface chemical analysis, XPS is used to explore the core electron binding energies of  $\text{Al}_{1-x}\text{Ti}_x\text{N}$  thin films and quantify the Ti concentration. The convolution of a Gaussian and a Lorentzian function is used to fit the high-resolution core level XPS spectra for Al 2*p*, N 1*s* and Ti 2*p* and the resultant binding energy is extracted, which is shown in Table 4.2. For discussion, a representative fitted core level spectrum corresponding to  $\text{Al}_{1-x}\text{Ti}_x\text{N}$  film with  $x = 4 \text{ at}\%$  after Shirley background subtraction is shown in Fig. 4.3.

x (%)	Al 2 <i>p</i> (eV)		N 1 <i>s</i> (eV)		Ti 2 <i>p</i> <sub>3/2</sub> (eV)
	Al-N	Al-O	Al-N	N-C	Ti-N
0	74.1	75.1	397.2	399.0	
1.5	74.1	75.0	397.2	399.0	455.0
3	74.3	75.1	397.2	398.9	455.2
4	74.2	75.0	397.1	399.0	455.3
Ref. [137]	74.4	75.0	397.5	398.7	
Ref. [138]	74.1		397.2		454.9
Ref. [139]	73.6 - 74.6	74.7 - 75.6	396.8 - 397.9		
Ref. [70, 140, 141]	74.1		396.5		454.8 - 455.1

**Table 4.2** – Binding energy of  $\text{Al}_{1-x}\text{Ti}_x\text{N}$  thin films with references.

Fig. 4.3(a), the convolution of a Gaussian and a Lorentzian function is used to fit the high-resolution core level Al 2*p* spectra. For simplification, the spin-orbit components of Al 2*p* spectra have been neglected in the curve fitting. In Al 2*p* profile, the strong intensity peak having area 85% of the original peak is found at 74.2 eV. This binding energy is

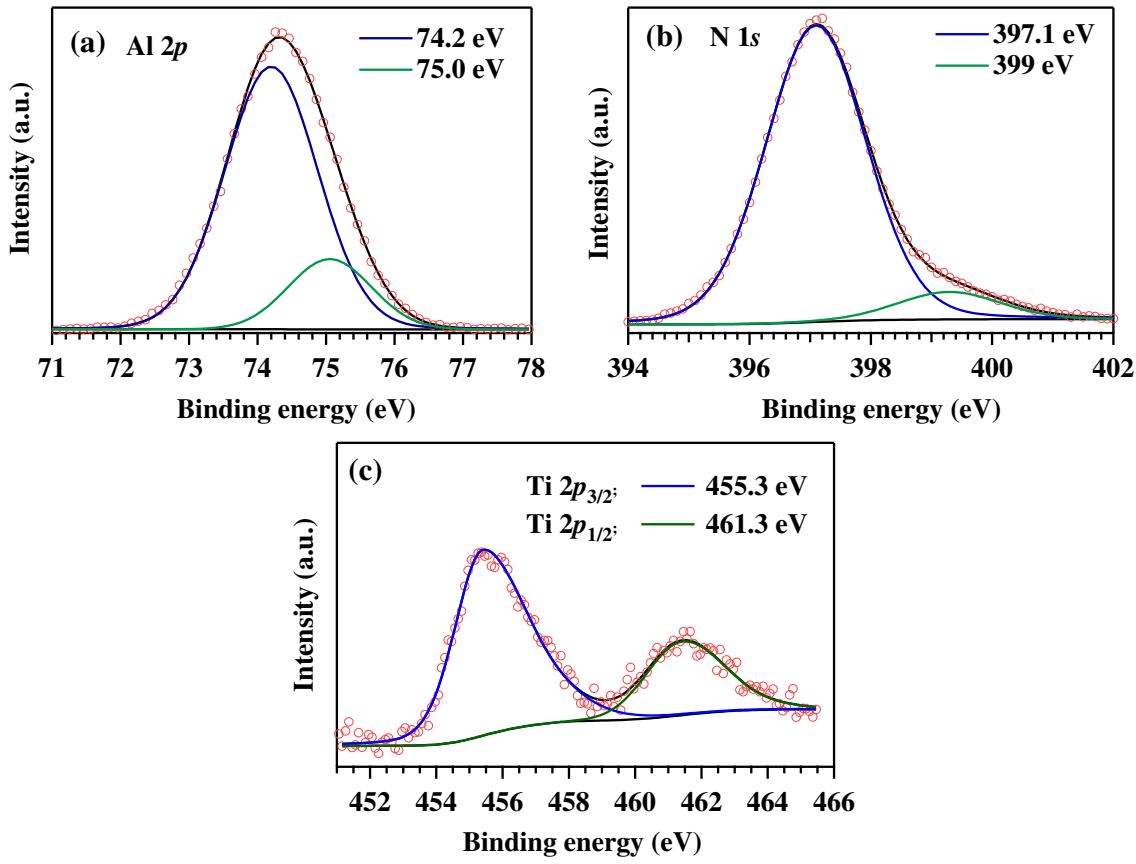


**Figure 4.3** – High resolution XPS spectra of (a) Al 2*p*, (b) N 1*s* and (c) Ti 2*p* for Al<sub>1-x</sub>Ti<sub>x</sub>N film with  $x = 4$  at%.

assigned to Al-N bond formation as it appears in the span of 73.6 to 74.6 eV. [70, 82, 137–139, 142] However, the second peak is observed at 75.0 eV that correlate to the Al-O bond as described in the span of 74.7 to 75.6 eV [137, 139]. Thermodynamically Al-O reaction is more commendatory compared to Al-N, since Al has high chemical affinity to oxygen, as deposition is performed at lower partial pressures ( $10^{-3}$  mbar) [82, 139]. Therefore, a detectable amount of oxygen impurity present in these films. However, there is no indication of Al cluster formation, which is expected in the span of 72.2 to 72.7 eV [137]. Similarly, the core spectra of N 1*s* has analyzed and is shown in Fig. 4.3(b). The intense peak having area 92% of original profile is found at 397.1 eV, which is allocated to Al-N bond [82, 138, 142]. A second peak is found at a binding energy 399 eV that corresponds to N-C bond in the form of triple (nitrile) and / or double (imine) bonds



[137, 143]. The core spectra of Ti shown in fig. 4.3(c) was analyzed with the help of asymmetric Doniach-Sunjic parameter towards higher binding energies. Also, the peaks having binding energy as 455.3 and 461.3 eV correspond to the Ti-N bond of  $2p_{3/2}$  and  $2p_{1/2}$ , respectively. Sufficient number of recent reports discussing the binding energy for Ti-N bond formation is also similar to this range and clearly different from the binding energy for the formation of Ti clusters (453.8 eV) [69, 70, 140, 141].

## 4.4 Morphology and surface roughness by AFM

AlN thin film is a potential candidate in surface and bulk acoustic wave devices due to high acoustic velocity. Surface acoustic waves could travel through the surface of the material which possess very small surface roughness has less propagation loss [37]. In this study, surface micro-structure and roughness of  $\text{Al}_{1-x}\text{Ti}_x\text{N}$  films are carried out by AFM technique. AFM images over  $1 \times 1 \mu\text{m}^2$  surface area of  $\text{Al}_{1-x}\text{Ti}_x\text{N}$  films with  $x = 0$  and 4 at% are shown in Fig. 4.4.

$\text{Al}_{1-x}\text{Ti}_x\text{N}$  films exhibit smooth morphology with pebble-like grain structure. The average ( $R_a$ ) and root mean square roughness ( $R_{rms}$ ) of these films is extracted from AFM. For pristine AlN film, the  $R_a$  and  $R_{rms}$  is around 2.0 and 2.6 nm, respectively. Whereas, the roughness ( $R_a$ ,  $R_{rms}$ ) is decreased as (1.6, 1.8), (1.4, 1.6) and (1.2, 1.5) nm with addition of Ti as 1.5, 3 and 4 at%, respectively. The roughness shows a similar behaviour with crystallite size as described in Table 4.1 *i.e.* surface roughness decreases with the decrease in grain growth.

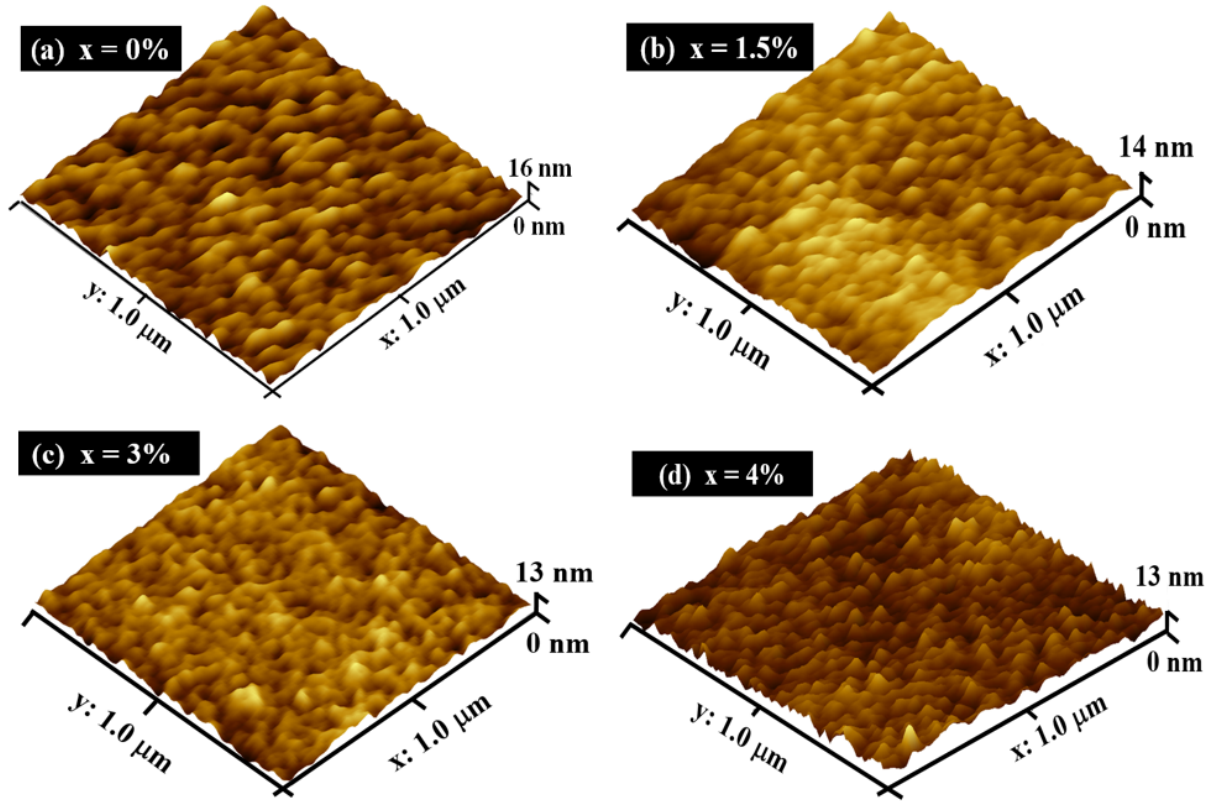


**Figure 4.4** – AFM images of  $\text{Al}_{1-x}\text{Ti}_x\text{N}$  films at (a)  $x = 0$ , (b)  $x = 1.5$ , (c)  $x = 3$ , and (d)  $x = 4$  at%.

## 4.5 Local crystal structure at vicinity of Ti in AlN: XAS

XAS is broadly classified into two important parts i.e. XANES and EXAFS after the edge. Ti K-edge absorption spectra of  $\text{Al}_{1-x}\text{Ti}_x\text{N}$  films are shown in Fig. 4.5 to investigate the local structure of the Ti dopant in the AlN lattice.

### 4.5.1 XANES analysis

XANES is very sensitive to the geometrical arrangements of X-ray absorbing atom (symmetry e.g. octahedral, tetrahedral coordination) in the host material. It can be seen from Fig. 4.5 that K-edge absorption spectra of Ti in  $\text{Al}_{1-x}\text{Ti}_x\text{N}$  films show a pre-edge peak

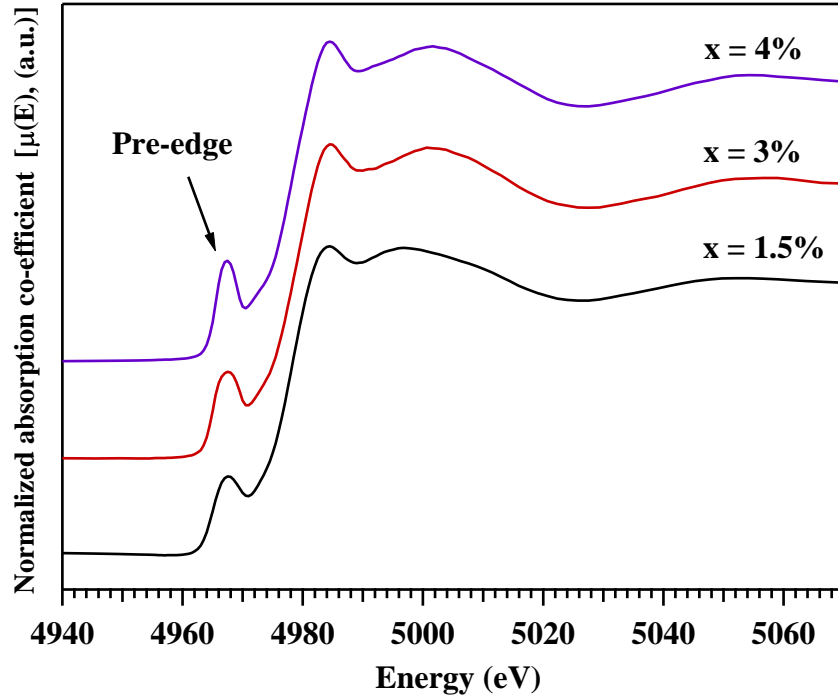


**Figure 4.5** – Ti K-edge absorption spectra of  $\text{Al}_{1-x}\text{Ti}_x\text{N}$  films.

around 4967 eV. Tatemizo *et al* and Tuilier *et al* have reported a pre-edge peak for K-edge absorption spectra of Ti in doped AlN films is around 4966 eV and in Al-rich  $\text{Ti}_{1-x}\text{Al}_x\text{N}$  composite films is around 4969 eV, respectively [76, 144]. They have concluded that Ti atoms occupy the cation (Al) site of hexagonal AlN structure and forms localized TiN species. Usually, the pre-edge peak for Ti K-edge appears at 4964 eV for Ti metal and low intense peak around 4969-4971 eV for octahedral coordination of cubic TiN lattice [76, 144]. In this study, the pre-edge peak position at 4967 eV is in consistent with tetrahedrally coordinated TiN species in wurtzite hexagonal AlN lattice [145]. Normally, this pre-edge peak is a signature of  $1s$  to  $3d$  electronic transitions of transition metals [146, 147]. However, for symmetric groups having center of inversion, this transition is forbidden by Laporte selection rule ( $\Delta l = \pm 1$ ) [148]. AlN has a distorted tetrahedron structure, where one Al atom forms covalent bond with three N atoms at the base (bs - basal) having bond length 0.1885 nm and an ionic Al-N bond at the apex (ax - axial)

having bond length 0.1997 nm [12]. Hence, AlN has no centre of symmetry due to the  $C_{3v}$  point group and Ti doped AlN partially allows the  $1s$  to  $3d$  electronic transition [76, 136, 147]. Additionally, it is also reported that transition metal atom replaces Al atom in AlN lattice and forms the  $p-d$  hybridization between it's neighbouring N atoms [81, 136, 146, 147]. Therefore, Ti K-edge absorption spectra of  $\text{Al}_{1-x}\text{Ti}_x\text{N}$  films show a strong pre-edge peak at 4967 eV due to the  $p-d$  mixing [76, 144, 146]. In this study, the XANES analysis is conforming that Ti replaces the Al atom tetrahedrally in AlN matrix and leads to form TiN species with  $p-d$  mixing.

x (at%)	Energy (eV)	Intensity
1.5	$4967.0 \pm 0.2$	0.25
3	$4967.0 \pm 0.2$	0.27
4	$4967.0 \pm 0.2$	0.31

**Table 4.3** – Pre-edge position of  $\text{Al}_{1-x}\text{Ti}_x\text{N}$  films in Ti K-edge absorption spectra.

The pre-edge peak positions and intensity of  $\text{Al}_{1-x}\text{Ti}_x\text{N}$  films are shown in Table 4.3. It is exhibited that the intensity of the pre-edge peaks increase with the Ti concentration, however the pre-edge energy is not changed. It is also confirmed from XANES that Ti forms distorted tetrahedron structure with surrounding nitrogen atom and form  $p-d$  hybridization. Since, the ionic radius of Ti ( $0.68 \text{ \AA}$ ) is larger than that of Al ( $0.51 \text{ \AA}$ ), the doping Ti atom in AlN lattice deforms the tetrahedron surroundings compared to pristine AlN and it increases with Ti concentration. Addition to this, the induced strain in these films increases with the Ti concentration, extracted using W-H method. Hence,  $1s - 3d$  transition strength increases with higher Ti concentration.

### 4.5.2 EXAFS analysis

For the EXAFS, oscillation part of the measured absorption co-efficient ( $\mu(E)$ ) is converted to the fine structure function  $\chi(E)$  as described in section 2.5. Finally,  $\chi(R)$  versus radial distances ( $R$ ) plots are used to extract the co-ordination number, radial distances and neighbouring atoms of the dopant in different co-ordination spheres. Wurtzite hexagonal AlN phase has been used as crystallographic inputs for the fitting of these spectra.

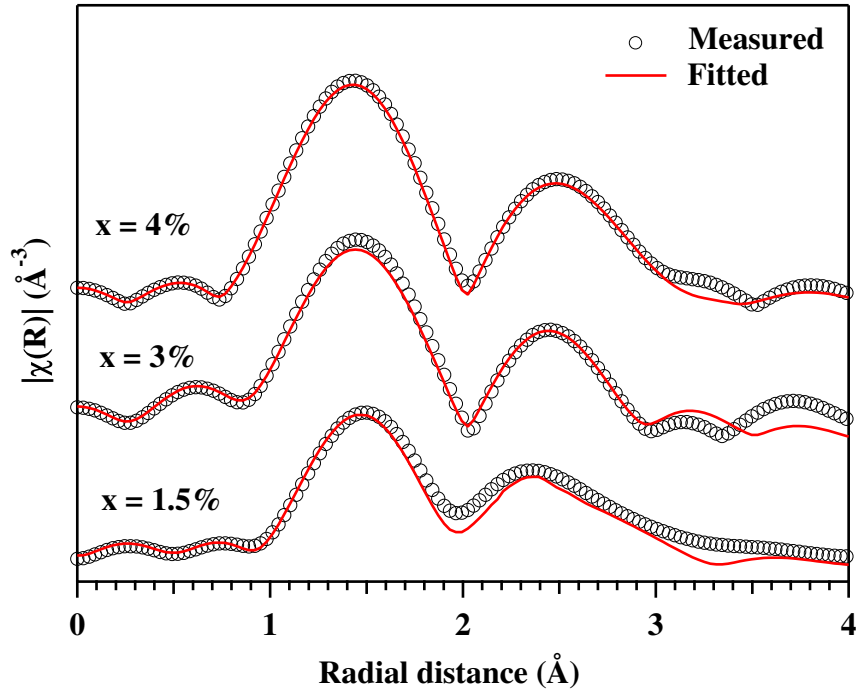


**Figure 4.6** – Extended region fitting using ARTEMIS in R-space of  $\text{Al}_{1-x}\text{Ti}_x\text{N}$  thin films.

Three single scattering paths are considered for EXAFS analysis as one path for basal nitrogen  $[(\text{Ti-N})_{bs}]$ , second path for the axial nitrogen  $[(\text{Ti-N})_{ax}]$  from the first coordination sphere and third path as Ti-Al from the second coordination sphere. Since the ranks of multiple scattering paths are very low, only the single scattering paths are included in the analysis. The overall value of R-factor is then minimized to establish the goodness of fit. The fitted EXAFS oscillation  $\chi(k)$  curves in R-space are shown in Fig. 4.6. The

bond lengths of Ti-N and Ti-Al paths as well as the corresponding co-ordination numbers (C.N) of each path ( $NS_0^2$ ,  $N$ =degeneracy of path), Deby-waller factor ( $\sigma^2$ ) and R-factor, are observed from the EXAFS and are shown in Table 4.4.

#### 4.5.2.1 Discussion on coordination number and bond length

The total coordination number (axial and basal) of Ti with N atom in the first coordination sphere of these  $\text{Al}_{1-x}\text{Ti}_x\text{N}$  thin films are 3.70, 3.75 and 3.93 for  $x = 1.5, 3$  and  $4 \text{ at\%}$ , respectively. For AlN, the stoichiometric coordination number of Al atom with N is 4 in the first coordination sphere. So Ti dopant in these films show a nearly stoichiometric coordination with N atom. similar to Al atom in AlN lattice. However, it is observed that the coordination number of Ti in the second sphere with Al atom are 8.35, 8.46 and 8.40 for  $x = 1.5, 3$  and  $4 \text{ at\%}$ , that is lower than the Al-Al in second coordination sphere ( $\sim 12$ , AlN lattice) *i.e.*. This signifies that it possess Al vacancies in second coordination sphere. Thus, all these films exhibit a constant coordination number in both first and second sphere, which is independent of Ti concentration.

The  $(\text{Ti-N})_{ax}$  and  $(\text{Ti-N})_{bs}$  bond length variation as a function of Ti concentration of first coordination sphere in  $\text{Al}_{1-x}\text{Ti}_x\text{N}$  films are shown in Fig. 4.7. Since, ionic radius of  $\text{Ti}^{3+}$  ( $0.68 \text{ \AA}$ ) is larger than the Al ( $0.51 \text{ \AA}$ ), so the Ti-N bond along both axial and basal has increased compared to the pristine AlN. However, the bond length for  $(\text{Ti-N})_{ax}$  reduces with the Ti concentration, whereas  $(\text{Ti-N})_{bs}$  bond length decreases moderately with Ti. This result is very similar with lower magnitude order as Cr doped AlN films grown by co-sputtering technique, which is discussed in chapter-5. Abdul *et al* and Fan *et al* have reported that Ti doped AlN exhibits ferromagnetic properties due to strong  $p - d$  hybridization mechanism between the doping element and the host atoms by the first principles calculations [66, 136]. It is also reported by Bannikov *et al* that

Sample	Paths	Bond length (Error)(Å)	C.N. (Error)	$\sigma^2$ (Å) <sup>2</sup> (Error)	R
x = 1.5%	(Ti-N) <sub>ax</sub>	2.082	0.90	0.0031	0.04
		(0.007)	(0.07)	(0.0006)	
	(Ti-N) <sub>bs</sub>	1.938	2.80	0.0033	
		(0.004)	(0.06)	(0.0005)	
	Ti-Al	3.094	8.35	0.0210	
		(0.008)	(0.13)	(0.0004)	
x = 3%	(Ti-N) <sub>ax</sub>	2.070	1.00	0.0037	0.02
		(0.005)	(0.06)	(0.0004)	
	(Ti-N) <sub>bs</sub>	1.932	2.75	0.0032	
		(0.005)	(0.04)	(0.0005)	
	Ti-Al	3.081	8.46	0.0262	
		(0.006)	(0.06)	(0.0003)	
x = 4%	(Ti-N) <sub>ax</sub>	2.064	1.00	0.0030	0.01
		(0.004)	(0.02)	(0.0006)	
	(Ti-N) <sub>bs</sub>	1.930	2.93	0.0033	
		(0.004)	(0.05)	(0.0001)	
	Ti-Al	3.087	8.40	0.0251	
		(0.006)	(0.04)	(0.0004)	

**Table 4.4** – The fitting path parameters of Al<sub>1-x</sub>Ti<sub>x</sub>N thin films

covalent bond strength increases by the addition of Ti in cubic AlN with the help of charge density distribution theory [67]. Therefore, the bond length in first coordination sphere in Al<sub>1-x</sub>Ti<sub>x</sub>N films decreases gradually with the Ti concentration and indicates a strong  $p - d$  hybridization which is also seen from XANES analysis. From Table 4.4, it can be seen that the bond length of Ti with Al in second coordination sphere is around 3.08 Å which is similar to that of Al-Al (3.14 Å) in bulk AlN as calculated by Cui *et al* using density functional theory [79]. In this study, EXAFS confirms that Ti atom forms distorted tetrahedral structure by replacing Al atom in AlN lattice, which is also corroborated with the observation of XRD, XPS and XANES studies without any other Ti clustering in Al<sub>1-x</sub>Ti<sub>x</sub>N thin films.

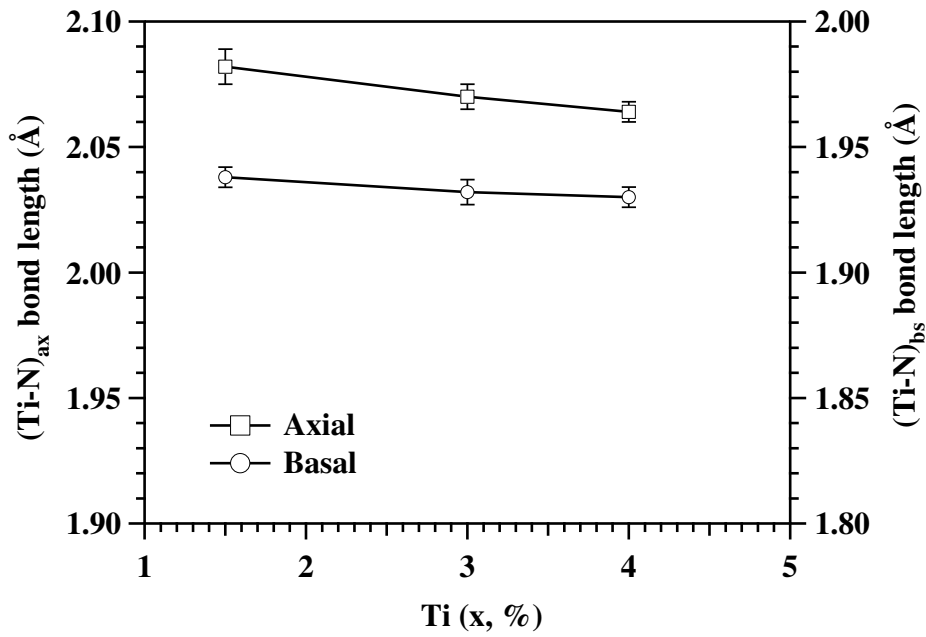


**Figure 4.7** –  $(\text{Ti-N})_{ax}$  and  $(\text{Ti-N})_{bs}$  bond lengths are shown with Ti concentration of  $\text{Al}_{1-x}\text{Ti}_x\text{N}$  films.

## 4.6 Mechanical properties

Nanomechanical characterization is performed by nano-indentation technique as a function of depth (20 nm to 650 nm) to understand the deformation behavior of  $\text{Al}_{1-x}\text{Ti}_x\text{N}$  thin films. Fig. 4.8 and Fig. 4.9 show the indentation hardness ( $H$ ) and modulus ( $E$ ) of Si (100) substrate and  $\text{Al}_{1-x}\text{Ti}_x\text{N}$  films with  $x = 0$  to 4 at%, respectively. It is well known that the average surface roughness ( $R_a$ ) causes an uncertainty in indentation contact area due to asperity contact at very shallow depths (less than  $20 \times R_a$ ) [149]. In this study, the average surface roughness of these films are around maximum of 2 nm. Therefore, the  $H$  and  $E$  are studied from the 20 nm depth of the films. The  $H$  and  $E$  of Si is independent of depth as an average value of 11.5 and 175 GPa, respectively. Pristine AlN film shows a constant hardness value around 17.5 GPa from 20 to 60 nm and afterwards it decreases slightly with depth. According to indentation thumb rule, the indentation should be performed lower depth than the one-tenth ( $1/10^{th}$ ) of the total



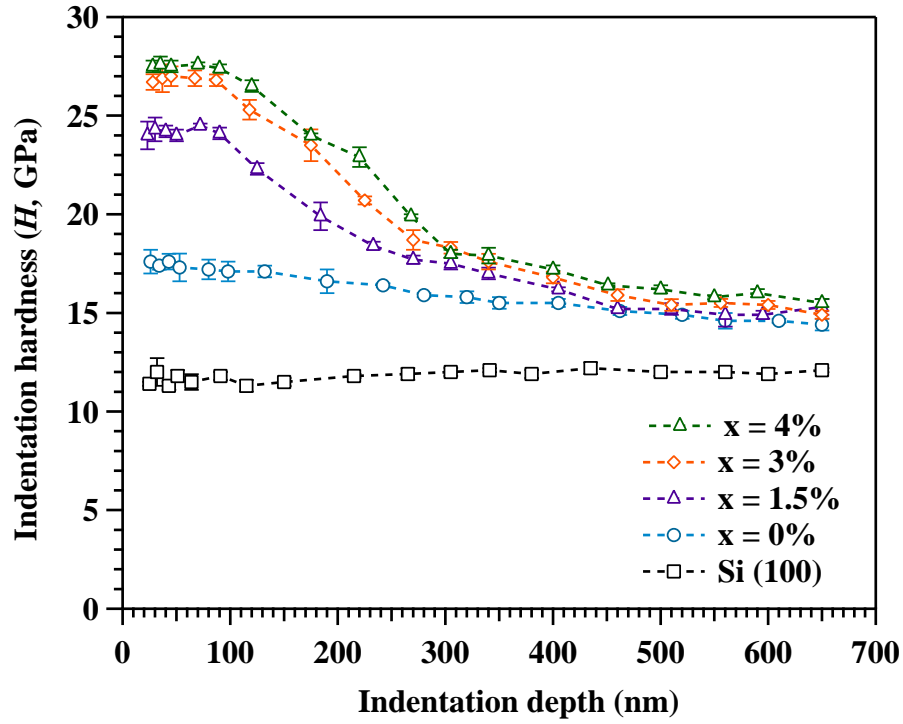


**Figure 4.8** – Indentation hardness as a function of depth of Si (100) substrate and  $\text{Al}_{1-x}\text{Ti}_x\text{N}$  films with  $x = 0$  to 4 at%.

film thickness to ascertain the film hardness by avoiding the substrate effect [150]. In this study, thickness of these  $\text{Al}_{1-x}\text{Ti}_x\text{N}$  films are around 400 nm. So, the hardness decreases gradually at higher depth due to the substrate effect. Ti doped AlN films also exhibit a similar behavior as pristine AlN film. The modulus ( $E$ ) of these films decreased rapidly with depth and reached the substrate modulus value at higher depths, which is shown in Fig. 4.9. The  $H$  and  $E$  of  $\text{Al}_{1-x}\text{Ti}_x\text{N}$  films are extracted at a depth of 35 nm which is shown in Fig. 4.10, according to less than the  $1/10^{\text{th}}$  depth rule.

In Fig. 4.10, it is seen that both  $H$  and  $E$  of  $\text{Al}_{1-x}\text{Ti}_x\text{N}$  films are gradually increased with  $x = 0$  to 4 at%. Mechanical properties of thin film generally depends on its microstructure *i.e* crystallite size of material, plane orientation, planar density, bond strength and induced stress during the growth. In this study, we have observed crystallite size reduction with Ti concentration as 29 nm to 24 nm and shown in Table 4.1. According

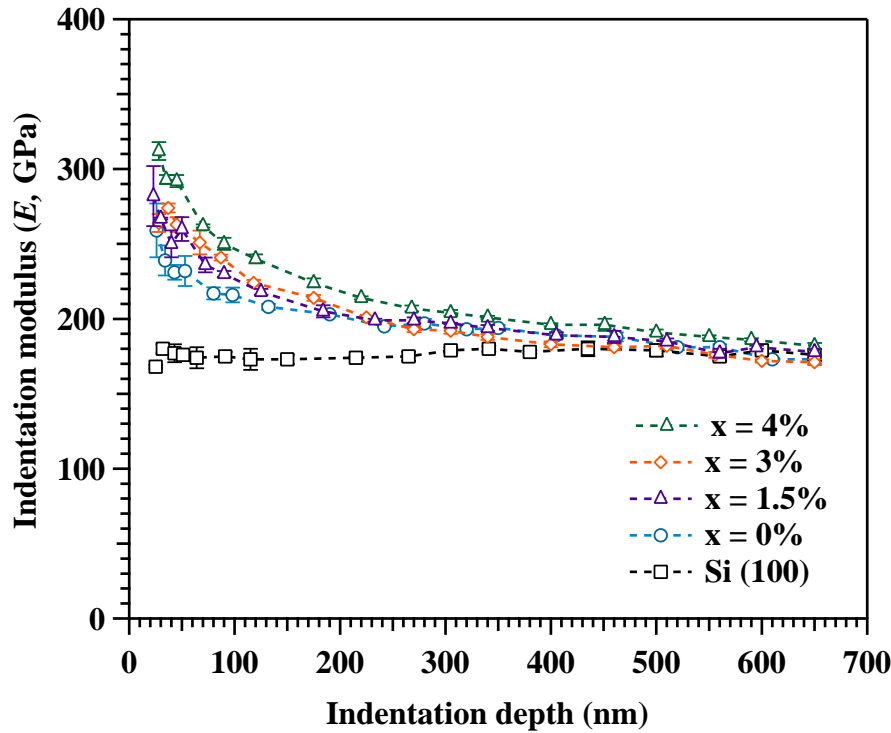


**Figure 4.9** – Indentation modulus as a function of depth of Si (100) substrate and  $\text{Al}_{1-x}\text{Ti}_x\text{N}$  films with  $x = 0$  to 4 at%.

to Hall-Petch relation, the hardness increases with the decrease in crystallite size above critical value of crystallite size (15-18 nm). Therefore, the  $H$  of these films is increased. Addition to this, the induced strain in these films also increased with Ti that is calculated by Williamson-Hall method and is shown in Table 4.1. Also, from XAS study of  $\text{Al}_{1-x}\text{Ti}_x\text{N}$  films, it is confirmed that Ti forms localized TiN species with distorted tetrahedron structure by replacing the Al atom in AlN lattice having a stoichiometry coordination number with N atoms in first coordination sphere. So, the indentation hardness is increased from 17.5 to 27.6 GPa with Ti concentration as 0 to 4 at%. Cai *et al* have reported that the indentation hardness is varied between 28 to 38 GPa for AlTiN films deposited by arc ion plating method using Al (67 at%) and Ti (38 at%) composite targets [71]. Similarly, Jose *et al* have discussed that TiAlN film with 36 at% of Ti shows indentation hardness as 35 GPa due the high density cubic AlN phase formation [73]. However, modulus of films depend on the nature of inter-atomic bond strength in the

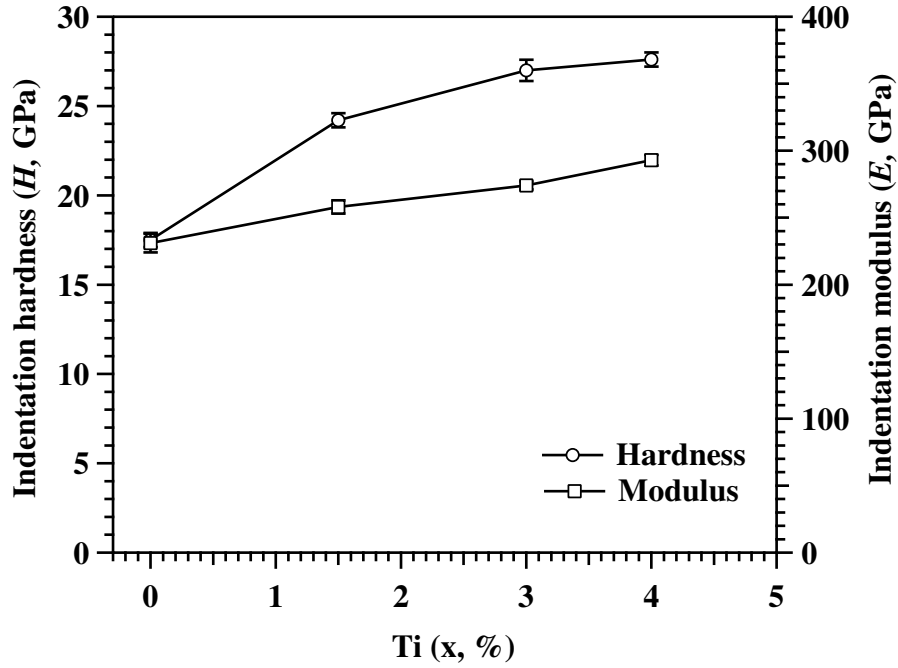


**Figure 4.10** – Indentation hardness and modulus of  $\text{Al}_{1-x}\text{Ti}_x\text{N}$  films as a function of Ti concentrations.

crystal. From EXAFS analysis, it is observed that Ti-N bond length decreased with Ti concentration and a distorted tetrahedral structure formed. Covalent band gap ( $E_h$ ) is related to inter-atomic distance by a relation  $E_h = Kd^{-2.5}$ , *i.e.* the covalent bond strength increases with a decrease in bond length [71]. So, the indentation modulus also increases from 231 to 293 GPa with Ti concentration as 0 to 4 *at%*.

Usually, the indentation impression on films are collected by AFM technique to study the pile-up or sink-in behavior due to plastic deformation [151]. Hence, AFM image of the indentation of  $\text{Al}_{1-x}\text{Ti}_x\text{N}$  thin films with  $x = 0$  and 4 *at%* over a  $2 \times 2 \mu\text{m}^2$  surface area is shown in Fig. 4.11 for a 2 mN indentation load. All these films show a well-defined sink-in indentation behaviour. It is observed that  $\text{Al}_{1-x}\text{Ti}_x\text{N}$  film at  $x = 4$  *at%* shows large sink-in behaviour compared to pristine AlN films without any radial cracks and exhibits a high elastic recovery behaviour *i.e.* high resistance to plastic deformation with

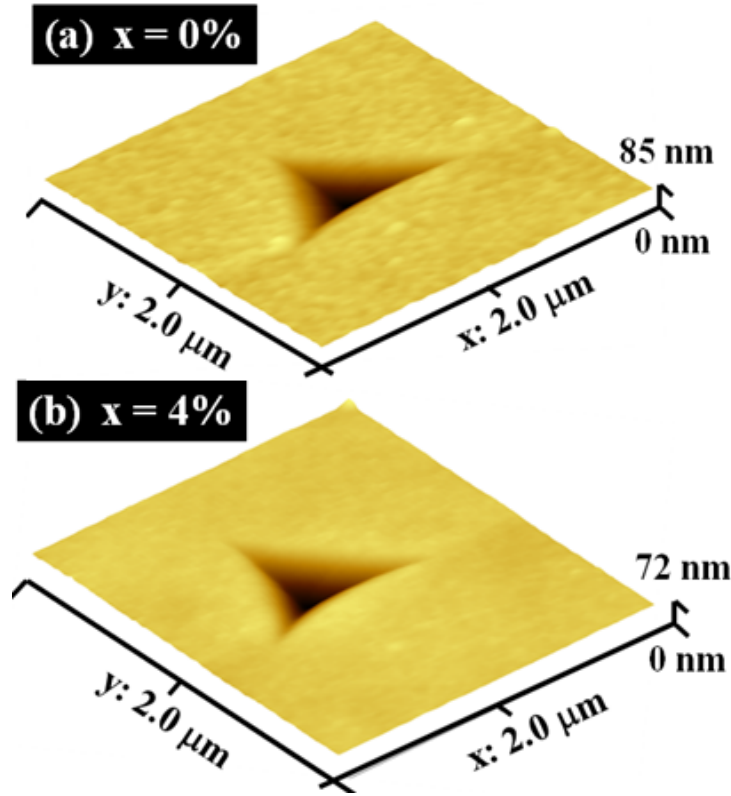


**Figure 4.11** – AFM images of the indentation impressions at 2 mN load of  $\text{Al}_{1-x}\text{Ti}_x\text{N}$  films with  $x = 0$  and 4 at%.

the addition of Ti to AlN lattice.

## 4.7 Conclusion

$\text{Al}_{1-x}\text{Ti}_x\text{N}$  films are grown by co-sputtering technique with various Ti concentration ( $x = 0, 1.5, 3$  and 4 at%). All these films are found to be poly-crystalline wurtzite hexagonal of AlN without any other secondary phases belongs to Ti compound. Ti concentration, chemical analysis and surface morphology of these films are studied by the XPS and AFM. XAS is performed to study the local crystal structure at the environment of Ti dopant that is investigated by both XANES and EXAFS of  $\text{Al}_{1-x}\text{Ti}_x\text{N}$  thin films. It is observed that Ti forms localized TiN species with distorted tetrahedron structure by replacing the Al atom in AlN lattice resulting to a tensile strain. The coordination number of Ti in first sphere shows stoichiometry with N atom, whereas Al vacancies are found in second coordination

sphere. The bond lengths  $(\text{Ti-N})_{ax}$ ,  $(\text{Ti-N})_{bs}$  are found to be moderately decreased with Ti concentration, whereas Ti-Al bond length in second coordination sphere is independent of Ti. Thus, XAS measurement confirms the enhancement of  $p-d$  hybridization between Ti and N atoms in  $\text{Al}_{1-x}\text{Ti}_x\text{N}$  thin films. The  $H$  and  $E$  of  $\text{Al}_{1-x}\text{Ti}_x\text{N}$  films are increased from 17.5 to 27.6 GPa and 231 to 293 GPa, respectively with  $x = 0$  to 4 *at%* having well-defined sink-in indentation impression behaviour without any radial cracks.

# Chapter 5

## Significance of Cr on local crystal structure and mechanical properties of $\text{Al}_{1-x}\text{Cr}_x\text{N}$ thin films

### 5.1 Introduction

Cr doped AlN is reported to exhibit DMS properties with Curie temperature higher than room temperature ( $T_c \geq 800$  K) by both experimental as well as first principle calculation [64, 65, 79]. According to density functional theory (DFT) calculation, Cr doped AlN exhibits a huge magnetic moment ( $3 \mu_B/\text{Cr}$ ) compared to other transition metal dopants. However, the experimentally observed magnetic moment was less than  $1 \mu_B/\text{Cr}$ , due to possible role of Cr clusters, nitrogen vacancies, defects and impurities for the different Cr concentration in AlN lattice [52, 54, 64]. Though Cr ionic radii is larger than the Al atom, still it can settle in the interstitial sites of AlN lattice. Formation of Cr clusters at interstitial sites reduce the total magnetic moment, which increases the antiferromagnetic states [79, 80]. Cui *et. al.* have reported using DFT calculation that the Cr clusters larger than 2 atoms exhibit antiferromagnetic coupling [79]. Hence, the growth of cluster less doped AlN thin films is the first step to achieve the DMS property in these systems. Also, piezoelectric response of Cr doped AlN films is 73% higher than that of the pristine AlN [81]. However, several unique parameters such as doping concentration,

position (substitution/interstitial) and the local environment of doping element play an essential role in the physical properties of doped AlN films, which is mainly controlled by the growth parameters. Therefore, the effect of dopant in the local crystal structure of AlN film needs a fundamental investigation using X-Ray Absorption Spectroscopy (XAS).

The present chapter describes about the growth of  $Al_{1-x}Cr_xN$  thin films by reactive magnetron co-sputtering with different Cr concentrations. The crystallographic structure, surface chemical analysis and morphology of these films are investigated by GIXRD, XPS and AFM technique. The local crystal structure around Cr dopant in these thin films are analyzed by XAS *i.e.* both XANES and EXAFS techniques. The nano-indentation technique is used to investigate the mechanical properties of these films.

## 5.2 Growth and crystallographic studies of $Al_{1-x}Cr_xN$ thin films

$Al_{1-x}Cr_xN$  thin films are grown on silicon (100) substrates by reactive magnetron co-sputtering technique at different Cr concentration ( $x = 0, 2, 4$  and  $6$  at%) from high pure Al and Cr target (4N) in a Ar:N<sub>2</sub> gas mixture. These Si substrates are cleaned by a standard two-step RCA process.  $Al_{1-x}Cr_xN$  films are deposited at different Cr power to vary the concentration by keeping all other sputtering parameters as constant. The details of the growth parameters are given at section 2.3.3.

The GIXRD profiles of reactive magnetron sputtered  $Al_{1-x}Cr_xN$  thin films with different Cr concentrations ( $x = 0, 2, 4$  and  $6$  at%) are shown in Fig. 5.1. The GIXRD patterns of these films exhibited poly-crystalline hexagonal wurtzite structure and agree with the JCPDS data 25-1133. Doped Cr atoms are well dissolved in the AlN and can be ascer-

tained by the absence of peaks corresponding to Cr, CrN,  $Cr_2N$  or  $Cr_2O_3$ . It is observed that these films are also preferentially  $a$ -axis oriented.

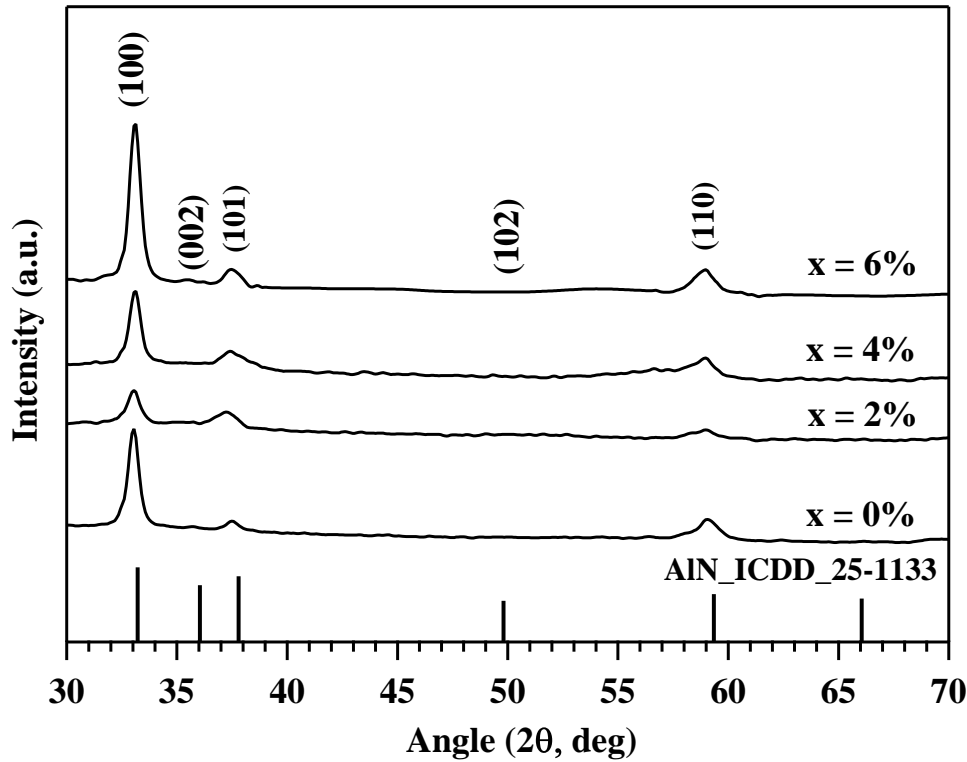


**Figure 5.1** – GIXRD profiles of  $Al_{1-x}Cr_xN$  thin films with  $x = 0, 2, 4$  and  $6$  at%

It can also be seen from Fig. 5.1 that there is a shift in the peak position towards lower  $2\theta$  values as compared to the standard data. This is due to the presence of tensile stress in the films. Hence, to delineate the effect of microstrain and crystallite size on the peak broadening, Williamson-Hall (W-H) method has been used as described in section 4.2. A representative W-H analysis term  $\beta \cos \theta$  is plotted with respect to  $4 \sin \theta$  for  $Al_{1-x}Cr_xN$  films with  $x = 0$  and  $6$  at% in Fig. 5.2. The strain is extracted from the slope of the fit to the data, and the crystallite size is extracted from the y-intercept of the fit. The crystallite size and strain of  $Al_{1-x}Cr_xN$  films are shown in Table 5.1.



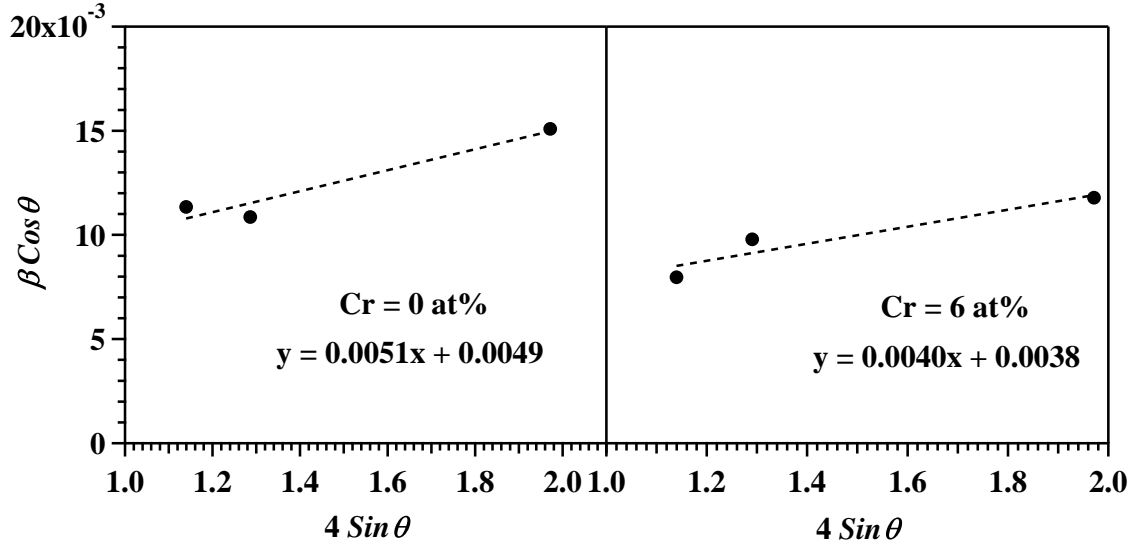


**Figure 5.2** – W-H plots of  $Al_{1-x}Cr_xN$  films with  $x = 0$  and 6 at%.

$x$ (at%)	$D$ (nm)	$\epsilon$ ( $10^{-3}$ )
0	29	5.1
2	19	5.4
4	24	5.2
6	37	4.0

**Table 5.1** – Crystallite size ( $D$ ) and strain ( $\epsilon$ ) of  $Al_{1-x}Cr_xN$  thin films with  $x = 0, 2, 4$  and 6 at%.

Pristine AlN ( $x = 0$  at%) grown at sputtering pressure  $5 \times 10^{-3}$  mbar has crystallite size around 29 nm with a tensile strain. Thereafter, Cr atoms are doped in AlN by the reactive co-sputtering technique that increases the sputtering pressure from 5 to  $7 \times 10^{-3}$  mbar as listed in section 2.3.3. Thus, sputtered atoms from the target undergoes many collisions to reach the substrate due to the decrease in the mean free path and reduces the ad-atom energy. So, the crystallite size is decreased with higher strain at  $x = 2$  at% compared to pristine AlN. Thereafter, the strain gradually decreases with addition of Cr to AlN lattice with increase in crystallite size. Luo *et al* has reported a similar trend in the stress of AlN films with the addition of Cr [81]. In this present study, all these films were grown with *a-axis* preferential orientation on Si (100) substrate, where there is a lattice mismatch always exists between AlN and the Si substrate. So, Cr doping in

the AlN lattices compensates for the lattice mismatch between the film and the substrate leading to decrease in strain with the increase of Cr concentration [81].

### 5.3 Surface chemical analysis

XPS is employed to investigate the existence of Cr and the binding energy of  $\text{Al}_{1-x}\text{Cr}_x\text{N}$  thin films. High-resolution spectra were obtained for all Cr concentrations after sputtering the surface for 10 minutes by 1 keV  $\text{Ar}^+$  ion beam. The Cr concentration of these films is calculated and found to be as 2, 4 and 6 at%. High resolution spectra of Al  $2p$ , N  $1s$  and Cr  $2p_{3/2}$ , are deconvoluted using the sum of Gaussian and Lorentz curves after the Shirley background subtraction and shown in Table 5.2.

x (%)	Al $2p$ (eV)		N $1s$ (eV)		Cr $2p_{3/2}$ (eV)
	Al-N	Al-O	Al-N	N-C	Cr-N
2	74.2	75.1	397.5	399.0	575.0
4	74.4	75.1	397.4	399.0	575.1
6	74.3	75.0	397.3	398.9	574.9
Ref. [137]	74.2	75	397.8	398.7	
Ref. [138]	74.1		397.2		574.9
Ref. [139]	73.5 - 74.7	74.7 - 75.6	396.8 - 397.9		
Ref. [152]					575.0

**Table 5.2** – Binding energy of different photoelectron peaks extracted from the  $\text{Al}_{1-x}\text{Cr}_x\text{N}$  thin films with references.

For discussion, a typical high-resolution XPS profile for Al  $2p$ , N  $1s$  and Cr  $2p$  corresponding to  $\text{Al}_{1-x}\text{Cr}_x\text{N}$  film with  $x = 6$  at% is shown in Fig. 5.3. Deconvoluted Al  $2p$  profile in Fig. 5.3(a) exhibits two sub-peaks where strong intensity one is found at 74.4 eV with an area 79% of the original peak. According to the literature, binding energy of Al-N is reported in the range of 73.5 to 74.7 eV [82, 137–139, 142]. However, the second peak with a binding energy of 75.1 eV corresponds to Al-O bond is observed, since

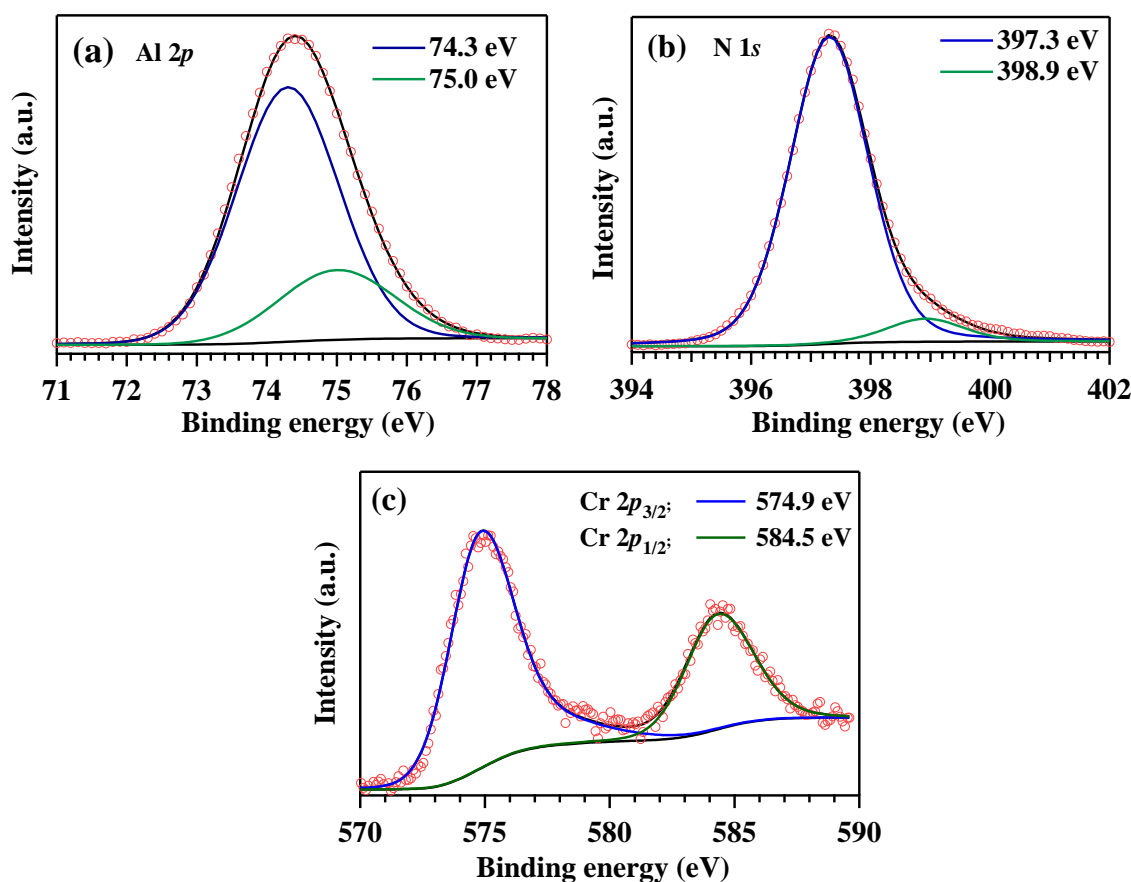


**Figure 5.3** – Core level XPS of (a) Al 2p, (b) N 1s and (c) Cr 2p for Al<sub>1-x</sub>Cr<sub>x</sub>N film with x = 6 at%.

Al has a significant chemical affinity to O. Thermodynamically Al-O interaction is more favourable compared to Al-N, as sputtering experiments are carried out at lower partial pressures (sum of Ar and N<sub>2</sub>). There is no evidence for Al-Al bonding or Al cluster formation, for which usually a peak is expected in the range between 72.2 to 72.8 eV [137]. Similarly, the N 1s profile has been deconvoluted and is shown in Fig. 5.3(b) with an intense peak corresponding to the binding energy 397.4 eV with 93% of an area which is assigned to Al-N. Recent reports on the binding energy of N 1s also confirms the same [82, 138, 142]. A second peak corresponding to a binding energy 399 eV is assigned to N-C bond in the form of triple (nitrile) and / or double (imine) bonds [137, 143]. Also, Cr XPS profile has fitted with the asymmetric Doniach-Sunjic parameter and is shown in

Fig. 5.3(c). The peaks corresponding to 575.1 and 584.6 eV are assigned to Cr-N bond of  $2p_{3/2}$  and  $2p_{1/2}$  core level of Cr. This binding energy is also well within the reported values [81, 138, 152]. This binding energy is clearly different from the Cr-Cr formation energy of 574 eV.

## 5.4 Morphology and surface roughness by AFM

Fig.5.4 consists of AFM images over  $1 \times 1 \mu m^2$  surface area of  $Al_{1-x}Cr_xN$  films deposited on Si (100) substrate having Cr concentration as  $x = 0$  and 6 at%.

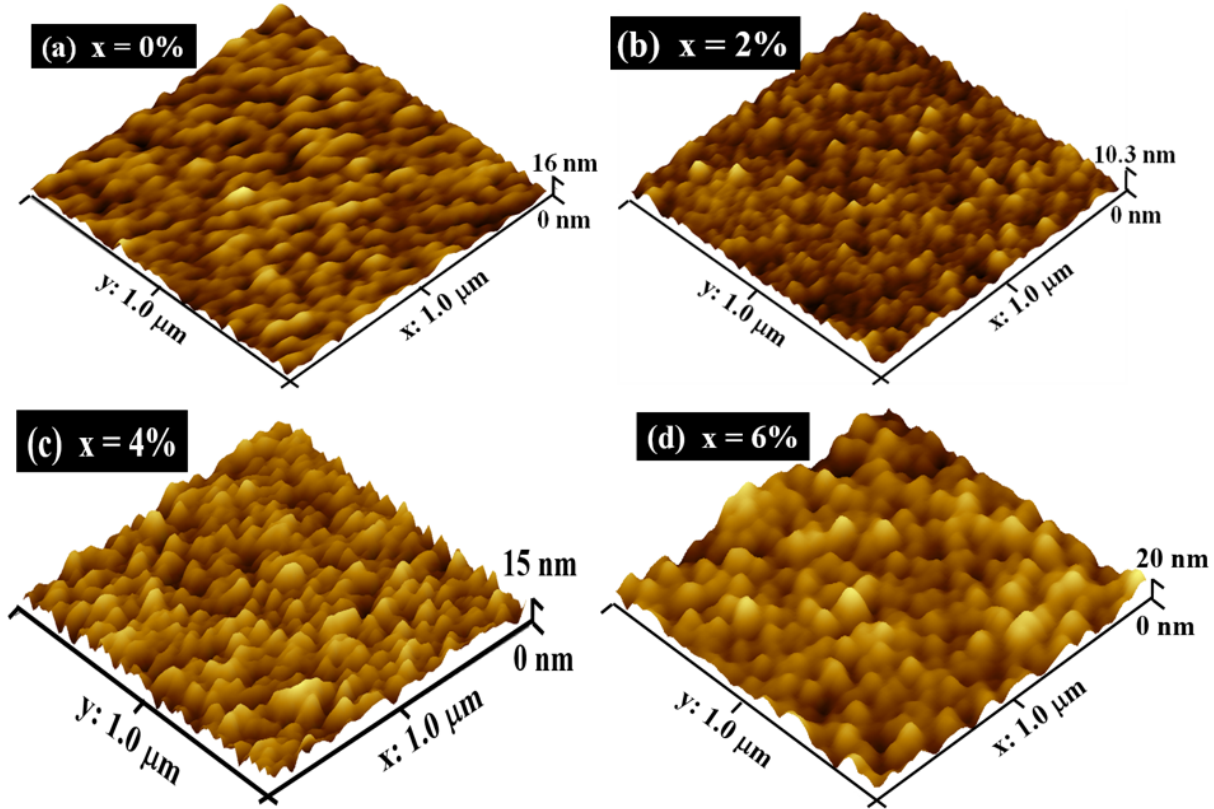


**Figure 5.4** – AFM images of  $Al_{1-x}Cr_xN$  films at Cr concentration of (a) $x = 0$ , (b) $x = 2$ , (c) $x = 4$ , and (d) $x = 6$  at%.

All these films exhibit a similar morphology with smooth pebble-like grain structure. The root mean square roughness ( $R_{rms}$ ) and the mean diameter of grains with the Cr concentration is extracted from AFM is shown in Table 5.3. For pristine AlN film, the

x (at%)	$R_{rms}$ (nm)	Grain size (nm)
0	2.6	35
2	1.3	22
4	3.3	33
6	4.0	46

**Table 5.3** –  $R_{rms}$  and average grain size of  $\text{Al}_{1-x}\text{Cr}_x\text{N}$  films with different Cr concentration.

surface consists of uniform smooth grains having roughness and grain size as 2.6 nm and 35 nm, respectively. However, both the roughness and grain size decreased with the addition of Cr atom (2%) and then significantly increased up to 6% of Cr atom. This can be compared from Table 5.1 that the roughness and grain size shows a similar behavior with crystallite size as observed from XRD. The surface of the film becomes coarser due to crystal growth that increases surface roughness. Since, the surface roughness of these  $\text{Al}_{1-x}\text{Cr}_x\text{N}$  films is very low, these films can be used for surface acoustic wave device applications.

## 5.5 Local crystal structure at vicinity of Cr in AlN:

### XAS

#### 5.5.1 XANES analysis

Cr K-edge absorption spectra of  $\text{Al}_{1-x}\text{Cr}_x\text{N}$  films are shown in Fig. 5.5 to investigate the local structure of the Cr dopant in the AlN lattice. From Fig. 5.5, a pre-edge peak is observed at around 5989 eV in all the Cr K-edge absorption spectra. Similar pre-edge peak in the XANES of Cr doped AlN films is reported as 5988.7 eV and 5989 eV by Fan *et al* in Cr doped AlN and Hashimoto *et al* in Cr doped GaN, respectively [68, 147]. They have shown that when Cr is introduced to the host matrix of AlN and GaN, Cr replaces the cation and forms localized CrN species. This is in concurrence with the observed

pre-edge peak in this study also [153]. Hence, it is concluded that when Cr is doped in AlN using the experimental methods described in this study led to the formation of localized CrN species in AlN. However, XAS is a localized technique, used to identify the ambiguity arising out of other local species of Cr with Oxygen. Usually, the pre-edge peak corresponding to  $\text{CrO}_2$  and  $\text{CrO}_3$  appears at 5979.6 eV and 5981.4 eV, respectively [154]. Also, the absorption spectrum of  $\text{Cr}_2\text{O}_3$  is similar to the  $\text{CrO}_2$ . These pre-edge peaks are distinctly different from the pre-edge peak observed in our study, which is around 5989 eV. Hence, it is concluded that there are no secondary oxide phases corresponding to Cr in these thin films.

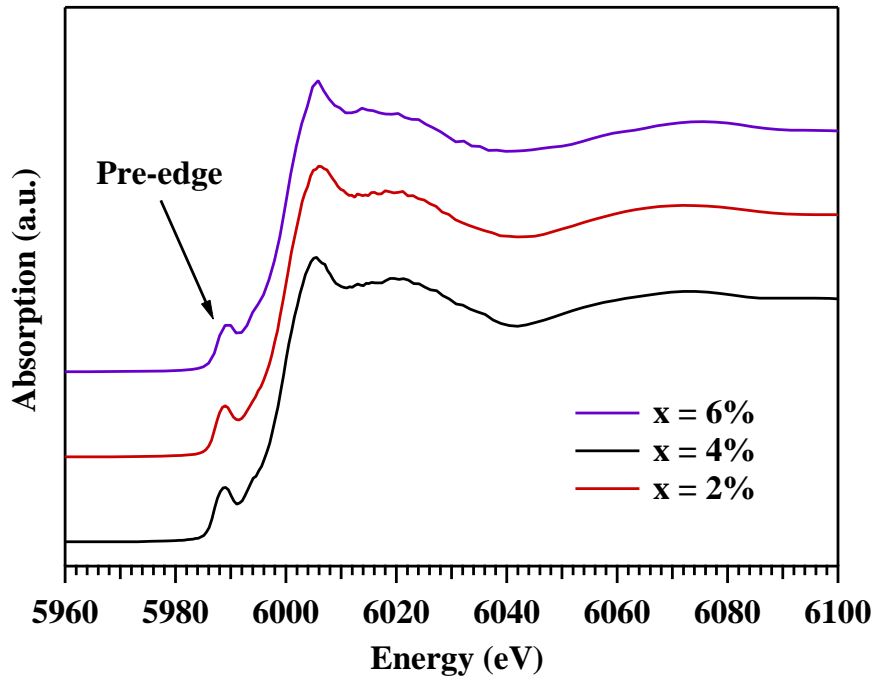


**Figure 5.5** – Cr K-edge absorption spectra of  $\text{Al}_{1-x}\text{Cr}_x\text{N}$  films.

Normally, the pre-edge peaks of transition metal elements in XAS spectrum are the signature of  $1s$  to  $3d$  electronic transitions [146, 147]. It is discussed in section 4.5.1 that  $1s$  to  $3d$  electronic transitions is generally forbidden for centro-symmetric compounds and can be possible to some extent in non-centro symmetric distorted tetrahedron com-

pounds [81, 136, 146, 147]. Since, AlN has a distorted tetrahedron structure, it is to note that this pre-edge peak at 5989 eV is solely from the localized distorted tetrahedron TiN species in AlN films. In addition to that this transition is also due to the presence of  $p-d$  hybridization between Cr and its neighbouring N atoms that led to the breakdown of the selection rule and  $p-d$  orbital mixing becomes feasible [81, 147]. Since, we have already confirmed that Cr replaces Al in AlN matrix, then Cr also has  $p-d$  mixing.

x (at%)	Energy (eV)	Intensity
1.5	$5989.0 \pm 0.2$	0.23
3	$5989.0 \pm 0.2$	0.19
4	$5989.5 \pm 0.2$	0.17

**Table 5.4** – Pre-edge peak of  $\text{Al}_{1-x}\text{Cr}_x\text{N}$  films in Cr K-edge absorption spectra.

The pre-edge peak positions and intensity of  $\text{Al}_{1-x}\text{Cr}_x\text{N}$  films are shown in Table 5.4. It is observed that the position of pre-edge peak is moving towards higher energy at high Cr concentration. Also, the intensity of the pre-edge peaks decreases with the increase of Cr in these films. At lower Cr concentrations, strain in these films is highly deforming the tetrahedron surroundings of Cr as well as the symmetry of the structure [68, 81]. It is observed that the strain decreases with the increase of Cr concentration that has been extracted using W-H method is shown in Table 5.1. In other words, the pre-edge peak intensity will be maximum for the films with lower Cr concentration, which is the case in the present study. Hence it can be concluded that  $1s-3d$  transition strength is higher when Cr concentration is low. Since, the  $\text{Cr}^{3+}$  ionic radius ( $0.63 \text{ \AA}$ ) is smaller than that of  $\text{Ti}^{3+}$  ( $0.68 \text{ \AA}$ ), the distorted tetrahedron structure of AlN is deformed less compared to Ti when it is doped with Cr. So, the magnitude of intensities of Cr K-edge are lower compared to pre-edge peak intensities of Ti K-edge as shown in section 4.5.1.

### 5.5.2 EXAFS analysis

For the EXAFS, oscillation part of the measured absorption co-efficient ( $\mu(E)$ ) is converted to the fine structure function  $\chi(E)$  as described in section 2.5. Finally,  $\chi(R)$  versus radial distances ( $R$ ) plots are used to extract the co-ordination number, radial distances and neighbouring atoms of the dopant in different co-ordination spheres. Wurtzite hexagonal AlN phase has been used as crystallographic inputs for the fitting of these spectra.

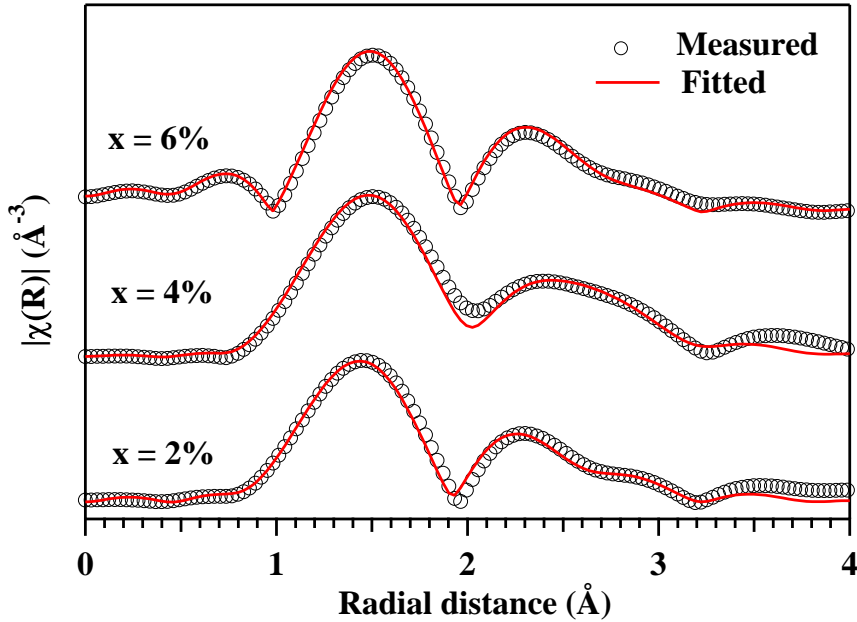


**Figure 5.6** – Extended region fitting using ARTEMIS in R-space of  $\text{Al}_{1-x}\text{Cr}_x\text{N}$  thin films.

Three paths corresponding to three basal nitrogen  $[(\text{Cr-N})_{bs}]$  and one path corresponding to the axial nitrogen  $[(\text{Cr-N})_{ax}]$  from the first co-ordination sphere and one path from the second co-ordination sphere (Cr-Al) are considered for the fitting of  $\text{Al}_{1-x}\text{Cr}_x\text{N}$  film spectra. Since the ranks of multiple scattering paths are very low, only the single scattering paths are included in the analysis. The overall value of R-factor is then minimized to establish the goodness of fit. The fitted EXAFS oscillation  $\chi(k)$  curves in R-space are shown in Fig. 5.6. The bond lengths of Cr-N and Cr-Al paths as well as the corresponding



co-ordination numbers (C.N) of each path ( $NS_0^2$ ,  $N$ =degeneracy of path), Deby-waller factor ( $\sigma^2$ ) and R-factor, are observed from the EXAFS and are shown in Table 5.5.

### 5.5.2.1 Discussion on coordination number and bond length

The total coordination number (axial and basal) of Cr with N atom in the first coordination sphere of these  $\text{Al}_{1-x}\text{Cr}_x\text{N}$  films is around 2.91 (constant). For AlN, the stoichiometric coordination number of Al atom with N is 4 in the first coordination sphere. So Cr dopant in these films show non-stoichiometric coordination with N atom. Similarly, it is observed that the coordination number of Cr in second sphere with Al atom is 8.03, 8.25 and 8.44 for  $x = 2, 4$  and  $6 \text{ at}\%$ , which is also lower than the Al-Al in second coordination sphere ( $\sim 12$ ) in AlN lattice. Hence, the coordination number of Cr in AlN film shows a lower stoichiometry compared to Ti doped AlN thin films with more N and Al vacancies in first and second coordination sphere.

The  $(\text{Cr-N})_{ax}$  and  $(\text{Cr-N})_{bs}$  bond lengths variation as a function of Cr concentrations for the first coordination sphere in  $\text{Al}_{1-x}\text{Ti}_x\text{N}$  films are shown in Fig. 5.7. It is observed that both the bond lengths decrease gradually with the Cr concentration. However, it is known that  $\text{Cr}^{3+}$  ionic radius ( $0.63 \text{ \AA}$ ) is larger than the ionic radius of Al ( $0.51 \text{ \AA}$ ), it is expected that Cr-N bond length should increase with the Cr concentration [79]. However, due to the strong atomic attraction as well as magnetic coupling of Cr and N, it is expected that the lattice constant of the Cr doped AlN decreases with the increase of Cr concentration [79, 81]. According to charge density distribution theory, it is understood that in pristine AlN there is a small overlap between Al and N charge densities, which leads to ionic bonding. When Al is replaced by Cr atom, there is a large scale overlap compared to pristine AlN i.e. there is a strong  $p$ - $d$  hybridization between dopant and the host atoms,

Sample	Paths	Bond length (Error)(Å)	C.N (Error)	$\sigma^2$ (Å) <sup>2</sup> (Error)	R
x = 2%	(Cr-N) <sub>ax</sub>	2.041	0.70	0.0011	0.02
		(0.005)	(0.06)	(0.0001)	
	(Cr-N) <sub>bs</sub>	1.872	2.20	0.0202	
		(0.005)	(0.05)	(0.0003)	
	Cr-Al	3.135	8.03	0.0250	
		(0.006)	(0.08)	(0.0003)	
x = 4%	(Cr-N) <sub>ax</sub>	1.994	0.70	0.0011	0.03
		(0.005)	(0.09)	(0.0005)	
	(Cr-N) <sub>bs</sub>	1.845	2.21	0.0182	
		(0.005)	(0.08)	(0.0007)	
	Cr-Al	3.163	8.25	0.0220	
		(0.009)	(0.11)	(0.0002)	
x = 6%	(Cr-N) <sub>ax</sub>	1.982	0.72	0.0010	0.01
		(0.003)	(0.06)	(0.0001)	
	(Cr-N) <sub>bs</sub>	1.813	2.22	0.0172	
		(0.003)	(0.03)	(0.0004)	
	Cr-Al	3.151	8.44	0.0220	
		(0.005)	(0.08)	(0.0003)	

**Table 5.5** – Fitted path parameters for the Al<sub>1-x</sub>Cr<sub>x</sub>N thin films

which causes the reduction in bond length [155]. Saeed *et al* [156] have also reported that the bond lengths of Cr-N and Cr-Al decreases with increase in Cr concentration, explained by Murnaghan's equation of state. Also, it is seen from XRD that the strain (tensile) decreases with increasing Cr concentration, this in turn reduces the bond length.

### 5.5.2.2 Discussion on Cr cluster formation

As we know, EXAFS is highly sensitive to the local co-ordination and bond length of neighbouring atoms. It provides information about the dopant position and the bond lengths of the dopant (absorber) with its nearest neighbors. In addition to this, EXAFS study also helps in identifying the nature of Cr bonding in AlN matrix. In particular, in the present study, it helps to remove the ambiguity regarding the Cr cluster formation. From Table 5.5, it can be observed that Cr-Al bond length is around 3.15 Å, which is similar to Al-Al bond length, in AlN system. Emura *et al* [157] reported a bond length

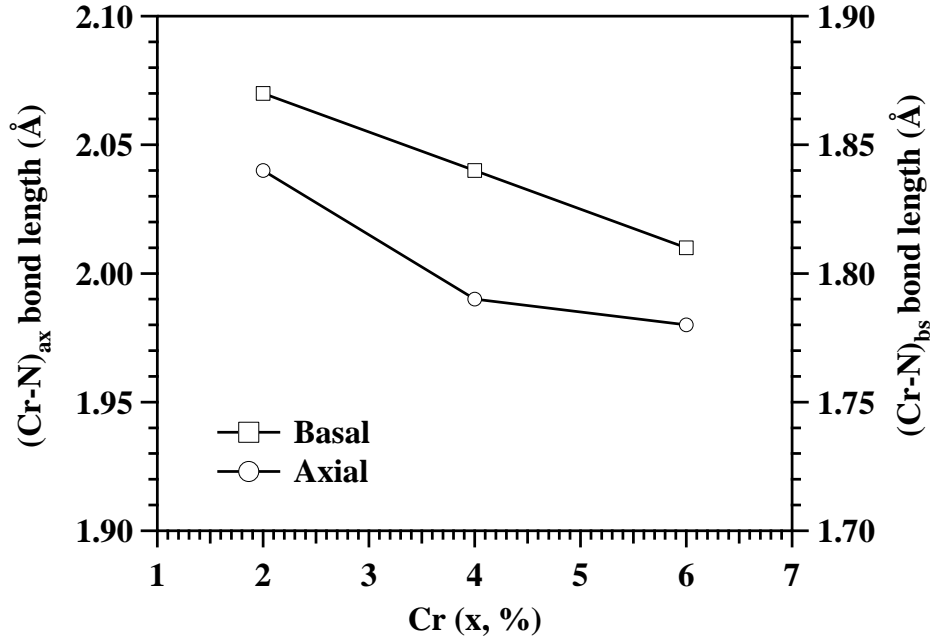


**Figure 5.7** –  $(\text{Cr-N})_{ax}$  and  $(\text{Cr-N})_{bs}$  bond length are plotted as the function of Cr concentration.

of 3.11 Å for Cr-Al in substitutionally Cr doped AlN films by plasma-assisted molecular beam epitaxy method on  $\text{Al}_2\text{O}_3$  (0001) substrate. Cui *et al* [79] reported the nearest neighbour Cr-Cr bond length of 2.49 Å in bulk bcc Cr. Whereas they calculated the bond length of Al-N and Al-Al as 1.90 and 3.14 Å, respectively in bulk AlN using DFT. So, in this study EXAFS confirms that there is no Cr clustering in these films. However, Cr substitutes the cation (Al) of few AlN tetrahedrons in these AlN matrices. This result corroborates with the observation of XANES studies described above, wherein we have elucidated that when Cr forms localised CrN species rather than Cr clusters.

## 5.6 Mechanical properties

Nanomechanical characterization is performed by nano-indentation technique to understand the deformation behavior of AlN film with the addition of Cr for the design of opto-electronic devices. Nano-indentation is performed on  $\text{Al}_{1-x}\text{Cr}_x\text{N}$  films as a function of depth (20 nm to 650 nm) at different linear load. The indentation hardness ( $H$ ) and

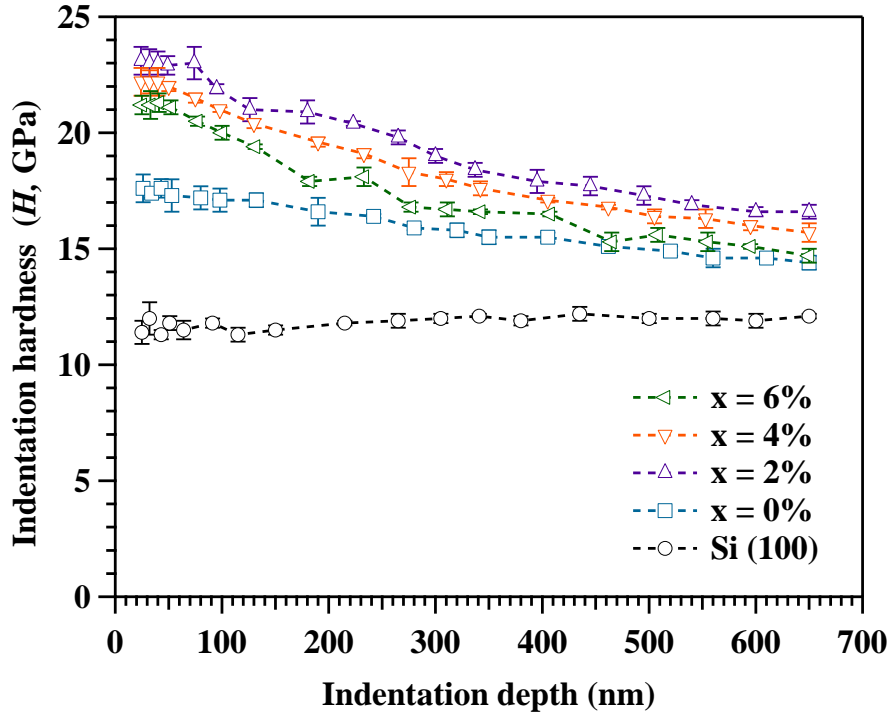


**Figure 5.8** – Indentation hardness as a function of depth of Si (100) substrate and  $\text{Al}_{1-x}\text{Cr}_x\text{N}$  films with  $x = 0$  to 6 at%.

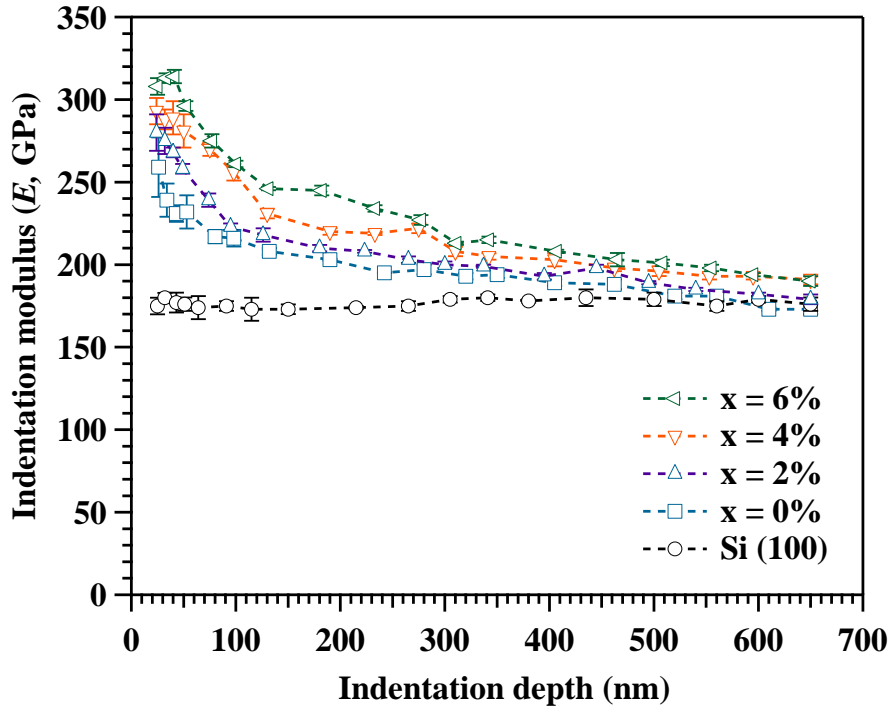


**Figure 5.9** – Indentation modulus as a function of depth of Si (100) substrate and  $\text{Al}_{1-x}\text{Cr}_x\text{N}$  films with  $x = 0$  to 6 at%.

modulus ( $E$ ) of Si (100) substrate and  $\text{Al}_{1-x}\text{Cr}_x\text{N}$  films with  $x = 0$  to 6 at% are shown in Fig. 5.8 and Fig. 5.9, respectively. It is observed that  $H$  and  $E$  of Si are almost constant throughout the depth at around 11.5 and 175 GPa, respectively. However, the  $H$  of  $\text{Al}_{1-x}\text{Cr}_x\text{N}$  films show a steady value up to 50 nm and thereafter decreases with the indentation depth due to the substrate effect. It is well known that the indentation should be performed within the one-tenth ( $1/10^{\text{th}}$ ) thickness of the film to determine the film hardness to avoid the substrate effect [150]. In this study, the film thickness is around 450 nm and the hardness at or below 50 nm are constant and then decreases to reach the composite hardness, which follows the  $1/10^{\text{th}}$  rule. Similarly, the indentation modulus value also decreases with depth as similar an exponential function and reach the value of substrate at 650 nm depth. The mechanical parameters have extracted at a depth of 35 nm from the indentation experiment and are plotted in Fig. 5.10.

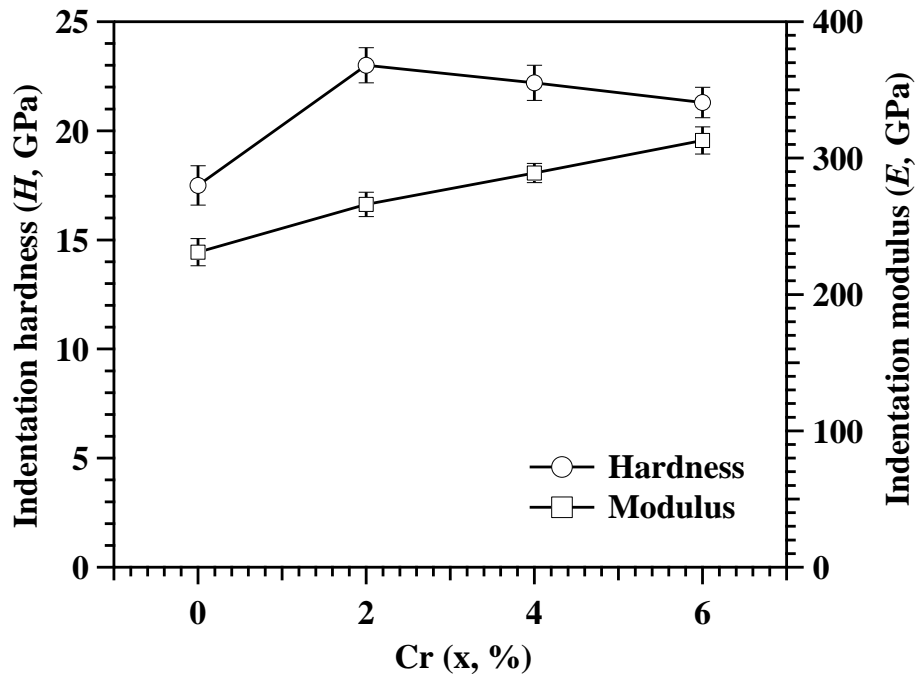


**Figure 5.10** – Indentation hardness and modulus of  $\text{Al}_{1-x}\text{Cr}_x\text{N}$  films with Cr concentration.

In Fig. 5.10, it is seen that the hardness value is 17.5 GPa for pristine AlN film. Whereas with the addition of 2% Cr atom to AlN film, the hardness value shows as 23 GPa. There after with increase in Cr, hardness exhibits a constant drop to 21.3 GPa for  $x = 6 \text{ at\%}$ . Normally, improvement in mechanical properties occurs due to the collective contribution of the film micro-structure *i.e.* crystallite size of material, plane orientation, planar density, bond strength and induced stress during the growth of films. It can be seen from Table 5.1 that the  $\text{Al}_{1-x}\text{Cr}_x\text{N}$  film at  $x = 2\%$  contains high intrinsic strain among all these films. Apart from this, the ionic radius of Cr is larger than the Al. In the doping process, Cr substitutes Al atom and forms local CrN species that increases the density of AlN lattice structure. It is also reported that the hardness of CrN film is around 25 GPa [150]. Therefore, this film shows higher hardness compared to pristine AlN films. However, the lattice strain decreases with Cr concentration as well as the crystallite size increases (Hall-Petch relation), which can be seen in XRD (Fig. 5.1) and AFM (Table 5.3). So, the hardness decreases due to the stress relaxation and grain growth.

Cr doped AlN films exhibited lower hardness compared to Ti doped AlN films. From XAS study, it can be understood that Cr forms localized CrN species with distorted tetrahedron structure and this deformation (distorted) is smaller than the Ti doped AlN. Also, the coordination number of Cr in  $\text{Al}_{1-x}\text{Cr}_x\text{N}$  films shows a lower stoichiometric compared to the coordination number of Ti in  $\text{Al}_{1-x}\text{Ti}_x\text{N}$  films having more N and Al vacancies in first and second coordination sphere. Additionally, Ti doped AlN films are found to be polycrystalline whereas, Cr doped AlN films are found to be crystallizing with a preferential *a-axis* direction. The hardness of highly *a-axis* oriented AlN film is found to be 16.4 GPa as shown in Fig. 3.7. Because of these reasons, Cr doped AlN films exhibit low hardness compared to Ti doped AlN films.

Moreover, nanoindentation modulus ( $E$ ) of  $\text{Al}_{1-x}\text{Cr}_x\text{N}$  films is gradually increased with Cr concentration *i.e.* from 231 to 313 GPa for  $x = 0$  to 6%, respectively in Fig. 5.10. Predominantly, modulus of a material depends on the nature of the inter-atomic bond strength. It is also perceived that Cr replaces substitutionally with Al atom in AlN crystal and the bond lengths belong to first and second co-ordination sphere decreases rapidly with Cr concentration due to the augmentation of strong  $p$ - $d$  hybridization between the Cr and N atom. Therefore, covalent bond strength increases in AlN lattice that enhances the modulus of the films. Thus, addition of Cr to AlN lattice exhibits high elastic in nature compared to Ti doped AlN films [158].

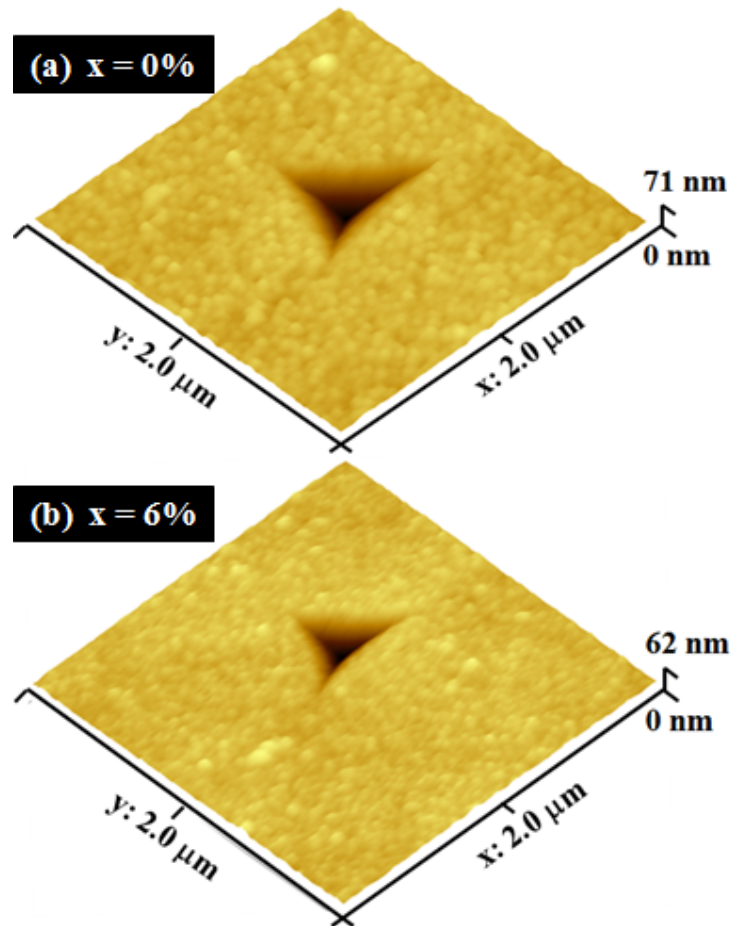


**Figure 5.11** – AFM images of the indentation impressions at a peak load of 2 mN of  $\text{Al}_{1-x}\text{Cr}_x\text{N}$  films with  $x = 0$  and 6 at%.

The plastic deformation of these films during indentation can be explored from the topography images of the indentation impression by observing the pile-up or sink-in behavior [151]. The typical AFM images of the indentation impressions at a peak load of 2 mN over  $2 \times 2 \mu m^2$  surface area of  $Al_{1-x}Cr_xN$  films with  $x = 0$  and 6 at% are shown in Fig. 5.11. Indentation impression of all these films exhibits a well-defined sink-in behavior which is caused by the Berkovich indenter. It is evident that  $Al_{1-x}Cr_xN$  films have high elastic recovery *i.e.* high resistance to plastic deformation after the indentation without any radial cracks.

## 5.7 Conclusion

Cr doped AlN thin films are grown using reactive magnetron co-sputtering with different Cr concentrations (0, 2, 4 and 6 at%). Surface chemical analysis and Cr concentration of these films are studied by the XPS. All these films are found to be crystallizing along *a-axis* direction with wurtzite structure of AlN without any secondary phases belongs to Cr compound. The crystallite size of these films increases with Cr concentration. The surface morphology, roughness and average grain size are also affected by the Cr dopant in AlN films. The local crystal structure around the Cr dopant in  $Al_{1-x}Cr_xN$  films are analyzed by both XANES and EXAFS. It is observed that Cr replaces the Al atom in AlN lattice and forms localized distorted tetrahedron CrN species. The total coordination number (axial and basal) of Cr with N atom in the first coordination sphere is around 2.91 (constant), whereas for second sphere with Al atom is 8.03, 8.25 and 8.44 for  $x = 2, 4$  and 6 at%. So, Cr dopant in these films shows non-stoichiometric coordination compared to pristine AlN lattice with both N and Al vacancies in the first and second coordination sphere, respectively. The bond lengths  $(Cr-N)_{ax}$ ,  $(Cr-N)_{bs}$  and Cr-Al, extracted from the EXAFS fitting are found to be decreasing rapidly with Cr concentration and shows a strong *p-d* hybridization between dopant and host atoms compared to Ti doped AlN



films. Therefore, the modulus enhanced from 231 to 313 GPa with the increase in Cr concentration. The hardness of  $\text{Al}_{1-x}\text{Cr}_x\text{N}$  films is varying between 17.5 to 23 GPa with the increase of Cr. These Cr doped AlN films show a lower hardness compared to Ti doped AlN due to more Al and N vacancies and large crystallite size. Indentation impression of these films exhibits a well-defined sink-in behavior and gives an evidence of high elastic recovery without any radial cracks.

# Chapter 6

## Summary and future directions

### 6.1 Summary

The main focus of this thesis is to grow *a*-axis oriented AlN films to study the crystal structure, mechanical and optical properties. Additionally, this thesis also focuses on the growth of transition metal (Ti and Cr) doped AlN films and study of local crystal structure as well as mechanical behavior with different doping concentrations. The results obtained in this thesis are expected to have relevance in realizing for fundamental applications and device fabrications in deep-UV opto-electronics.

The growth of AlN thin films using reactive magnetron sputtering at different growth temperatures ( $T_s$ , 35 to 600 °C) have discussed. All these films are crystallized with wurtzite structure and the  $T_s$  influences the orientation of these films. The crystallinity is increased with  $T_s$  and a preferential *a*-axis orientation is observed at 400 °C with high degree of columnar structure. The surface morphology, RMS roughness and average grain size are also strongly influenced by the  $T_s$ . However, the residual stress measurement by  $\sin^2\psi$  technique exhibits a transition from tensile to compressive between 200 to 400 °C growth temperature. Nano-indentation hardness studies on these films revealed that the indentation hardness ( $H$ ) varied between 13.0 to 18.5 GPa, whereas at 400 °C AlN film

exhibited a relatively high elastic modulus ( $E = 238$  GPa) due to the  $B_1$  type of bonding which is more covalent in nature. Uniaxial anisotropic optical properties of these films with different  $T_s$  are investigated by SE technique, which is strongly depend on  $T_s$ . Highly *a-axis* oriented AlN film grown at  $400^\circ\text{C}$ , exhibited high  $n$  ( $n_\perp = 2.55$ ,  $n_\parallel = 2.57$ ) and low  $k$  ( $k_\perp = 0.21$ ,  $k_\parallel = 0.25$ ) at  $210$  nm (deep-UV region) with low value of  $\Delta n$  ( $-0.01$ ) and  $\Delta k$  ( $0.03$ ). It is observed that the birefringence ( $\Delta n = -0.01$ ) of *a-axis* oriented AlN film is relatively lower compared to the *c-axis* oriented AlN film ( $\Delta n = -0.05$  at  $210$  nm) reported in the literature so far. With the increase in  $T_s$  the band gap increased upto  $400^\circ\text{C}$ , which is close to the bulk AlN. So, the anisotropy optical properties of *a-axis* AlN can be effectively used in UV-LED and electro-luminescent diode based polarization sensitive optoelectronic applications.

Similarly, the Ti and Cr doped AlN ( $\text{Al}_{1-x}\text{Ti}_x\text{N}$  and  $\text{Al}_{1-x}\text{Cr}_x\text{N}$ ) films are grown by reactive magnetron co-sputtering technique with different Ti ( $x = 0, 1.5, 3$  and  $4$  at%) and Cr concentrations ( $x = 0, 2, 4$  and  $6$  at%). All these films are found to be polycrystalline wurtzite hexagonal of AlN without any other secondary phases belonging to Ti and Cr compounds. However, Cr doped AlN films are found to be crystallizing along *a-axis* direction as compared to Ti doped AlN films. The surface chemical analysis, doping concentration and surface morphology of these films are studied by XPS and AFM technique. All these films have exhibited an intrinsic tensile residual strain. The tensile strain increases with the Ti concentration in  $\text{Al}_{1-x}\text{Ti}_x\text{N}$  films, whereas it decreases with Cr concentration in  $\text{Al}_{1-x}\text{Cr}_x\text{N}$  films. The local crystal structure around Ti and Cr dopant in  $\text{Al}_{1-x}\text{Ti}_x\text{N}$  and  $\text{Al}_{1-x}\text{Cr}_x\text{N}$  films, respectively are analyzed by both XANES and EXAFS. Both the cases, it is observed that Ti and Cr forms localized nitride species with distorted tetrahedron structure by replacing the Al atom in AlN lattice. The coordination number of Ti in first sphere shows stoichiometric with N atom, whereas Al

vacancies are found in second coordination sphere. The bond lengths  $(\text{Ti-N})_{ax}$ ,  $(\text{Ti-N})_{bs}$  are found to be moderately decreased with Ti concentration, whereas Ti-Al bond length in second coordination sphere is independent of Ti. Thus, XAS measurement confirms the enhancement of  $p-d$  hybridization between Ti and N atoms in  $\text{Al}_{1-x}\text{Ti}_x\text{N}$  thin films. Similarly, the bond lengths  $(\text{Cr-N})_{ax}$ ,  $(\text{Cr-N})_{bs}$  and Cr-Al, extracted from the EXAFS fitting are found to be decreased rapidly compared to  $\text{Al}_{1-x}\text{Ti}_x\text{N}$  films with Cr due to the strong atomic attraction as well as magnetic coupling between dopant and host atoms that shows a strong  $p-d$  hybridization between Cr and N. The indentation hardness ( $H$ ) and modulus ( $E$ ) of  $\text{Al}_{1-x}\text{Ti}_x\text{N}$  films are increased from 17.5 to 27.6 GPa and 231 to 293 GPa, respectively with  $x = 0$  to 4 at%. The  $H$  of  $\text{Al}_{1-x}\text{Cr}_x\text{N}$  films is varied between 17.5 to 23 GPa. Whereas,  $E$  is enhanced with Cr concentration from 231 to 313 GPa for  $x = 0$  to 6% due to strong  $p-d$  hybridization between the Cr and N atom. Indentation impression of these films exhibits a well-defined sink-in behavior and gives an evidence of high elastic recovery without any radial cracks.

## 6.2 Future directions

Though AlN is embedded with many versatile properties, a growth of doped  $a$ -axis oriented epitaxial AlN films is a most challenging task. To make use of its practical applications, understanding and exploring the proper growth condition is therefore very necessary. In addition to the exotic optical and mechanical properties, AlN also has a high thermal conductivity. It is therefore important to study the thermal conductivity properties of doped epitaxial AlN films for IC packaging in optoelectronics and thermal/environmental barrier coating applications. Transition metal doped group III nitrides have attracted considerable attention in spin-dependent photonic and electronic devices due to their intrinsic ferromagnetic with semiconducting properties. Therefore, doped AlN film requires a investigation in both local and bulk magnetization proper-

ties. Apart from this, heavily doped wide band gap materials are expected to be used in photovoltaic conversion applications, intermediate band solar cell and photo-electrodes semiconductor for artificial photosynthesis. Thus doping and tailoring of AlN films particularly with transition elements such as p-type (Mg, Be, C etc) and n-type (Si, Cr, Ti, V, Co etc) will provide wide opportunity in the area of future cutting edge science and industry.

So, it is important to develop various concentrations of p-type (Mg, Be, C etc) and n-type (Si, Cr, Ti, V, Co etc) doped epitaxial AlN films using various deposition techniques for the tailoring of structural, optical, thermal and electrical properties as elaborated below;

1. Optimization of p-type and n-type AlN growth in order to obtain high quality epitaxial film as well as smooth surface morphologies.
2. Investigation of the crystal orientation and epitaxial nature of these films and optimization of the growth process for improved physical properties.
3. Investigation of the optical and electrical properties of these epitaxial layers in order to find the best efficient p and n-type doping elements.
4. Investigation on improvement of thermal conductivity and nano-mechanical properties with different doping elements to AlN to find out the future hard materials for optoelectronic applications.

# References

- [1] H. Morkoc, *Handbook of Nitride Semiconductors and Devices. Vol.1: Materials Properties, Physics and Growth*, WILEY-VCH, Weinheim, 2008.
- [2] T. S. Pan, Y. Zhang, J. Huang, B. Zeng, D. H. Hong, S. L. Wang, H. Z. Zeng, M. Gao, W. Huang and Y. Lin, *Journal of Applied Physics*, 2012, **112**, 044905.
- [3] T. Hanada, *Basic properties of ZnO, GaN, and related materials*, Springer, 2009, pp. 1–19.
- [4] W. Martienssen and H. Warlimont, *Springer handbook of condensed matter and materials data*, Springer Science & Business Media, 2006.
- [5] P. Y. Yu and M. Cardona, *Fundamentals of semiconductors: physics and materials properties*, Springer, 1996.
- [6] F. Litimein, B. Bouhafs, Z. Dridi and P. Ruterana, *New Journal of Physics*, 2002, **4**, 64.
- [7] W.-T. Lin, L.-C. Meng, G.-J. Chen and H.-S. Liu, *Applied physics letters*, 1995, **66**, 2066–2068.
- [8] T. Schupp, K. Lischka and D. As, *Journal of Crystal Growth*, 2010, **312**, 1500–1504.
- [9] M. Bartosik, M. Todt, D. Holec, J. Todt, L. Zhou, H. Riedl, H. Böhm, F. Rammerstorfer and P. Mayrhofer, *Applied Physics Letters*, 2015, **107**, 071602.

- [10] D. Holec and P. H. Mayrhofer, *Scripta materialia*, 2012, **67**, 760–762.
- [11] R. Rodriguez-Clemente, B. Aspar, N. Azema, B. Armas, C. Combescure, J. Durand and A. Figueras, *Journal of crystal growth*, 1993, **133**, 59–70.
- [12] X.-H. Xu, H.-S. Wu, C.-J. Zhang and Z.-H. Jin, *Thin Solid Films*, 2001, **388**, 62 – 67.
- [13] F. Medjani, R. Sanjines, G. Allidi and A. Karimi, *Thin Solid Films*, 2006, **515**, 260 – 265.
- [14] H. M. and J. S., *Metall. Trans. A*, 1992, **23**, 3141–3149.
- [15] H. A. Barkad, A. Soltani, M. Mattalah, J.-C. Gerbedoen, M. Rousseau, J.-C. D. Jaeger, A. BenMoussa, V. Mortet, K. Haenen, B. Benbakhti, M. Moreau, R. Dupuis and A. Ougazzaden, *Journal of Physics D: Applied Physics*, 2010, **43**, 465104.
- [16] Y. Xu, M. Goto, R. Kato, Y. Tanaka and Y. Kagawa, *Journal of Applied Physics*, 2012, **111**, 084320.
- [17] M. D. Brubaker, I. Levin, A. V. Davydov, D. M. Rourke, N. A. Sanford, V. M. Bright and K. A. Bertness, *Journal of Applied Physics*, 2011, **110**, 053506.
- [18] T. Kamohara, M. Akiyama and N. Kuwano, *Applied Physics Letters*, 2008, **92**, 093506.
- [19] F. Jose, R. Ramaseshan, S. Tripura Sundari, S. Dash, A. K. Tyagi, M. S. R. N. Kiran and U. Ramamurty, *Applied Physics Letters*, 2012, **101**, 254102.
- [20] M. Clement, L. Vergara, J. Sangrador, E. Iborra and A. Sanz-Hervás, *Ultrasonics*, 2004, **42**, 403–407.

- [21] T. Aubert, J. Bardong, O. Legrani, O. Elmazria, M. Badreddine Assouar, G. Bruckner and A. Talbi, *Journal of Applied Physics*, 2013, **114**, 014505.
- [22] S. Wu, R. Ro, Z.-X. Lin and M.-S. Lee, *Journal of Applied Physics*, 2008, **104**, 064919.
- [23] J. Rodríguez-Madrid, G. Iriarte, O. A. Williams and F. Calle, *Sensors and Actuators A: Physical*, 2013, **189**, 364–369.
- [24] L. Qian, C. Li, M. Li, F. Wang and B. Yang, *Applied Physics Letters*, 2014, **105**, 183501.
- [25] Y.-J. Hsiao, T.-H. Fang, Y.-H. Chang, Y.-S. Chang and S. Wu, *Materials Letters*, 2006, **60**, 1140–1143.
- [26] S. Fu, Q. Li, M. Wang, C. Song, F. Zeng and F. Pan, *Journal of Materials Science: Materials in Electronics*, 2018, **29**, 3912–3919.
- [27] Y. Taniyasu and M. Kasu, *NTT Tech. Rev*, 2010, **8**, 1–5.
- [28] Y. Taniyasu and M. Kasu, *Applied Physics Letters*, 2010, **96**, 221110.
- [29] Y. Taniyasu, M. Kasu and T. Makimoto, *Nature*, 2006, **441**, 325.
- [30] L. Chen, B. J. Skromme, R. F. Dalmau, R. Schlessner, Z. Sitar, C. Chen, W. Sun, J. Yang, M. A. Khan, M. L. Nakarmi, J. Y. Lin and H.-X. Jiang, *Applied Physics Letters*, 2004, **85**, 4334–4336.
- [31] E. Silveira, J. A. Freitas, O. J. Glembocki, G. A. Slack and L. J. Schowalter, *Phys. Rev. B*, 2005, **71**, 041201.
- [32] E. F. Schubert, *Light Emitting Diodes*, Cambridge University Press, 2nd edn., 2006.



- [33] I. Bryan, A. Rice, L. Hussey, Z. Bryan, M. Bobea, S. Mita, J. Xie, R. Kirste, R. Collazo and Z. Sitar, *Applied Physics Letters*, 2013, **102**, 061602.
- [34] A. Kakanakova-Georgieva, G. K. Gueorguiev, R. Yakimova and E. JanzÅ©n, *Journal of Applied Physics*, 2004, **96**, 5293–5297.
- [35] K. T., S. M., U. Y., K. J. F., S. R., O. T., N. S. and C. S. F., *physica status solidi (a)*, 2006, **203**, 1603–1606.
- [36] K. Okamoto, S. Inoue, T. Nakano, T.-W. Kim, M. Oshima and H. Fujioka, *Thin Solid Films*, 2008, **516**, 4809 – 4812.
- [37] H. Liu, G. Tang, F. Zeng and F. Pan, *Journal of Crystal Growth*, 2013, **363**, 80 – 85.
- [38] X.-P. Kuang, H.-Y. Zhang, G.-G. Wang, L. Cui, C. Zhu, L. Jin, R. Sun and J.-C. Han, *Superlattices and Microstructures*, 2012, **52**, 931 – 940.
- [39] C. Mirpuri, S. Xu, J. D. Long and K. Ostrikov, *Journal of Applied Physics*, 2007, **101**, 024312.
- [40] H. Cheng, Y. Sun, J. Zhang, Y. Zhang, S. Yuan and P. Hing, *Journal of crystal growth*, 2003, **254**, 46–54.
- [41] M. Ishihara, S. Li, H. Yumoto, K. Akashi and Y. Ide, *Thin Solid Films*, 1998, **316**, 152–157.
- [42] M. Ishihara, T. Nakamura, F. Kokai and Y. Koga, *Diamond and related materials*, 2002, **11**, 408–412.
- [43] Y. Chen, R. Wang, B. Wang, T. Xing, X. Song, M. Zhu and H. Yan, *Journal of crystal growth*, 2005, **283**, 315–319.

- [44] T. Liu, J. Zhang, X. Su, J. Huang, J. Wang and K. Xu, *Scientific reports*, 2016, **6**, 1–8.
- [45] W. Wang, W. Yang, Z. Liu, H. Wang, L. Wen and G. Li, *Scientific reports*, 2015, **5**, 11480.
- [46] A. Kale, R. Brusa and A. Miotello, *Applied Surface Science*, 2012, **258**, 3450–3454.
- [47] H.-G. Chen, S.-R. Jian, H.-L. Kao, M.-R. Chen and G.-Z. Huang, *Thin Solid Films*, 2011, **519**, 5090–5094.
- [48] H. Ohno, *Science*, 1998, **281**, 951–956.
- [49] V. I. Litvinov and V. K. Dugaev, *Phys. Rev. Lett.*, 2001, **86**, 5593–5596.
- [50] S. W. Fan, X. N. Huang and K. L. Yao, *Journal of Applied Physics*, 2017, **121**, 073905.
- [51] C. Zhou, A. Ghods, V. G. Saravade, P. V. Patel, K. L. Yunghans, C. Ferguson, Y. Feng, B. Kucukgok, N. Lu and I. T. Ferguson, *ECS Journal of Solid State Science and Technology*, 2017, **6**, Q149–Q156.
- [52] D. Kumar, J. Antifakos, M. G. Blamire and Z. H. Barber, *Applied Physics Letters*, 2004, **84**, 5004–5006.
- [53] S. G. Yang, A. B. Pakhomov, S. T. Hung and C. Y. Wong, *Applied Physics Letters*, 2002, **81**, 2418–2420.
- [54] K. Ueda, H. Tabata and T. Kawai, *Applied Physics Letters*, 2001, **79**, 988–990.
- [55] S. Ogale, R. Choudhary, J. Buban, S. Lofland, S. Shinde, S. Kale, V. Kulkarni, J. Higgins, C. Lanci, J. Simpson *et al.*, *Physical Review Letters*, 2003, **91**, 077205.

- [56] Y. Matsumoto, M. Murakami, T. Shono, T. Hasegawa, T. Fukumura, M. Kawasaki, P. Ahmet, T. Chikyow, S.-y. Koshihara and H. Koinuma, *Science*, 2001, **291**, 854–856.
- [57] Y. Muramoto, M. Kimura and S. Nouda, *Semiconductor Science and Technology*, 2014, **29**, 084004.
- [58] V. Chivukula, D. Ciplys, A. Sereika, M. Shur, J. Yang and R. Gaska, *Applied Physics Letters*, 2010, **96**, 163504.
- [59] T. Aoki, N. Fukuhara, T. Osada, H. Sazawa, M. Hata and T. Inoue, *Applied Physics Express*, 2014, **7**, 106502.
- [60] M. Alevli, C. Ozgit, I. Donmez and N. Biyikli, *Journal of Vacuum Science & Technology A*, 2012, **30**, 021506.
- [61] H. Y. Yang, S. F. Yu, J. I. Wong, Z. H. Cen, H. K. Liang and T. Chen, *ACS Appl. Mater. Interfaces*, 2011, **3**, 1726–1730.
- [62] J. Song, J. Zhou, W. Wang, Y. Liu, X. Li, X. Xu, X. An and E. Xie, *J. Phys. Chem. C*, 2010, **114**, 10761–10767.
- [63] T.-C. Liu, H. Kominami, H. F. Greer, W. Zhou, Y. Nakanishi and R.-S. Liu, *Chem. Mater.*, 2012, **24**, 3486–3492.
- [64] L.-J. Shi, L.-F. Zhu, Y.-H. Zhao and B.-G. Liu, *Phys. Rev. B*, 2008, **78**, 195206.
- [65] J. Zhang, X. Z. Li, B. Xu and D. J. Sellmyer, *Applied Physics Letters*, 2005, **86**, 212504.
- [66] A. Majid, M. Azmat, N. Ahmad, F. Hussain and G. Nabi, *Journal of Magnetism and Magnetic Materials*, 2017, **432**, 351 – 355.

- [67] V. V. Bannikov, A. R. Beketov, M. V. Baranov, A. A. Elagin, V. S. Kudyakova and R. A. Shishkin, *Physics of the Solid State*, 2016, **58**, 924–932.
- [68] B. Fan, F. Zeng, C. Chen, Y. C. Yang, P. Y. Yang and F. Pan, *Journal of Applied Physics*, 2009, **106**, 073907.
- [69] Y. Ren, D. Pan, J. Jian, X. Jiang, J. Li, Y. Sun and R. Wu, *Integrated Ferroelectrics*, 2013, **146**, 154–160.
- [70] F. Cai, M. Chen, M. Li and S. Zhang, *Ceramics International*, 2017, **43**, 3774 – 3783.
- [71] F. Cai, S. Zhang, J. Li, Z. Chen, M. Li and L. Wang, *Applied Surface Science*, 2011, **258**, 1819 – 1825.
- [72] E. L. Bourhis, P. Goudeau, M. Staia, E. Carrasquero and E. Puchi-Cabrera, *Surface and Coatings Technology*, 2009, **203**, 2961 – 2968.
- [73] F. Jose, R. Ramaseshan, S. Dash, A. Dasgupta, S. Saroja and A. K. Tyagi, *Journal of Nanoscience and Nanotechnology*, 2009, **9**, 5451–5454.
- [74] M. Maqbool, K. Main and M. Kordesch, *Opt. Lett.*, 2010, **35**, 3637–3639.
- [75] M. Maqbool, K. Main and I. Ahmad, *Journal of Low Temperature Physics*, 2015, **179**, 365–374.
- [76] N. Tatemizo, Y. Miura, K. Nishio, S. Hirata, F. Sawa, K. Fukui, T. Isshiki and S. Imada, *J. Mater. Chem. A*, 2017, **5**, 20824–20832.
- [77] Y. Gai, J. Li, S.-S. Li, J.-B. Xia and S.-H. Wei, *Physical review letters*, 2009, **102**, 036402.

- [78] E. Iborra, J. Capilla, J. Olivares, M. Clement and V. Felmetzger, IEEE International Ultrasonics Symposium, 2012, pp. 2734–2737.
- [79] X. Y. Cui, D. Fernandez-Hevia, B. Delley, A. J. Freeman and C. Stampfl, *Journal of Applied Physics*, 2007, **101**, 103917.
- [80] B. Amin, S. Arif, I. Ahmad, M. Maqbool, R. Ahmad, S. Goumri-Said and K. Prisybrey, *Journal of Electronic Materials*, 2011, **40**, 1428–1436.
- [81] J. T. Luo, B. Fan, F. Zeng and F. Pan, *Journal of Physics D: Applied Physics*, 2009, **42**, 235406.
- [82] F. Jose, R. Ramaseshan, S. Dash, S. Bera, A. K. Tyagi and B. Raj, *Journal of Physics D: Applied Physics*, 2010, **43**, 075304.
- [83] Q. Wang, F. Zhou and J. Yan, *Surface and Coatings Technology*, 2016, **285**, 203–213.
- [84] J. Rujisomnapa, S. Surinphong and P. Wongpanya, Current Trends in the Development of Industry, 2013, pp. 858–863.
- [85] C. Nouveau, C. Labidi, J.-P. F. Martin, R. Collet and A. Djouadi, *Wear*, 2007, **263**, 1291 – 1299.
- [86] H. C. Barshilia, N. Selvakumar, B. Deepthi and K. Rajam, *Surface and Coatings Technology*, 2006, **201**, 2193–2201.
- [87] A. Reiter, V. Derflinger, B. Hanselmann, T. Bachmann and B. Sartory, *Surface and Coatings Technology*, 2005, **200**, 2114 – 2122.
- [88] H. Yamashita, K. Fukui, S. Misawa and S. Yoshida, *Journal of Applied Physics*, 1979, **50**, 896–898.

- [89] L. Benedict, T. Wethkamp, K. Wilmers, C. Cobet, N. Esser, E. L. Shirley, W. Richter and M. Cardona, *Solid state communications*, 1999, **112**, 129–133.
- [90] L.-P. Wang, D. S. Shim, Q. Ma, V. R. Rao, E. Ginsburg and A. Talalyevsky, *Journal of Vacuum Science & Technology A*, 2005, **23**, 1284–1289.
- [91] W. Jiang, W. Lin, S. Li, J. Chen and J. Kang, *Optical Materials*, 2010, **32**, 891 – 895.
- [92] S. Shokhovets, R. Goldhahn, G. Gobsch, S. Piekh, R. Lantier, A. Rizzi, V. Lebedev and W. Richter, *Journal of Applied Physics*, 2003, **94**, 307–312.
- [93] B. D. Cullity, *Elements of X-Ray Diffraction*, Addison-Wesley, USA, Second Edition edn., 1978.
- [94] M. Birkholz, *Thin Film Analysis by X-Ray Scattering*, Wiley-VCH, Weinheim, 2006.
- [95] A. K. Zak, W. A. Majid, M. Abrishami and R. Yousefi, *Solid State Sciences*, 2011, **13**, 251 – 256.
- [96] B. B. He, *Two-Dimensional X-Ray Diffraction*, John Wiley & Sons, New Jersey, 2009.
- [97] R. Egerton, *Physical Principles of Electron Microscopy: An Introduction to TEM, SEM, and AEM*, Springer, US, 2011.
- [98] J. Watts and J. Wolstenholme, *An Introduction to Surface Analysis by XPS and AES*, John Wiley & Sons, 2003.
- [99] M. Newville, *Reviews in Mineralogy and Geochemistry*, 2014, **78**, 33–74.
- [100] C. H. Booth and F. Bridges, *Physica Scripta*, 2005, **2005**, 202.

- [101] C. Adelhelm, M. Balden and M. Sikora, *Materials Science and Engineering: C*, 2007, **27**, 1423–1427.
- [102] K. Hamamoto, T. Suzuki, B. Liang, T. Yamaguchi, H. Sumi, Y. Fujishiro, B. Ingram, A. J. Kropf and J. D. Carter, *Journal of Power Sources*, 2013, **222**, 15–20.
- [103] D. Konigsberger and R. Prince, *X-Ray Absorption: Principles, Applications, Techniques of EXAFS, SEXAFS and XANES*, Wiley, New York, 1988.
- [104] M. Newville, B. Ravel, D. Haskel, J. Rehr, E. Stern and Y. Yacoby, *Physica B: Condensed Matter*, 1995, **208-209**, 154 – 156.
- [105] W. Oliver and G. Pharr, *Journal of Materials Research*, 2004, **19**, 3–20.
- [106] S. Tripura Sundari, R. Ramaseshan, F. Jose, S. Dash and A. K. Tyagi, *Journal of Applied Physics*, 2014, **115**, 033516.
- [107] M. Modreanu, J. Sancho-Parramon, O. Durand, B. Servet, M. Stchakovsky, C. Eypert, C. Naudin, A. Knowles, F. Bridou and M.-F. Ravet, *Applied Surface Science*, 2006, **253**, 328 – 334.
- [108] K.-H. Chiu, J.-H. Chen, H.-R. Chen and R.-S. Huang, *Thin Solid Films*, 2007, **515**, 4819 – 4825.
- [109] R. Guinebretière, *X-ray Diffraction by Polycrystalline Materials*, ISTE Ltd, 2007.
- [110] M.-S. Lee, S. Wu, S.-B. Jhong, K.-T. Liu, R. Ro, C.-C. Shih, Z.-X. Lin, K.-I. Chen and S.-C. Cheng, *Microelectronics Reliability*, 2010, **50**, 1984–1987.
- [111] S. Mahieu, P. Ghekiere, D. Depla and R. D. Gryse, *Thin Solid Films*, 2006, **515**, 1229 – 1249.

- [112] P. Panda, R. Ramaseshan, N. Ravi, G. Mangamma, F. Jose, S. Dash, K. Suzuki and H. Suematsu, *Materials Chemistry and Physics*, 2017, **200**, 78 – 84.
- [113] J. Wang, Q. Zhang, G. F. Yang, C. J. Yao, Y. J. Li, R. Sun, J. L. Zhao and S. M. Gao, *Journal of Materials Science: Materials in Electronics*, 2016, **27**, 3026–3032.
- [114] C. L. Tien, T. W. Lin, K. C. Yu, T. Y. Tsai and H. F. Shih, *IEEE Transactions on Magnetism*, 2014, **50**, 1–4.
- [115] W. M. Yim and R. J. Paff, *Journal of Applied Physics*, 1974, **45**, 1456–1457.
- [116] B. W. Sheldon, K. H. A. Lau and A. Rajamani, *Journal of Applied Physics*, 2001, **90**, 5097–5103.
- [117] J. A. Thornton and D. Hoffman, *Thin Solid Films*, 1989, **171**, 5 – 31.
- [118] H. Windischmann, *Critical Reviews in Solid State and Materials Sciences*, 1992, **17**, 547–596.
- [119] J. Song and J. Yu, *Thin Solid Films*, 2002, **415**, 167 – 172.
- [120] G. Guisbiers and L. Buchaillet, *Journal of Physics D: Applied Physics*, 2008, **41**, 172001.
- [121] R. Jayaganthan, K. Mohankumar and A. Tay, *International Journal of Nanoscience*, 2005, **4**, 197–205.
- [122] P. Loper, M. Stuckelberger, B. Niesen, J. Werner, M. Filipic, S.-J. Moon, J.-H. Yum, M. Topic, S. De Wolf and C. Ballif, *J. Phys. Chem. Lett.*, 2015, **6**, 66–71.
- [123] G. E. Jellison Jr, M. A. McGuire, L. A. Boatner, J. D. Budai, E. D. Specht and D. J. Singh, *Physical Review B*, 2011, **84**, 195439.



- [124] G. Jellison Jr, L. Boatner, J. Budai, B.-S. Jeong and D. Norton, *Journal of Applied Physics*, 2003, **93**, 9537–9541.
- [125] M.-I. Kang, S. W. Kim, Y.-G. Kim and J.-W. Ryu, *Journal of the Korean Physical Society*, 2010, **57**, 389–394.
- [126] M. Gaillet, L. Yan and E. Teboul, *Thin solid films*, 2007, **516**, 170–174.
- [127] T. Easwarakhanthan, M. B. Assouar, P. Pigeat and P. Alnot, *Journal of Applied Physics*, 2005, **98**, 073531.
- [128] P. Janicek, K. M. Niang, J. Mistrik, K. Palka and A. J. Flewitt, *Applied Surface Science*, 2017, **421**, 557–564.
- [129] S. T. Sundari, N. Raut, T. Mathews, P. Ajikumar, S. Dash, A. Tyagi and B. Raj, *Applied Surface Science*, 2011, **257**, 7399 – 7404.
- [130] Z. Zhao, B. Tay, L. Huang, S. Lau and J. Gao, *Optical Materials*, 2004, **27**, 465 – 469.
- [131] J. A. Thornton, *Journal of Vacuum Science and Technology*, 1974, **11**, 666–670.
- [132] G. Balakrishnan, S. T. Sundari, R. Ramaseshan, R. Thirumurugesan, E. Mohandas, D. Sastikumar, P. Kuppusami, T. Kim and J. Song, *Ceramics International*, 2013, **39**, 9017 – 9023.
- [133] L. Jiang, W. Shen, H. Ogawa and Q. Guo, *Journal of applied physics*, 2003, **94**, 5704–5709.
- [134] P. Panda, R. Ramaseshan, S. T. Sundari and H. Suematsu, *OSA Continuum*, 2018, **1**, 1241–1250.
- [135] J. Kar, G. Bose and S. Tuli, *Surface and Coatings Technology*, 2005, **198**, 64 – 67.

- [136] S. Fan, K. Yao, Z. Huang, J. Zhang, G. Gao and G. Du, *Chemical Physics Letters*, 2009, **482**, 62 – 65.
- [137] D. Chen, D. Xu, J. Wang and Y. Zhang, *Journal of Physics D: Applied Physics*, 2008, **41**, 235303.
- [138] G. Greczynski, D. Primetzhofer, J. Lu and L. Hultman, *Applied Surface Science*, 2017, **396**, 347 – 358.
- [139] P. Motamedi and K. Cadien, *Applied Surface Science*, 2014, **315**, 104 – 109.
- [140] G. Greczynski and L. Hultman, *Applied Surface Science*, 2016, **387**, 294 – 300.
- [141] D. Jaeger and J. Patscheider, *Journal of Electron Spectroscopy and Related Phenomena*, 2012, **185**, 523 – 534.
- [142] X. H. Ji, S. P. Lau, G. Q. Yu, W. H. Zhong and B. K. Tay, *Journal of Physics D: Applied Physics*, 2004, **37**, 1472.
- [143] A. Mahmood, R. Machorro, S. Muhl, J. Heiras, F. Castillon, M. Farias and E. Andrade, *Diamond and Related Materials*, 2003, **12**, 1315 – 1321.
- [144] M.-H. Tuilier, M.-J. Pac, G. Covarel, C. Rousselot and L. Khouchaf, *Surface and Coatings Technology*, 2007, **201**, 4536 – 4541.
- [145] P. Panda, N. G. Krishna, P. Rajput and R. Ramaseshan, *Phys. Chem. Chem. Phys.*, 2018, **20**, 29817–29825.
- [146] T. Yamamoto, *X-Ray Spectrometry: An International Journal*, 2008, **37**, 572–584.
- [147] M. Hashimoto, S. Emura, H. Tanaka, T. Honma, N. Umesaki, S. Hasegawa and H. Asahi, *Journal of Applied Physics*, 2006, **100**, 103907.

- [148] P. Durant and B. Durrant, *Introduction to Advanced Inorganic Chemistry*, Longman Group, London, 1970.
- [149] *ISO 14577-1 : Metallic materials - Instrumented indentation test for hardness and materials parameters - Part 1: Test method*, 2015.
- [150] H. Ichimura and I. Ando, *Surface and Coatings Technology*, 2001, **145**, 88 – 93.
- [151] A. Fischer-Cripps, *Nanoindentation*, Springer-Verlag, New York, 2002.
- [152] A. Conde, A. Cristobal, G. Fuentes, T. Tate and J. de Damborenea, *Surface and Coatings Technology*, 2006, **201**, 3588 – 3595.
- [153] P. Panda, R. Ramaseshan, M. Sahoo, N. G. Krishna, A. K. Yadav, S. N. Jha and D. Bhattacharyya, *Phys. Chem. Chem. Phys.*, 2018, **20**, 13084–13091.
- [154] A. Pantelouris, H. Modrow, M. Pantelouris, J. Hormes and D. Reinen, *Chemical Physics*, 2004, **300**, 13 – 22.
- [155] Q. Wang, A. K. Kandalam, Q. Sun and P. Jena, *Phys. Rev. B*, 2006, **73**, 115411.
- [156] Y. Saeed, A. Shaukat, S. Nazir, N. Ikram and A. H. Reshak, *Journal of Solid State Chemistry*, 2010, **183**, 242 – 249.
- [157] E. Shuichi, K. Shigeya, T. Katsuhiko, T. Hiroyuki, H. Shigehiko and A. Hajime, *physica status solidi c*, 2011, **8**, 473–475.
- [158] P. Panda and R. Ramaseshan, *Ceramics International*, 2019, **45**, 1755–1760.